Copyright

by

Despina Milathianaki

2010

The Dissertation Committee for Despina Milathianaki certifies that this is the approved version of the following dissertation:

Time-Resolved Lattice Measurements of Shock-Induced Phase Transitions in Polycrystalline Materials

Committee:

Todd Ditmire, Supervisor

Roger Bengtson

Michael Downer

Michael Marder

Eric Taleff

Time-Resolved Lattice Measurements of Shock-Induced Phase Transitions in Polycrystalline Materials

by

Despina Milathianaki, M.Sci.; M.S.

Dissertation

Presented to the Faculty of the Graduate School of

The University of Texas at Austin

in Partial Fulfillment

of the Requirements

for the Degree of

Doctor of Philosophy

The University of Texas at Austin

May, 2010

ACKNOWLEDGEMENTS

I am truly grateful to my family, my colleagues, and dissertation advisors at the University of Texas at Austin and Lawrence Livermore National Laboratory for their support throughout this effort. My parents Filippos and Rena and sister Maria deserve my biggest thank you since they have been behind me in all my career pursuits, however reasonable or unreasonable these may have been and despite the thousands of miles they have put in between us. My husband Greg gave me tons of encouragement, support, and motivation towards the finishing line so I would like to thank him enormously for this. He also contributed to my greatest achievement in life that could not have been described in this document: our daughter Melina. In a way, Melina was part of this research effort too as unknowingly she participated in my final and most fruitful data runs and also motivated me to complete my dissertation writing in a timely manner.

Having spent the majority of my PhD at LLNL, I came to realize the value of teamwork and the importance of supportive, dependable, and patient teammates. I am especially thankful to my colleagues Bassem El-Dasher, Jim Hawreliak, Jim McNaney and Damian Swift for their consistent support throughout my student term at LLNL that came in the form of useful discussions, assistance in the experiments, editing papers, and in general, providing me with guidance in all my research efforts. I am also extremely thankful towards Hector Lorenzana, who gave me the opportunity to receive training and perform research at the forefront of his efforts in dynamic x-ray diffraction.

Last but not least, I would like to thank my UT advisor, Todd Ditmire, for being the driver for my scientific pursuits from the time I first met him as an undergraduate student at the Laser Consortium of Imperial College in London. From Todd I have learnt that great scientific challenges are like puzzles: if you focus on one piece only, you will never be able to solve them. Hopefully, one day I will be able to view clearly the "big picture" of my research like he does.

Time-Resolved Lattice Measurements of Shock-Induced Phase Transitions in Polycrystalline Materials

Publication No.____________

Despina Milathianaki, Ph.D.
The University of Texas at Austin, 2010

Supervisor: Todd Ditmire

The response of materials under extreme temperature and pressure conditions is a topic of great significance because of its relevance in astrophysics, geophysics, and inertial confinement fusion. In recent years, environments exceeding several hundred gigapascals in pressure have been produced in the laboratory via laser-based dynamic loading techniques. Shock-loading is of particular interest as the shock provides a fiducial for measuring time-dependent processes in the lattice such as phase transitions. Time-resolved x-ray diffraction is the only technique that offers an insight into these shock-induced processes at the relevant spatial (atomic) and temporal scales.

In this study, nanosecond resolution x-ray diffraction techniques were developed and implemented towards the study of shock-induced phase transitions in polycrystalline materials. More specifically, the capability of a focusing x-ray diffraction geometry in high-resolution *in situ* lattice measurements was demonstrated by probing shock-compressed Cu and amorphous metallic glass samples. In addition, simultaneous lattice and free surface velocity measurements of shock-compressed Mg in the ambient hexagonal close packed (hcp) and shock-induced body centered cubic (bcc) phases between 12 and 45 GPa were performed. These measurements revealed x-ray diffraction signals consistent with a compressed bcc lattice above a shock pressure of 26.2±1.3 GPa, thus capturing for the first time direct lattice evidence of a shock-induced hcp to bcc phase transition in Mg. Our measurement of the hcp-bcc phase boundary in Mg was found to be consistent with the calculated boundary from generalized pseudopotential theory in the pressure and temperature region intersected by the principal shock Hugoniot. Furthermore, the subnanosecond timescale of the phase transition implied by the shock-loading conditions was in agreement with the kinetics of a martensitic transformation. In conclusion, we report on the progress and future work towards time-resolved x-ray diffraction measurements probing solid-liquid phase transitions in high Z polycrystalline materials, specifically Bi.

Table of Contents

1 INTRODUCTION 1

2 SHOCK PHYSICS CONCEPTS 7

2.1 Shock Wave Formation 8

2.2 Conservation Equations 10

2.3 Equation of State 14

2.4 Shock Hugoniot and Entropy 18

2.5 Shock Impedance 20

3 MATERIALS RESPONSE UNDER SHOCK COMPRESSION 24

3.1 Stress-Strain Conventions in Non-Hydrostatic Solids 24

3.2 Elastic and Plastic Shock Regimes 28

3.3 Strong Shock Regime 31

3.4 Shock-Induced Phase Transitions 34

- 3.4.1 Thermodynamics of Phase Transitions 34
- 3.4.2 Kinetics of Phase Transitions 39

3.5 Shock Generation via Laser Ablation 43

- 3.5.1 Momentum Transfer by Laser Ablation 44

3.5.2 Laser Absorption in a Plasma 47

3.5.3 Heat Conduction 49

3.5.4 Equilibirum Radiation Transport 52

4 X-RAY DIFFRACTION FUNDAMENTALS 55

4.1 Geometric Description of Crystals 56

4.1.1 Cubic Lattices 56

4.1.2 Hexagonal Close Packed Lattice 61

4.2 X-Ray Diffraction from Crystals 64

4.2.1 Bragg's Law 65

4.2.2 X-ray Scattering Intensity 71

4.2.3 X-ray absorption 75

4.3 Measuring the Dynamic Material Response with X-ray Diffraction 78

4.3.1 Uniaxial Lattice Compresssion 79

4.3.2 Hydrostatic Lattice Compresssion 83

4.3.3 Phase Transitions 85

4.4 X-ray Emission from a Thermal Plasma 89

5 DESCRIPTION OF EXPERIMENTAL TECHNIQUE AND DIAGNOSTICS 93

5.1 General Description of Experimental Setup 93

5.2 The Janus Laser System...96

5.3 X-Ray Diffraction Diagnostics 99

5.3.1 The Seeman-Bohlin Focusing Diffraction Geometry.......................100

5.3.2 The Cylindrical Powder Pinhole Camera..111

5.4 Two-Channel Line-Imaging Velocimetry 115

5.4.1 Background on Doppler Velocimetry...116

5.4.2 JANUS VISAR Description and Operation....................................120

5.4.3 VISAR free surface velocity extraction..123

5.5 Beam Alignment Diagnostics 125

6 EXPERIMENTAL RESULTS 128

6.1 Density Measurement of Shock-Compressed Copper...............................129

6.2 *In situ* Lattice Measurement of the Bcc Phase Boundary in Magnesium Along the Principal Hugoniot..138

6.2.1 Experiment Description 139

6.2.2 Results from X-Ray Diffraction and Velocimetry...........................143

6.2.3 Identification of the Bcc Phase in Mg 153

6.2.4 Comparison Between Ab initio Bcc Boundary Calculations and Experiments in Mg 155

6.3 Shock-Induced Melt Studies Using Dynamic X-ray Diffraction 162

6.3.1 Demonstration of Single Shot Nanosecond X-ray Diffraction from an Amorphous Material 162

6.3.2 Determination of the Solid-Liquid Boundary in Shocked Bismuth ..164

7 SIMULATIONS OF ABLATION-DRIVEN SHOCKS 169

7.1 An Introduction to HYADES Simulations 170

7.2 Simulations of Shock-Loading in Mg 173

7.3 Shock Profile versus Laser Temporal Waveform 179

8 CONCLUSIONS 183

8.1 Summary of Results 183

8.2 Progress Towards Lattice Measurements in Shocked High Z Materials....186

8.3 Future Work 189

9 REFERENCES 191

VITA 204

1 INTRODUCTION

In recent years, the extreme pressure and temperature conditions produced via dynamic loading have received great attention because of their relevance to astrophysical [1-5], geophysical [6, 7], and inertial confinement fusion (ICF) [8-10] environments. With dynamic loading techniques, such as shock-induced compression [11-13] generated via laser ablation or projectile impact, fundamental questions pertaining to the above environments can be answered within laboratory-scale experiments. For example, an understanding of the formation of planetary systems can be obtained via laboratory equation-of-state measurements of hydrogen. Such measurements can shed light onto the composition of the gas giant planets of our solar system, Jupiter and Saturn, to predict the formation of other planetary systems with similar gas giants. In the area of geophysics, the temperature distribution of the Earth's core that relates to a number of geodynamic phenomena, such as seismic discontinuities, can be deduced from an investigation of the phase diagram of Fe and Fe-rich compounds at pressures equivalent to the Earth's inner core. Such measurements can in principle be obtained using shock-loading to generate the equivalent pressure conditions, and a diagnostic such as streaked pyrometry for temperature measurements. Last, in ICF an understanding of the response of the capsule and hohlraum materials is of paramount importance in order to minimize the possibility of microstructural effects that can seed plasma instabilities capable of quenching the implosion. For this reason, dynamic loading of materials relevant to ICF (diamond, Be, Ta etc.) to capture plasticity and phase transition information is critical for predicting ICF yields. Thus, the extreme pressure and temperature conditions accessed by dynamic loading are applicable to a broad spectrum of scientific and technological areas.

An important problem in all of these areas, as indicated earlier, is gaining an insight into the lattice response especially in the vicinity of solid-solid and solid-liquid phase boundaries. For most materials information on their phase boundaries comes from *ab initio* electronic structure calculations [14-17] where, in order to reduce computational effort, various approximate potentials are used. Especially for structural changes with small equilibrium energy differences and/or phase boundaries at extremely high pressure and temperature conditions, these calculated phase boundaries can vary significantly. Shock-induced phase transformations are of particular interest, as time-resolved information on the phase transition along the shock Hugoniot can be revealed. In this way, non-equilibrium theoretical models used in large-scale molecular dynamics simulations [18-20] can be evaluated, and experimental equation-of-state data within different phases can be obtained.

Historically, two approaches have been employed to provide evidence of shock-induced phase transformations: sample recovery and *in situ* bulk property measurements. In the first approach, microstructural analysis of the recovered shocked samples has been applied in order to infer the dynamic lattice behavior [21-23]. In the second approach, real-time measurements of the bulk response have been performed with optical diagnostics such as velocimetry [24-26], reflectivity monitors [27-31] (linear and nonlinear), and time-resolved pyrometry [32, 33]. Even though these methods can in principle detect a phase change by features in the detected signal, they do not offer lattice-level information that could reveal the atomic re-arrangement process leading to the structural change. In the case of velocimetry measurements, where changes in the compressibility of materials are inferred from the slope of the velocity profile, phase changes with a small volume change (<1 %) may be undetectable. For reflectivity probes, it may be difficult to disassociate changes in reflectivity resulting from the phase change vs. scattering losses attributed to deformation of the probed surface upon shock breakout. Last, streaked optical pyrometry has currently a lower limit of ~0.5 eV [34] (~5.8×10^3 K) in the temperatures detected.

Gaining a fundamental understanding of lattice-level phenomena under dynamic conditions requires *in situ* lattice measurements with sufficient temporal and spatial resolution. Dynamic x-ray diffraction (DXRD) techniques of both single [35, 36] and polycrystalline materials [37, 38] have successfully shown such capabilities and therefore, have been increasingly employed as lattice diagnostics in shock studies over the past few years. Remarkable breakthroughs in single-crystal nanosecond DXRD studies have been the time-resolved measurement of uniaxial compression in Si [39] and the confirmation of the well-known α-ε (bcc-hcp) transition in shock-compressed Fe [40, 41] along the [001] direction. In general, single-crystal DXRD has proven to be important in experiments attempting to associate lattice-level phenomena to the target crystallographic orientation.

X-ray diffraction from shock-loaded polycrystalline materials offers significantly more complex information compared to single crystals due to the unpredictable material behavior along grain boundaries and other material anisotropies. In general, polycrystalline DXRD is highly desirable from the point of view of interrogating materials used in engineering applications. Even though polycrystalline DXRD techniques are potentially very important in extracting information related to material texture, strength-strain rate dependence, and shock-induced phase transformations, probing shock-compressed polycrystalline materials with DXRD, especially these of high Z and/or complex phase diagrams, is a formidable experimental challenge. Because of texture, polycrystalline materials are inherently inefficient x-ray scatterers. Under dynamic conditions, the x-ray scattering efficiency decreases even further because of the highly disordered microstructure.

In this dissertation the research that was proposed had two main thrusts: a) develop x-ray diffraction instrumentation capable of capturing single-shot nanosecond lattice information from shock-induced phase transitions in polycrystalline materials with improved signal-to-noise ratio and angular resolution compared to existing DXRD techniques. The x-ray diffraction technique developed had to be applicable to laser-based x-ray sources and shock waves. b) Demonstrate measurement of a shock-induced phase transition aiming specifically in resolving the controversies of the hcp to bcc phase boundary in Mg.

This dissertation begins by introducing the fundamental concepts in shock physics, dynamic material response, and x-ray diffraction necessary to understand the experiments and results described. More specifically, in Chapter 2, a hydrodynamic treatment of shocks is presented, including the criteria of stable shock formation and shock propagation in a material. The concept of shock impedance and its effect on shock propagation across an interface of materials having mismatched impedances are also discussed as it will prove useful in understanding the shock properties in our ablator coated targets.

In Chapter 3, the material response to uniaxial compression is presented. The material response, from the viewpoint of a pressure-volume Hugoniot measurement, is divided into elastic, plastic, and strong shock regimes. Since the topic of this dissertation encompasses phase transitions, a thermodynamic description of these phenomena is also included. The ablation process responsible for shock formation is briefly described.

Chapter 4 provides a basic background on x-ray diffraction as well as specific information on the crystal structures investigated. Most importantly, dynamic x-ray diffraction in the context of interpreting dynamic lattice-level phenomena is presented. The laser plasma x-ray sources are also described.

In Chapter 5, the experimental techniques developed by the author and implemented for dynamic x-ray diffraction experiments are presented. Special emphasis is given on the focusing x-ray diffraction instrument designed specifically for probing shock-induced phase transitions and for measuring density in absolute equation of state studies.

The results obtained from the application of the techniques presented in Chapter 5 are described in Chapter 6. These include measurement of the density from shocked polycrystalline Cu and of the scattering function from an amorphous material. The latter was performed in order to demonstrate the capability of the instrument in future measurements from a liquid substance. Most important, the first *in situ* lattice measurement of the hcp-bcc phase transition in shocked polycrystalline Mg is presented. Because of the accuracy in our density and pressure determination, our measurements enabled us to assess *ab initio* phase boundary calculations based on the density functional theory. These results on the hcp-bcc boundary in Mg explored along the principal Hugoniot as well as preliminary experiments towards a shock-induced solid-melt investigation in Bi are presented. All of the above results represent original work led by the author.

To gain knowledge of the shock properties in the ablator-coated and uncoated Mg foils, 1D Hydrodynamic simulations using the HYADES code were also performed by the author. Simulation results, including a pressure vs. laser intensity scaling in coated/uncoated Mg and the dependency of the shock profile on the laser temporal profile, are presented in Chapter 7.

Last, an overview of the overall work in this dissertation, progress towards shock-initiated phase transition studies in high Z materials, and future work directions in dynamic phase transition studies are discussed in Chapter 8.

2 SHOCK PHYSICS CONCEPTS

Shock waves are formed as a result of impulsive loading at a rate that is much faster than the intrinsic response time of the material. A classic example of shock formation is that of a snow plow creating a discontinuity between loose and packed snow that travels at a speed that is faster than the speed of the plow itself. The speed of the density discontinuity in the snow is referred to in shock physics terms as the "shock speed" whereas the speed of the plow that equals the rate of displacement of snow is the "particle speed". The plowing action represents "shock-loading"; when the loading rate is faster that the time it takes for the snow ahead to be displaced a shock front is formed.

In this chapter, fundamental concepts in shock physics are presented in order to provide the necessary background for discussing the material response under shock-loading [42-44]. Specifically, the conditions for shock formation and assumptions allowing a simple hydrodynamic treatment of the shock properties are discussed. The conservation equations of mass, momentum, and energy are derived as they will be used to describe the thermodynamic and mechanical properties of matter in its initial and shocked states. The thermodynamical information obtained from the combination of the conservation equations and an equation of state (EOS) is also discussed. Last, the effect of impedance on the shock amplitude as it traverses a boundary is explained. The latter concept will become useful in understanding shock propagation in the multi-layer targets used in the experiments, as well as in the relation of particle velocity to free surface velocity measured by Doppler velocimetry.

2.1 Shock Wave Formation

In a laboratory frame of reference, the speed at a location on a compression wave can be represented by $c+u$, i.e. the sum of the speed of sound c in the material and the particle velocity u. For a stable shock wave to be formed c_1+u_1 in the low pressure region of the compression wave must be smaller than c_2+u_2 in the high pressure region (Figure 2.1). This implies the criterion of shock front formation, namely an increasing adiabatic sound speed with pressure or density:

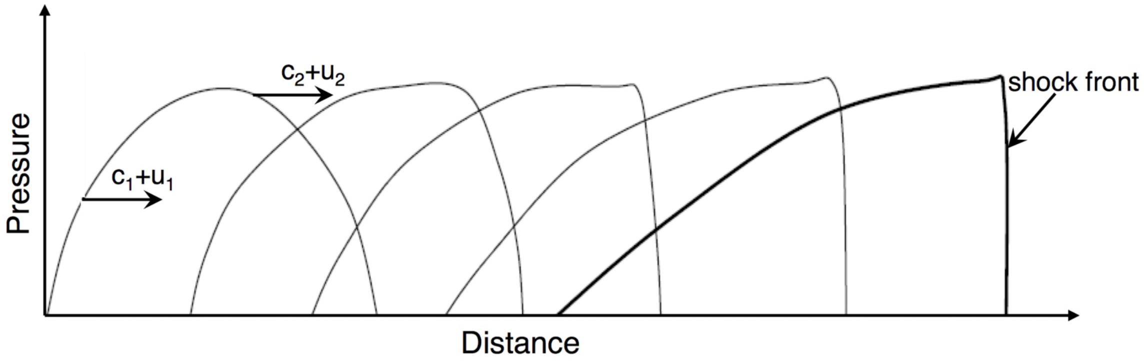

Figure 2.1. Shock front formation from a compressional disturbance. The "steepening" effect occurs because of the increasing speed amplitude with pressure.

$$\frac{\partial c}{\partial P} > 0 \text{ and } \frac{\partial c}{\partial \rho} > 0 . \tag{2.1}$$

The adiabatic sound speed c is linked to the bulk modulus κ and the material density ρ by

$$c = \sqrt{\frac{\kappa}{\rho}}. \tag{2.2}$$

Since the bulk modulus κ can be expressed in terms of the partial derivative of pressure P with respect to volume V, and density ρ, at constant entropy S as

$$\kappa = -V\left(\frac{\partial P}{\partial V}\right)_S = \rho\left(\frac{\partial P}{\partial \rho}\right)_S , \tag{2.3}$$

the criterion for stable shock front formation becomes

$$\frac{\partial c}{\partial \rho} = \frac{\partial}{\partial \rho}\sqrt{\left(\frac{\partial P}{\partial \rho}\right)_S} = \frac{1}{2c}\left(\frac{\partial^2 P}{\partial \rho^2}\right) > 0 \tag{2.4}$$

which is equivalent to

$$\left(\frac{\partial^2 P}{\partial V^2}\right) > 0 \tag{2.5}$$

upon substitution of $\rho=1/V$. Furthermore, for a stable shock front to be sustained in a medium, additional stability criteria are: $c+u$ (in the shocked state) $\geq U$, and c_0 (in the unshocked state) $<U$ where U represents the shock speed. The shock wave must be subsonic with respect to the shocked state and supersonic with respect to the material ahead. Satisfying the above criteria should result in the formation of an infinitesimally thin shock front: however, dissipative mechanisms such as viscosity and heat conduction

counteract the infinite steepening of the shock front and therefore, a steady stress wave is formed when the two opposing effects cancel out.

2.2 Conservation Equations

Conservation equations (mass, momentum, energy) that describe the properties of the shock front and of the material through which it propagates can be derived assuming the following:

a) The material behaves as an ideal fluid, namely there is no strength and therefore, no shear stresses. In other words, the applied stresses are isotropic.

b) No phase transformations or elastic-plastic effects take place.

c) The shock is an infinitesimally thin discontinuity of pressure, density, and internal energy.

d) The application of stress is uniaxial and there is no lateral motion.

Because of assumptions a), d), the concepts of applied stress and material pressure can be used interchangeably. For a solid the above assumptions are only valid in the case where the applied stress greatly surpasses the dynamic flow stress of the material such that any deviations from an isotropic stress state are small.

Within the above "hydrodynamic" framework, we can use the example of an ideal gas in a cylinder compressed by a piston of unit area (Figure 2.2) to derive expressions connecting the uncompressed state variables P_0, ρ_0, E_0 and u_0 to the compressed state variables P, ρ, E and u, where P the pressure, ρ the density, E the internal energy and u the particle velocity of the fluid. The speed of the discontinuity front between the two sets of parameters will be assigned the variable U. In addition, the piston speed and average particle speed in the compressed state are assumed to be equal.

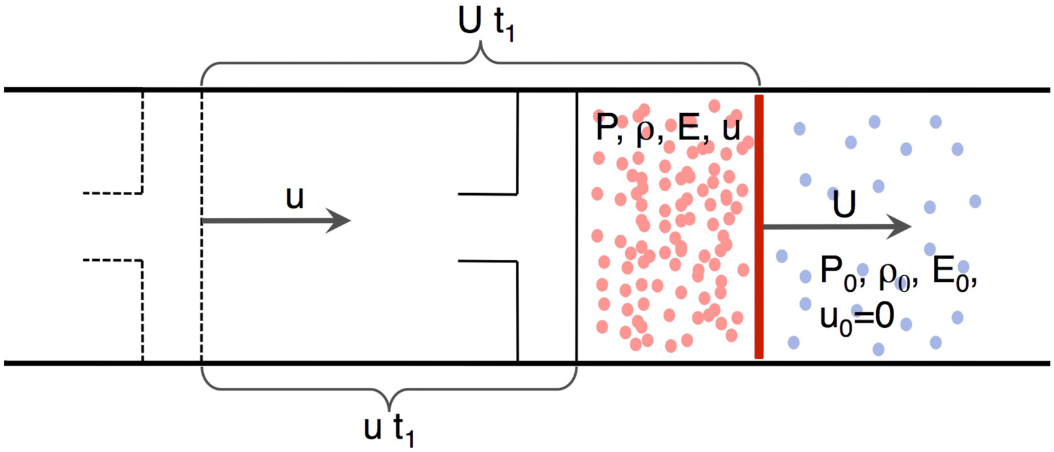

Figure 2.2. Compression of a gas by a moving piston. After time t=t_1 the piston has moved by a distance equal to $u_p t_1$ whereas the compression (shock) front by Ut_1. The front is depicted as a discontinuity in the thermodynamic variables between the initial and final equilibrium states.

The piston and gas is initially (t_0=0) at rest (u_0=0). At t>0, the piston starts to compress the gas while moving at speed u. The front separating the compressed from the uncompressed gas region propagates at speed U. Conservation of mass requires that the compressed mass bounded by the shock front and the piston at t=t_1 is equal to the uncompressed mass encompassed by the shock front in time t_1. Thus

$$\rho_0 U t_1 = \rho(U-u)t_1 \Rightarrow \rho_0 U = \rho(U-u) \Rightarrow \frac{U}{u} = \frac{\rho}{\rho-\rho_0}. \qquad (2.6)$$

The change in momentum Δp between the initially stationary gas and the compressed gas at $t{=}t_1$ is equal to the applied impulse I from the piston. Since by definition

$$I = F\Delta t = \frac{\Delta P}{A}\Delta t = \Delta p \ , \tag{2.7}$$

for a unit cross-sectional area A the pressure in the compressed gas becomes equal to

$$\left(P - P_0\right)\Delta t = \rho\left(U - u\right)\Delta t \cdot u \Rightarrow \left(P - P_0\right) = \rho\left(U - u\right)u \ . \tag{2.8}$$

By substituting ρ with the expression obtained from the mass conservation equation

$$P - P_0 = \rho_0 U u. \tag{2.9}$$

The above equation relates the compressed fluid pressure to the particle and shock speed. The latter two variables can be experimentally determined to provide a shock pressure calibration as it will be shown in Chapter 5. Substituting the shock speed U in the above expression, using equation (2.6), results in

$$P - P_0 = \frac{\rho \cdot \rho_0}{\left(\rho - \rho_0\right)} u^2 \ . \tag{2.10}$$

This is another very useful expression for the shock pressure as density and particle speed can both be measured experimentally.

Last, conservation of energy in the piston/gas system is satisfied when the work done by the piston ΔW_{piston} over a distance ut_1 equals the sum of the change in kinetic energy $\Delta K.E._{fluid}$ and internal energy ΔE (per unit mass)$_{fluid}$ in the gas, $\Delta W_{piston} = \Delta K.E._{fluid} + \Delta E$ (per unit mass)$_{fluid}$, namely

$$P \cdot ut_1 = \tfrac{1}{2}\rho_0 U t_1 \cdot u^2 + \rho_0 U t_1 \cdot \left(E - E_0\right). \tag{2.11}$$

Eliminating the particle and shock speed by using the conservation of mass/momentum relations yields

$$\left(E - E_0\right) = \tfrac{1}{2}\left(P + P_0\right)\left(\frac{\rho - \rho_0}{\rho\rho_0}\right) \tag{2.12}$$

where upon substitution of $V = 1/\rho$ results in the Rankine-Hugoniot equation

$$\left(E - E_0\right) = \tfrac{1}{2}\left(P + P_0\right)\left(V_0 - V\right). \tag{2.13}$$

These conservation equations, derived with the assumption of an infinitesimally thick discontinuity or a “jump” between an initial and final equilibrium state, are also valid for steady shocks and shocks whose rise time is much faster than the material response. Therefore the above equations are applicable to calculations for a wide range of loading conditions. They also constrain the five state variables (P, ρ, E, u, U) to a two dimensional surface. In order to eliminate another independent variable as well as be able to predict the equilibrium thermodynamic state of the material behind the steady shock, a material-specific equation is introduced.

2.3 Equation of State

A well-known equation of state (EOS) is that of an ideal gas

$$E(P,V) = \frac{PV}{\gamma - 1} \tag{2.14}$$

where $\gamma = C_P/C_V$ the ratio of the specific heat at constant volume and pressure respectively. In the context of shocks in an ideal gas, substitution of the above expression into the Rankine-Hugoniot equation results in a P-V relation

$$\frac{P}{P_0} = \frac{(\gamma+1)V_0 - (\gamma-1)V}{(\gamma+1)V - (\gamma-1)V_0} \tag{2.15}$$

which is referred to as the shock Hugoniot in an ideal gas. For a solid, a commonly used EOS is the Mie-Gruneisen

$$E(P,V) = E_k(V) + \frac{V(P - P_k(V))}{\Gamma(V)} \tag{2.16}$$

where $E_k(V)$, $P_k(V)$ the internal energy and pressure on a reference isotherm respectively and $\Gamma(V)$ the Gruneisen parameter

$$\Gamma(V) = V\left(\frac{\partial P}{\partial E}\right)_V. \tag{2.17}$$

The Mie-Gruneisen equation can also be related to any other reference state such as a Hugoniot state. In this way the off-Hugoniot P, E parameters can be determined assuming the same volume between the Hugoniot and off-Hugoniot states.

In the shock physics literature the experimentally measured shock speed U and particle speed u are often combined into a linear equation of the form:

$$U = C_0 + Su. \tag{2.18}$$

This is also referred to as an EOS, where C_0 and S are constants. A table with the EOS constants C_0 and S for materials of interest is shown below, together with U-u, P-u, and u-ρ plots for the same materials (Figure 2.3). These plots are common representations of the shock Hugoniot nominally starting from ambient pressure and temperature conditions (principal Hugoniot).

Table 2.1 Properties relevant to shock calculations for materials of experimental interest.

Material	ρ_0 $(10^3\ kg/m^3)$	C_0 $(10^3\ m/s)$	*S*	γ
Mg	1.74	4.49	1.24	1.6
Cu	8.93	3.94	1.49	2.0
Bi	9.84	1.83	1.47	1.1

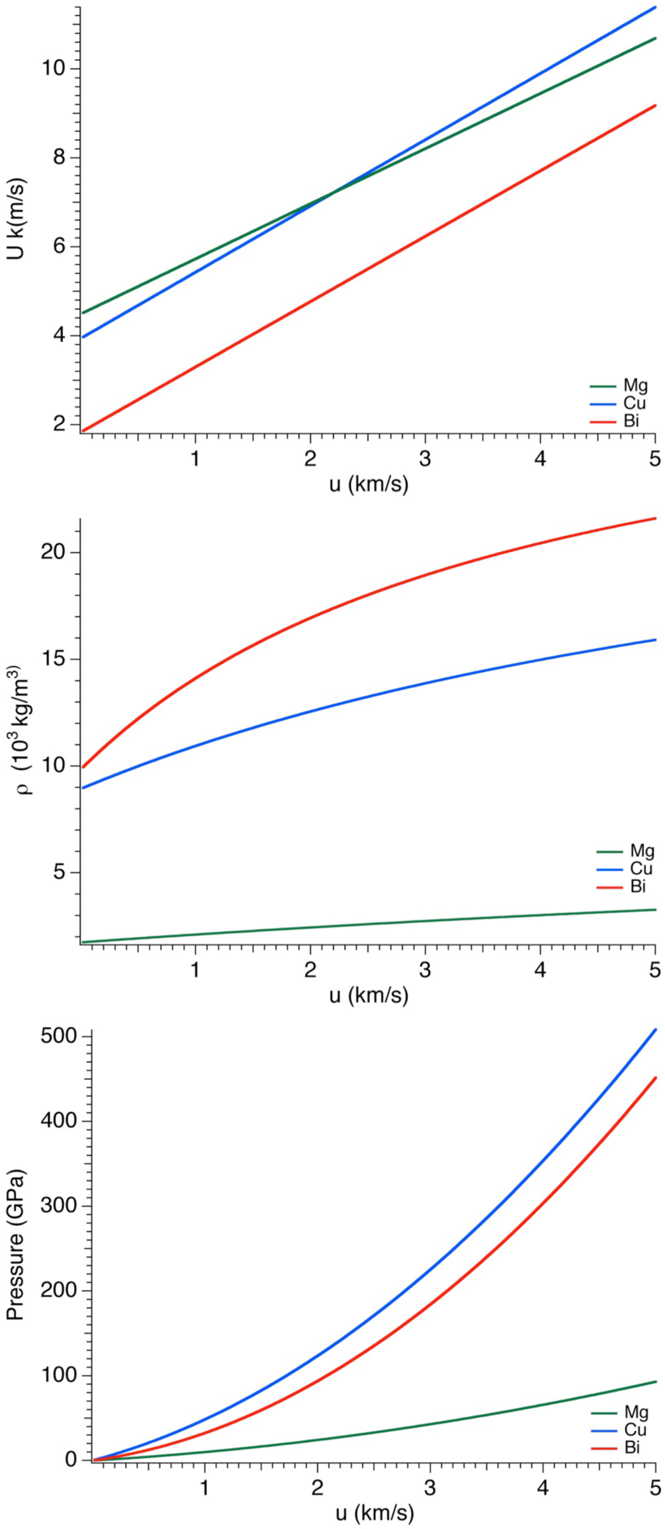

Figure 2.3. ***U*-*u*, *ρ*-*u*, and *P*-*u* plots for Mg, Cu, and Bi using the equation of state parameters from Table 2.1.**

2.4 Shock Hugoniot and Entropy

In the previous section the formulation of a Hugoniot was demonstrated by combining the three conservation equations with an EOS. In this section, a brief description of the Hugoniot properties will be provided together with the thermodynamic information that they convey.

Based upon the derivation of the Hugoniot, it is clear that it does not represent a thermodynamic path. The Hugoniot is a locus of end states that a material attains as a result of shock-loading from an initial *P*-*V* state. However, it can be shown that in the limit of weak shocks the Hugoniot overlaps with the material isentrope (Figure 2.4). For increasing pressure, the Hugoniot is above the isentrope; the difference in the area underneath the isentrope and Hugoniot between the same initial and final *P*-*V* conditions represents the irreversible heating caused by the shock. Figure 2.4 depicts the Hugoniot, isentrope, and Rayleigh line between the initial and final states for a compressed ideal gas. The isentrope for an ideal gas is given by

$$\frac{P}{P_0} = \left(\frac{V}{V_0} \right)^{-\gamma}, \tag{2.19}$$

after differentiating the expression for entropy $S = C_V \ln\left(PV^{\gamma}\right) + const.$ and setting dS=0. The Rayleigh line, namely the line connecting the initial and final Hugoniot states, represents the thermodynamic path of the loading process. Its slope is proportional to the

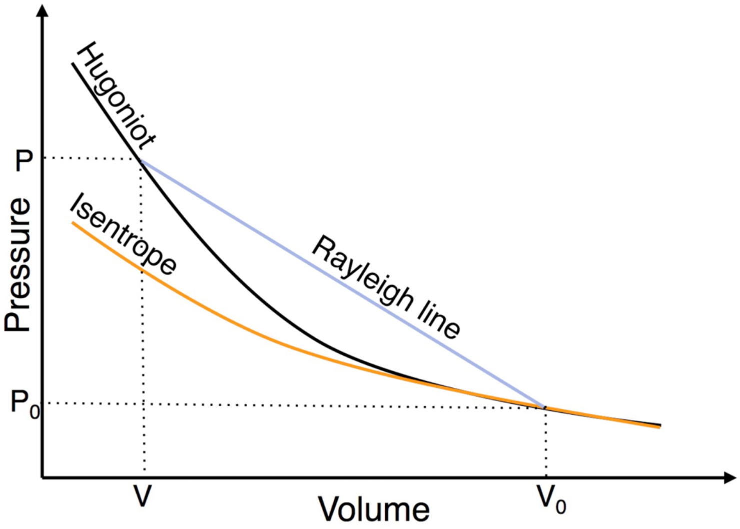

Figure 2.4. ***P-V*** **plot depicting the Hugoniot, isentrope, and Rayleigh line connecting specific initial and final end states accessed via shock-loading.**

shock speed in the material, which can be shown by equation (2.10) after substituting ρ with $1/V$. We find that

$$\frac{P-P_0}{V_0-V}=\left(\frac{U}{V_0}\right)^2 \tag{2.20}$$

where

$$U=V_0\sqrt{\frac{P-P_0}{V_0-V}} \tag{2.21}$$

and

$$u=\sqrt{(P-P_0)(V_0-V)}\,. \tag{2.22}$$

Thus, the slope of the Rayleigh line is proportional to the shock speed in the material. In addition, since the specific kinetic energy equals $u^2/2$ it is obvious from equation (2.22) that it equals the triangular area defined by the Rayleigh, P_0, and V lines. From the Rankine-Hugoniot equation (2.13), the change in the specific internal energy is represented by the area bounded by the Rayleigh, V_0, and V lines. Note that the Hugoniot is a concave upward function, that is the velocity is an increasing function of the shock pressure as required by the stability condition equation (2.5).

2.5 Shock Impedance

The behavior of shock waves at boundaries such as these present in multi-layer targets is an important problem. A number of laser driven shock experiments utilize targets coated by an ablator layer to avoid material preheat, in other words ensuring that shock compression occurs on a target at ambient temperature conditions. Furthermore, critical information is often extracted from the surface velocity of a compressed target during shock break out into vacuum or into another substrate such as LiF. Therefore, the shock propagation properties across different interfaces must be well-understood.

Let us consider two materials A, B with density ρ_A and ρ_B respectively (Figure 2.5). When a stress wave of amplitude σ_i reaches their interface, transmitted and reflected stress waves of amplitude σ_t and σ_r are generated to satisfy pressure continuity across the interface

$$\sigma_i + \sigma_r = \sigma_t \,. \tag{2.23}$$

In addition, continuity of velocity where v_i the incident, v_r the reflected, and v_t the transmitted velocity is satisfied by the relation

$$v_i - v_r = v_t\,. \tag{2.24}$$

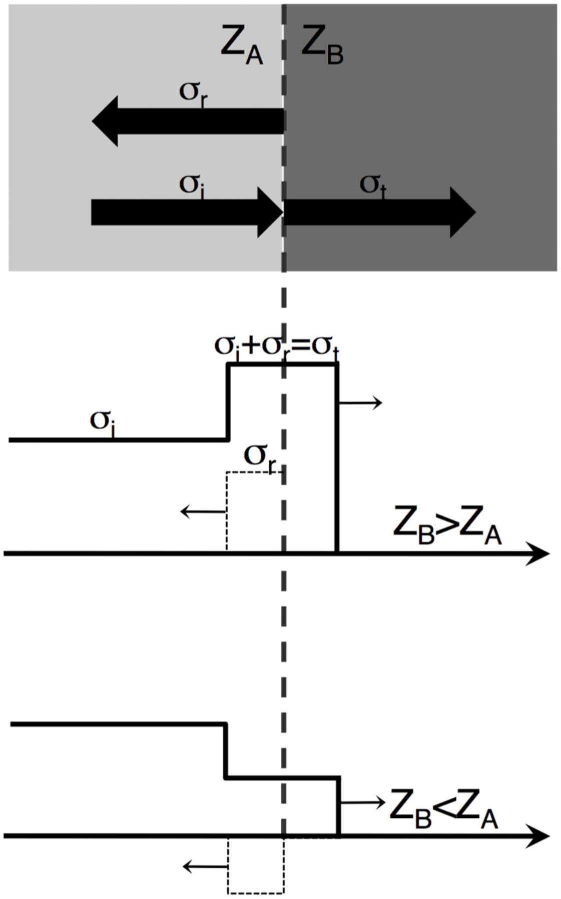

Z_A
Z_B
σ_r
σ_i
σ_t
$\sigma_i+\sigma_r=\sigma_t$
σ_i
σ_r
$Z_B>Z_A$
$Z_B<Z_A$

Figure 2.5. Shock transmission and reflection at a boundary of materials with different impedance. The effect on the incident shock amplitude in the cases $Z_A> Z_B$ and $Z_B<Z_A$ is illustrated.

Defining the product of the static density and shock speed as the material shock impedance $Z \equiv \rho U$ and from equation 2.9, $\sigma_i = Z_A v_i$, $\sigma_r = Z_A v_r$ and $\sigma_t = Z_B v_t$. Substituting the above expressions into (2.23) and combining with (2.24) we obtain the ratios for the reflected and transmitted velocity amplitude to the incident velocity amplitude

$$\frac{v_r}{v_i} = \frac{Z_B - Z_A}{Z_B + Z_A} \tag{2.25}$$

and

$$\frac{v_t}{v_i} = \frac{2Z_A}{Z_B + Z_A} \,. \tag{2.26}$$

Similarly the ratio of the transmitted and reflected stress wave amplitudes to the incident wave amplitude becomes

$$\frac{\sigma_r}{\sigma_i} = \frac{Z_B - Z_A}{Z_B + Z_A} \tag{2.27}$$

and

$$\frac{\sigma_t}{\sigma_i} = \frac{2Z_B}{Z_B + Z_A} \,. \tag{2.28}$$

From the above expressions, it is clear that impedance matching where Z_A=Z_B results in no reflections at an interface. A shock wave in material A should propagate undisturbed into material B. This situation is encountered in several shock experiments utilizing a transparent backing material such as LiF, onto which a target material of equal impedance is coated. The advantage of this configuration is that a "true" measurement of the particle velocity can be made as $v_t = v_i$. In the limit Z_B=0, such as when a shock breaks out into vacuum, $\sigma_r = -\sigma_i$, $v_r = -v_i$, and $v_t = 2v_i$. A reflected rarefaction wave of equal amplitude to the incident shock wave is generated at the material/vacuum interface. In addition, the latter result supports the common assumption made in free surface velocimetry, namely that the free surface velocity equals twice the particle velocity in the target upon shock breakout into vacuum.

In metallic targets coated by plastic ablator layers, discussed in more detail in Chapter 7, impedance mismatch is inevitable. As an example consider a 10 GPa amplitude shock wave at the interface of a parylene-N ablator ρ_{CH}=1.11 x10^3 kg/m^3 and a magnesium target ρ_{Mg}=1.74 x10^3 kg/m^3. At a pressure of 10 GPa, equation of state data for parylene-N suggest a shock speed U_{CH}=4.9 x10^3 m/s and Z_{CH}=5.4 (x10^6). Similarly for Mg at 10 GPa, U_{Mg}=5.8 x10^3 m/s and Z_{Mg}=10.1 (x10^6). The reflected shock wave in parylene-N has amplitude $\sigma_r = 0.3\sigma_i$. The transmitted shock wave has amplitude $\sigma_t = 1.3\sigma_i$. In general, for a given ablation pressure, the addition of a lower *Z* ablator layer on a target material can result in a favorable pressure increase at the interface because of the impedance mismatch between materials. Simulations of this effect will be shown in Chapter 7.

3 MATERIALS RESPONSE UNDER SHOCK COMPRESSION

In this chapter a background on the material response under shock compression is provided [45-48]. The role of shear stresses is now taken into account, which necessitates the formulation of a set of stress-strain conventions that describe the non-hydrostatic component of the material response. As the effect of shear stresses is dependent upon the shock-loading conditions, two regimes in the material behavior are differentiated; a low pressure elastic-plastic regime where the material behavior transits from being "spring-like" to becoming permanently deformed, and a high pressure "strong shock" regime where shear stresses are negligible compared to the hydrostatic component of pressure. Features in the shock wave profile are linked to the macroscopic material response in these regimes. A special section is dedicated to the thermodynamics of shock-induced phase transformations as they are highly relevant to the experimental results described in Chapter 6. Last, the basic physics of shock generation via laser ablation are presented.

3.1 Stress-Strain Conventions in Non-Hydrostatic Solids

So far in our hydrodynamic treatment of shock wave propagation, pressure has been considered as a scalar. More specifically, we have assumed a compressive load applied to an isotropic fluid in one direction (e.g. x axis). For materials of interest shear stresses and anisotropy require new conventions to link the quantities derived earlier in a hydrostatic state to these of a non-hydrostatic solid. Note that pressure in a fluid is related to stress, namely the force applied on a differential element in a solid by

$$P_{ij} = -\sigma_{ij}, \tag{3.1}$$

where by convention positive pressure results in compression. Within a Cartesian coordinate system, x, y, z are the principal coordinates and all off-diagonal elements vanish. Hence

$$P_{xx} = P_x,\ P_{yy} = P_y,\ P_{zz} = P_z. \tag{3.2}$$

In addition, considering a planar shock front propagating in the x direction

$$P_y = P_z. \tag{3.3}$$

Compression of a material in one axis only is referred to as a state of uniaxial strain as the material is allowed to deform only along the direction of the compression front. Upon release of the pressure the material returns to its original state much like a spring obeying Hooke's law. Deformation along the axes perpendicular to the shock front is encountered when defect formation and propagation in the material causes the material to deform plastically as it will be explained later.

Since the pressure component measured in shock experiments corresponds to P_x, a mean pressure in the material can be defined as

$$\overline{P} = \left(\frac{P_x + P_y + P_z}{3} \right) = \left(\frac{P_x + 2P_y}{3} \right). \tag{3.4}$$

From the simple identity

$$P_x = \left(\frac{P_x + 2P_y}{3} \right) + 2\left(\frac{P_x - P_y}{3} \right) \tag{3.5}$$

(3.4) can be re-written as

$$\overline{P} = P_x - \frac{4}{3}\tau \tag{3.6}$$

where τ is called the maximum resolved shear stress, that is the shear stress on planes oriented at 45° with respect to the shock propagation axis. From (3.6) the maximum resolved shear stress equates to

$$\tau = \frac{\left(P_x - P_y\right)}{2}. \tag{3.7}$$

In addition, in plane shock wave experiments the dynamic yield strength [49] is a property that quantifies the difference between the longitudinal and lateral stresses in an isotropic material under uniaxial strain where

$$Y = P_x - P_y \Rightarrow \overline{P} = P_x - \frac{2}{3}Y \,. \tag{3.8}$$

Note that in the case of hydrostatic (rather than uniaxial) compression $\overline{P} = P_x = P_{hydrostatic}$. The difference between the hydrostatic Hugoniot and the Hugoniot inclusive of shear stresses is shown in Figure 3.1. At increasingly higher shock pressure the yield strength becomes small compared to $P_{hydrostatic}$ so the shock pressure can be safely approximated to a hydrostatic Hugoniot end state. More details on the material response at different shock regimes are presented below.

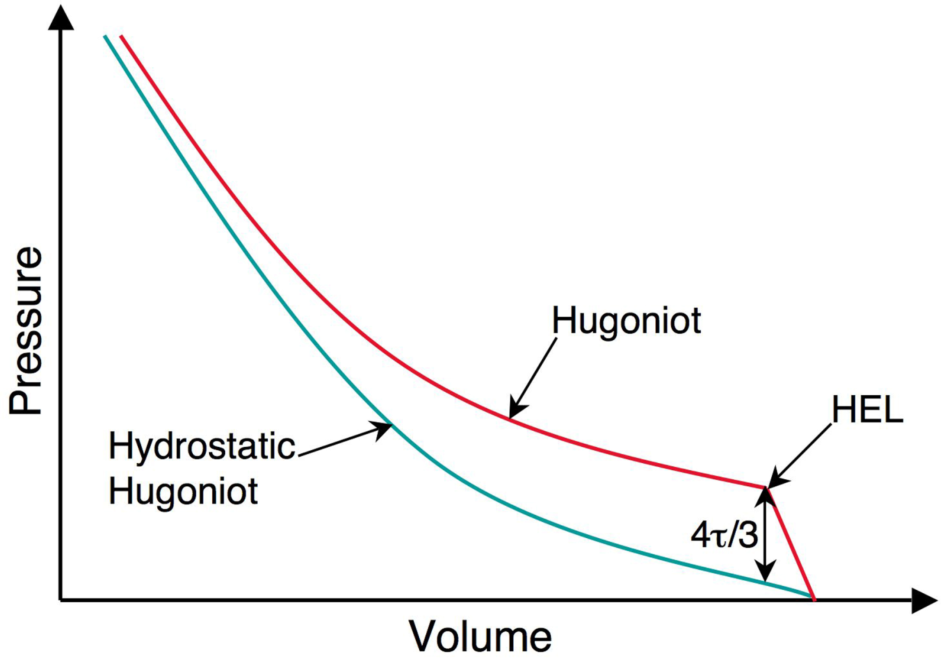

Figure 3.1. Hugoniot curve relative to the hydrostatic Hugoniot (often approximated by the material isentrope at low pressures). The pressure at the cusp of the Hugoniot is the Hugoniot Elastic Limit (HEL).

3.2 Elastic and Plastic Shock Regimes

The pressure region where the P-V Hugoniot of a material is a linear function of volume is called the elastic shock regime. The strain in the material is uniaxial along the direction of shock propagation and there is no transverse motion. Most importantly, the material deforms elastically during shock-loading restoring its initial state after shock release. The maximum pressure beyond which this elastic behavior ceases is the Hugoniot Elastic Limit (HEL). In the elastic shock regime the loading path (Rayleigh line connecting initial and final states) overlaps the Hugoniot. The speed of the elastic wave in the material is given by the longitudinal sound speed

$$c_l = \sqrt{\frac{\kappa + \frac{4}{3}G}{\rho_0}} \tag{3.9}$$

where κ the bulk modulus of the material defined by equation (2.3) and G the shear modulus. A comprehensive treatment of the elastic properties for different types of materials can be found in several materials science/metallurgy textbooks [46, 48]. From equation (2.20) it can also be shown that under uniaxial strain (and stress) conditions the pressure in the material is

$$P = \frac{V_0 - V}{V_0} \rho_0 c_l^2 . \tag{3.10}$$

The application of a compressive load below HEL leads to the generation of a single shock front with amplitude given by equation (3.10).

Above the HEL defect formation and propagation in the material causes the structure to deform in both the longitudinal and lateral directions to the shock front. Deformation in this pressure region becomes plastic, namely the material deforms irreversibly. Assuming the amplitude of the shock front to be higher than HEL, the speed of the plastic wave is defined by equation (2.1) that is the shear stresses are neglected.

Another attribute of the plastic shock regime that distinguishes it from the elastic shock regime is the presence of two separate shock fronts. Figure 3.2 elucidates this effect. For pressures less than P_{C} an elastic precursor wave is generated between the initial (P_0, V_0) state and the (P_A, V_A) state corresponding to the HEL pressure. A second (plastic) wave originates from (P_A, V_A) to the final state (P_B, V_B). Since the Rayleigh line connecting the states A and B has a smaller slope than that of the linear response region the plastic wave propagates at a lower speed than the elastic wave.

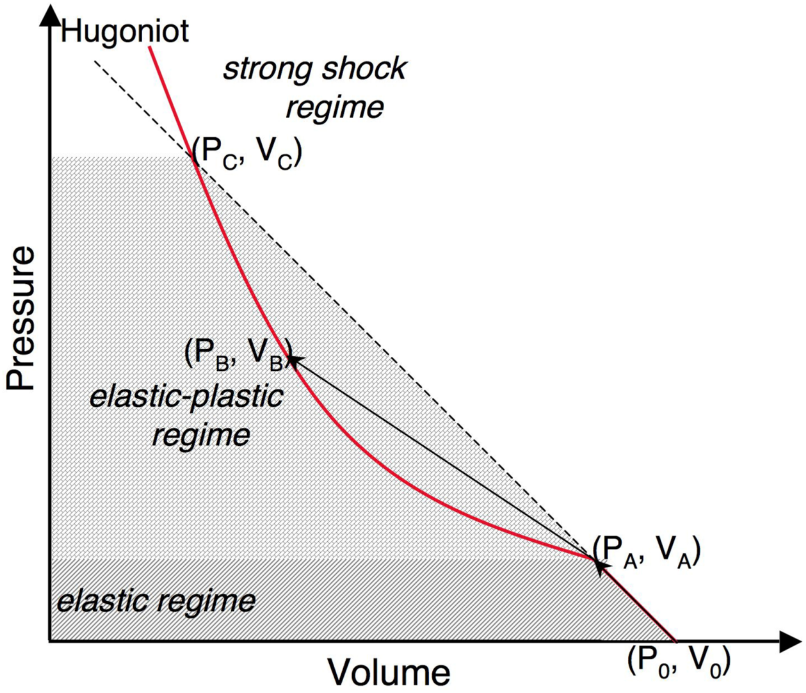
Hugoniot
strong shock regime
(P$_C$, V$_C$)
Pressure
(P$_B$, V$_B$)
elastic-plastic regime
(P$_A$, V$_A$)
elastic regime
Volume
(P$_0$, V$_0$)

Figure 3.2. Illustration of single shock wave generation in the elastic regime bounded by P_0-P_A. Shock wave splitting occurs for $P>P_A$ that is when the Hugoniot end state lies in the plastic regime. The elastic precursor has greater speed than the plastic wave indicated by the greater slope of the Rayleigh line in the elastic regime. For $P>P_C$ only a single plastic wave propagates in the material with speed greater than that of the elastic precursor.

In this example the elastic and plastic shock speeds are

$$U_A = V_0\sqrt{\frac{P_A - P_0}{V_0 - V_A}} \text{ and } U_B = V_A\sqrt{\frac{P_B - P_A}{V_A - V_B}} \text{ where } U_A > U_B. \qquad (3.11)$$

For pressures greater than P_C only a single shock exists. This is called the strong shock regime.

3.3 Strong Shock Regime

In the example presented above a single shock front is established when a material is shocked to a Hugoniot end state with $P > P_C$ assuming that material remains in its initial structural phase. However, shock Hugoniots may traverse a number of phase boundaries. If the target end state has $P > P_D$ shock wave splitting occurs in a similar manner as in the elastic-plastic regime (Figure 3.3). A mixed phase region results from shock pressures between P_E and P_F. A single shock front is present in phase 1 between pressures P_C and P_D and in phase 2 for $P > P_F$. The phase diagram and respective Hugoniot for the materials investigated is shown in Figure 3.4. Shock-loading Bi from ambient P-T is expected to result in multiple shock fronts as there is at least two low pressure solid-solid phase boundaries [50-55]. For this reason, shock melt investigations in Bi choose to access the melt region by preheating the Bi samples. At an elevated initial temperature a pressure of greater than 3 GPa is sufficient to achieve melt. On the other hand, Cu is a material where the shock Hugoniot does not encounter a phase boundary until about 230 GPa. This makes Cu a good material for studies of strength, elastic-plastic effects etc. [21, 56-58]. Melt however requires a shock of amplitude exceeding 230 GPa. Last, Mg has a phase diagram with both solid-solid and solid-melt phase transitions at easily accessible pressures by laser-induced shock-loading [59]. This is one of the reasons Mg was chosen for our study of shock-induced structural transitions.

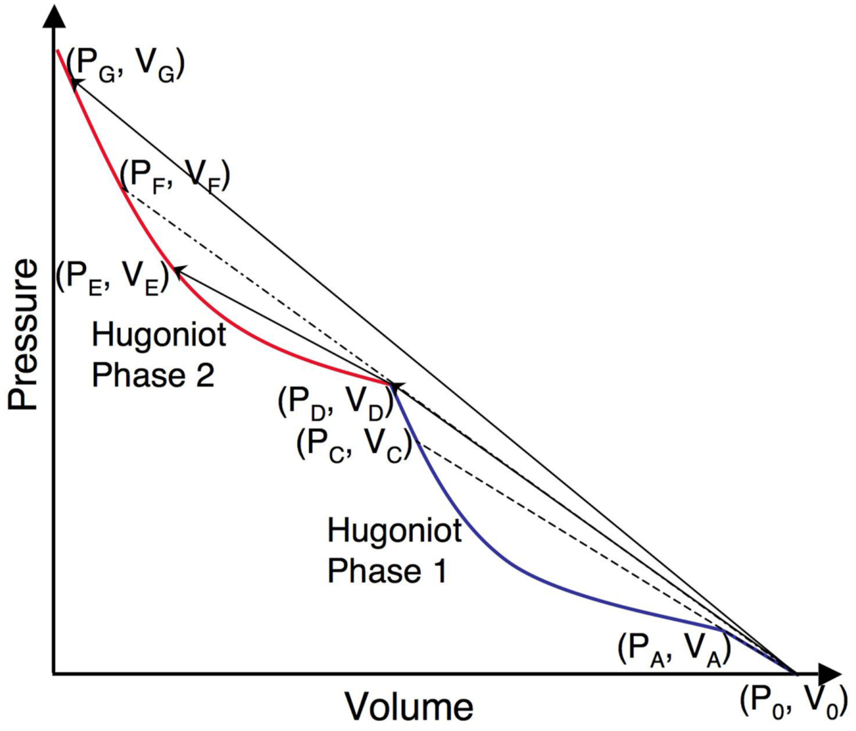

Pressure
Volume
(P_G, V_G)
(P_F, V_F)
(P_E, V_E)
Hugoniot Phase 2
(P_D, V_D)
(P_C, V_C)
Hugoniot Phase 1
(P_A, V_A)
(P_0, V_0)

Figure 3.3. ***P-V*** **diagram for a material for which shock compression provides access to two different phases. Similar to the elastic-plastic regime a double shock front results for** $P_C < P < P_F$**. The volume change between the two phases determines the extent of the shock wave splitting region as well as the difference in the speed of the shock fronts.**

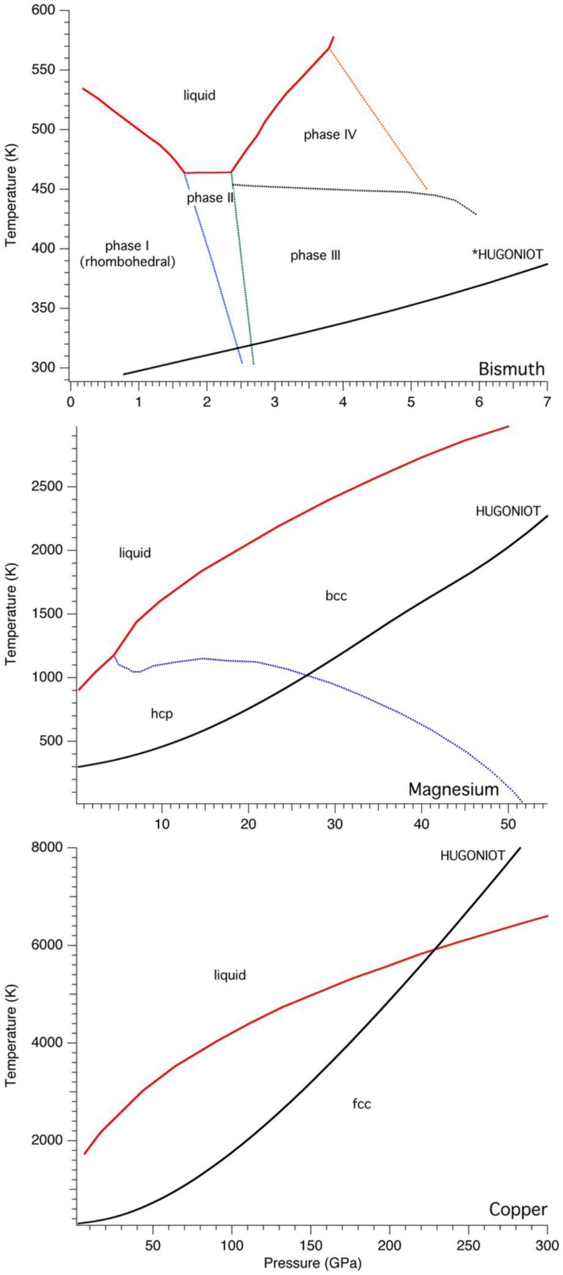

Figure 3.4. ***P-T*** **phase diagram and principal Hugoniot for Bi, Mg, and Cu. Intersection of the Hugoniot with a phase boundary results in the formation of a 2nd shock front.**

3.4 Shock-Induced Phase Transitions

3.4.1 THERMODYNAMICS OF PHASE TRANSITIONS

The equilibrium P-T phase diagram of materials has traditionally been investigated under static conditions. Most equilibrium experimental data has been obtained in diamond anvil cells where both pressure and temperature can be easily controlled. In our experiments, different regions in the P-T diagram of various materials were accessed dynamically via shock-loading. During shock-loading the timescale for structural changes to occur is of the order of the shock duration or less, namely subnanosecond. Therefore, the ultrafast timescales imposed by the loading mechanism make shock-induced phase transformations an extremely interesting topic. In this section, I will attempt to link equilibrium thermodynamics of phase transformations to the shock Hugoniot properties following closely the treatment of Duvall and Graham [60]. Even though shock-loading is fundamentally a non-equilibrium process, equilibrium thermodynamics can still be applied for gaining an insight into the concepts of phase stability, phase transition volume change, and the shock Hugoniot.

Phase stability, at constant temperature and pressure, occurs where the Gibbs free energy G is minimized. The definition of G(P,T) is

$$G = H - TS = E + PV - TS\,, \tag{3.12}$$

where H is the enthalpy, T the temperature, and S the entropy of the system. In differential form G is given by

$$dG = VdP - SdT \tag{3.13}$$

after substitution of the 1st law of thermodynamics for dE where

$$dE = TdS - PdV\ . \tag{3.14}$$

From (3.13) we can deduce the first derivatives of G with respect to pressure and temperature at constant T and P respectively

$$\left(\frac{\partial G}{\partial P}\right)_T = V \text{ and } \left(\frac{\partial G}{\partial T}\right)_P = -S\ . \tag{3.15}$$

Hence the slope of the Gibbs free energy as a function of pressure is equal to the volume at constant temperature (Figure 3.5). For first order phase transformations the slope becomes discontinuous at the phase boundary resulting in a volume change. A volume differential accompanies all first order phase transformations such as melting and solidification. In shock-induced transformations a volume change manifests itself as a “kink” in the velocity profile recorded by velocimetry (VISAR) due to shock wave splitting.

As it was shown in Chapter 2, particle velocity, the quantity typically measured by velocimetry, is proportional to the square root of the volume difference between the initial and final Hugoniot state. For the well-known $\alpha(\text{bcc}) \rightarrow \varepsilon(\text{hcp})$ phase transformation in Fe [61-64] the corresponding volume decrease is $\Delta V/V_0$=6.5%. Such volume change was detectable in velocity profile measurements performed by a number of research groups and for this reason a wealth of information exists on the bcc to hcp boundary in Fe even prior to the development of dynamic x-ray diffraction. On the other hand, phase transformations with an expected volume [65, 66] change of <1% such as the hcp to bcc in Mg are extremely challenging to diagnose. Thus, an estimate of the phase transition volume change is always useful in order to predict the presence or absence of a double shock front or "kink" in the particle velocity profile measurement.

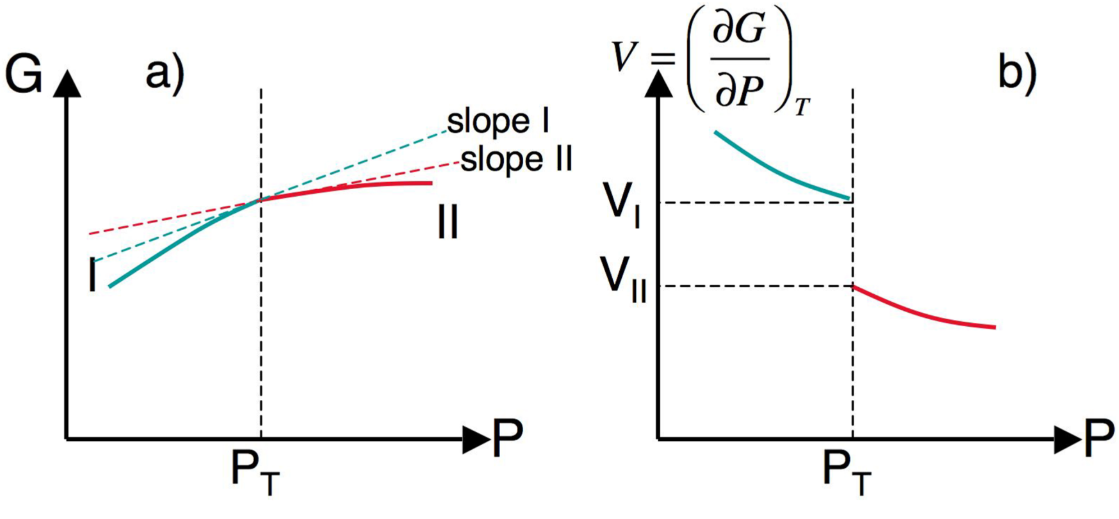

Figure 3.5. a) The Gibbs function G(P, T) at constant temperature for first order phase transformations. b) The origin of the volume discontinuity at the phase boundary of first order phase transformations is illustrated.

Having discussed the origin of the volume discontinuity in a first order phase transformation we now examine the thermodynamic behavior at a phase boundary. The criterion for equilibrium phase coexistence is

$$dG_I = dG_{II} \Rightarrow \tag{3.16}$$

$$V_I dP - S_I dT = V_{II} dP - S_{II} dT \tag{3.17}$$

The curve defined by the intersection of G_I and G_{II} is mathematically expressed by the Clausius-Clapeyron equation

$$\frac{dP}{dT} = \frac{\Delta S}{\Delta V} = \frac{\Delta H}{T\Delta V}\,. \tag{3.18}$$

Equation (3.18) describes the phase boundary in P-T space. ΔH represents the latent heat of the phase transformation. Depending on the slope of the phase boundary dP/dT can be either positive or negative. Assuming that $\Delta V<0$ for a shock compressed material, the shape of the Hugoniot for the cases where $\Delta S<0$ and $\Delta S>0$ is explained below (Figure 3.6).

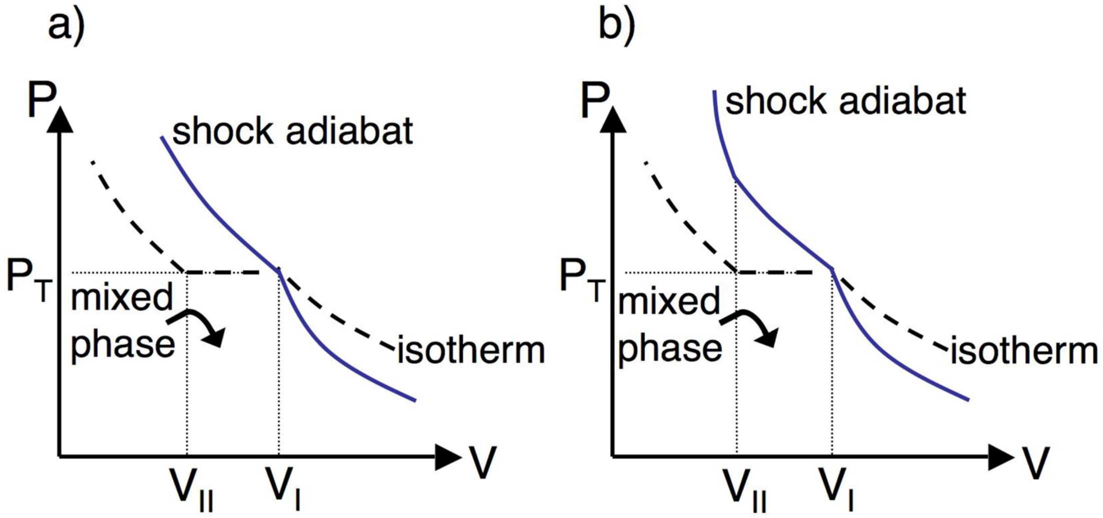

Figure 3.6. Pressure-volume plot of the isotherm and shock adiabat (Hugoniot) when a) $dP/dT>0$, $\Delta S<0$, $\Delta V<0$ and b) $dP/dT<0$, $\Delta S>0$, $\Delta V<0$.

To understand the features on the shock Hugoniot for materials undergoing a phase transformation we must first remind ourselves that the Hugoniot is not a thermodynamic path. However, the thermodynamic process at the shock front is assumed to be adiabatic. The shock Hugoniot (adiabat) for the case where $\Delta V<0$ and $\Delta S<0$ is shown in Figure 3.6a. From (3.18) such conditions imply that $dP/dT>0$ such as in the example of the solid-liquid phase boundary in Cu. The Hugoniot in this case exhibits a discontinuity at the onset of the phase transformation at V_I. A mixed phase region exists between V_I-V_{II}. Similarly, when $\Delta V<0$ and $\Delta S>0$, $dP/dT<0$. A decrease in temperature with increasing pressure is encountered in the negatively sloped boundary of the solid-liquid phases in Bi and the hcp-bcc phases in Mg. The second discontinuity in the Hugoniot slope at V_{II} can be explained by means of a P-V-T surface where the family of isotherms, having decreasing temperature as P increases, along with the Rankine-

Hugoniot curve are plotted [60]. In both cases a), b), stable two wave structures can be supported depending on the Hugoniot end state. It can also be observed that as V_I-V_{II} becomes smaller the phase coexistence region and the two-wave stability pressure range decreases.

3.4.2 KINETICS OF PHASE TRANSITIONS

The kinetics of first order phase transformations is a topic of great experimental and theoretical interest. In dynamic compression experiments the kinetics of non-equilibrium phase transformations can span timescales from μs to ps. For this reason, if there is no prior knowledge of the transformation mechanism and its corresponding timescale, detecting such transient processes becomes extremely challenging. In general, there are two broad classes of phase transformations: displacive and diffusional [67]. A type of displacive transformation is the so-called martensitic and it takes place with a well-defined crystallographic relationship between the parent and daughter phases. An example of this type of phase transformation is the hcp to bcc transition in Mg [68, 69]. The suggested mechanism, simulated by ab initio molecular dynamics calculations, consists of a distortion of the $(001)_{hcp}$ plane into the $(110)_{bcc}$ by displacement of the atoms in the B layer of the hcp structure (ABAB…) followed by shearing (Figure 3.7). Therefore there is a change in volume associated with this type of transformation which for Mg is ~ 1%.

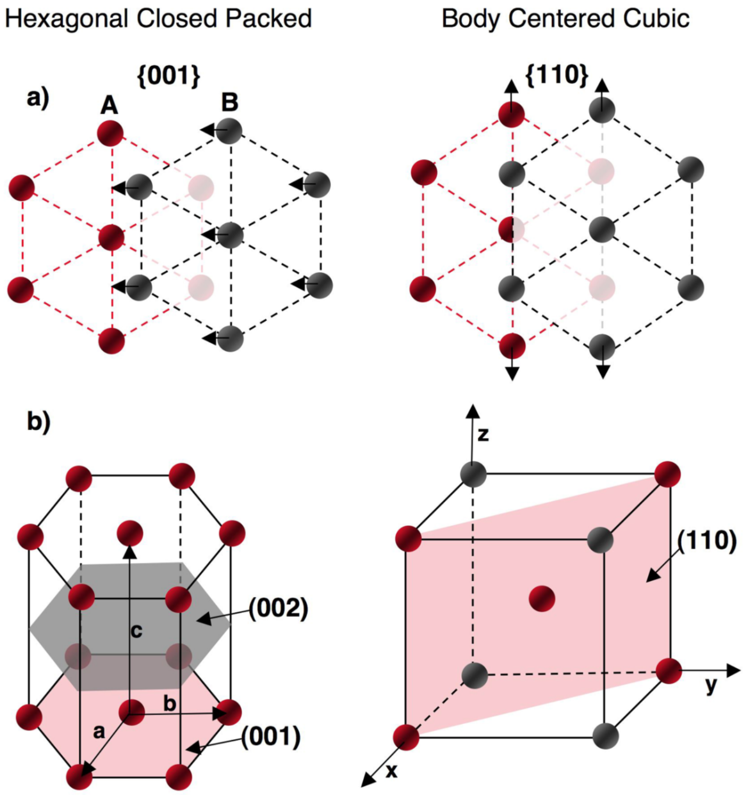

Figure 3.7. Illustration of the atomic re-arrangement that results in the hcp to bcc transformation in Mg. a) Atoms are initially displaced by an equal amount in layer B ((002) hcp plane). Further shearing brings the (100) hcp to coincide with the (110) bcc plane. b) 3D views of the corresponding planes in the hcp and bcc structure are shown.

On the other hand, in diffusional transformations there is no specific crystallographic correspondence between the initial and final phase. Diffusional transformations also occur at a much slower rate than displacive transformations and are not accompanied by a macroscopic change of shape. In general, the differences between displacive and diffusional transformations stem from the underlying phase nucleation and growth mechanisms. For this reason, I will briefly try to explain a simple model of nucleation and growth kinetics known as the Kolmogorov-Johnson-Mehl-Avrami

(KJMA) model [65, 66]. This model has successfully described a number of systems [70].

When a system is forced to transform from phase 1 to phase 2 by a sudden change in pressure and temperature conditions, small regions of phase 2 will start to form at a nucleation rate of $\gamma(t)$. These stable phase 2 domains will continue to grow isotropically at a rate u. At time t the radius of the domain that formed at t' becomes

$$r(t-t') = u \cdot (t-t') \tag{3.19}$$

The volume growth rate is then given by

$$w(t-t') = 4\pi u^3 (t-t')^2 \tag{3.20}$$

Now taking into account the nucleation rate of the phase 2 domains $\gamma(t)$ and the fact that phase 2 domains can only grow in the fractional volume occupied by phase 1, namely $v_1 = (1-v_2)$ we see that the fractional volume of phase 2 is

$$\frac{dv_2}{dt} = (1-v_2)\int_0^t w(t-t')\gamma(t')dt' \tag{3.21}$$

Assuming that at $t \to \infty$ the two phases coexist with equilibrium fractional volumes v_1^0 and v_2^0 equation (3.21) becomes

$$\frac{dv_2}{dt} = (v_2^0 - v_2)\int_0^t w(t-t')\gamma(t')dt' \tag{3.22}$$

Taking v_2^0 as a constant in time (3.22) can be integrated to result in a solution of the form

$$v_2(t) = v_2^0\left\{1 - \exp\left[-\left(\frac{t}{\tau}\right)^n\right]\right\} \tag{3.23}$$

where τ is the kinetic time constant. Depending on the nucleation process n can take values between 1-4. For homogeneous nucleation, a process having a time-independent growth rate γ=const., n varies between $3<n<4$. For heterogeneous nucleation, a process depending upon grain boundaries, impurities, and other defects in the material to initiate nucleation, $n<3$. In general, homogeneous nucleation is an extremely fast process. In studies of polycrystalline materials undergoing phase transformations (displacive or diffusional) phase nucleation at grain boundaries is the dominant mechanism. Furthermore, the KJMA model assumes no externally applied forces such as those of shock compression. To obtain kinetics information under such condition the KJMA model must be coupled to a hydrodynamics model.

3.5 Shock Generation via Laser Ablation

Investigating the response of materials under shock-loading requires the application of a well-characterized load. A number of loading techniques have been employed over the years each with their advantages and disadvantages. Projectile impact has been the most broadly used technique to generate shock fronts, employing gas guns [71], magnetically [72] or laser driven flyer plates [13], and explosives. This technique has been particularly valuable in high accuracy EOS measurements because of the planarity of the induced shock fronts. On the other hand, projectile impact has a lower limit on the timescales that can be investigated (typically microseconds). In addition, the maximum flyer plate velocity attainable is dependent on the material properties of the flyer plate (e.g. melting temperature of Al flyer plate) and for this reason, shock pressures are limited to <200 GPa.

Inducing shocks into a solid sample by direct laser irradiation [73] is a versatile technique for the study of dynamic material response. Depending on the laser source, loading timescales can be varied from microseconds to femtoseconds. The shock pressures achieved can easily exceed 500 GPa depending on the material Hugoniot. The main drawback however of laser-induced shock-loading is that of shock planarity which is critical for the accurate determination of the Hugoniot end states. To ensure planarity a sufficiently large laser spot diameter to sample thickness ratio must be used. In addition, beam smoothing techniques (such as phase plates) must be utilized to ensure a spatially uniform beam profile. A temporally constant shock profile is much more difficult to obtain as constant laser irradiance does not induce a constant pressure in the sample (see Chapter 7). For this reason hydrodynamics simulations are very useful in understanding the pressure history as a function of irradiance and position in the sample.

Despite the above difficulties, laser-induced shock-loading is still the most suitable technique for studying phenomena that occur at timescales within the rising edge of the shock front, such as elastic-plastic phenomena and phase transformations. Since these were the primary phenomena studied throughout my PhD research, in this section I will summarize briefly the processes involved in the laser-matter interaction that lead to shock wave formation.

3.5.1 MOMENTUM TRANSFER BY LASER ABLATION

In the experiments described later, a laser pulse of a few nanoseconds in duration is incident on a metal target to induce a shock wave (Figure 3.8). Energy is initially deposited within the skin depth of the material causing ablation on the surface of the material. Subsequently the laser energy is absorbed in the plasma formed via ablation near the critical plasma density n_{crit}. Momentum transfer from the plasma expanding into vacuum to the sample results in a forward moving shock front in the sample, similar to a rocket engine effect. To derive a scaling law between the incident laser intensity I and the ablation pressure P_a let us assume that a fraction α of the laser intensity is absorbed and converted to kinetic energy in the backward expanding plasma such that

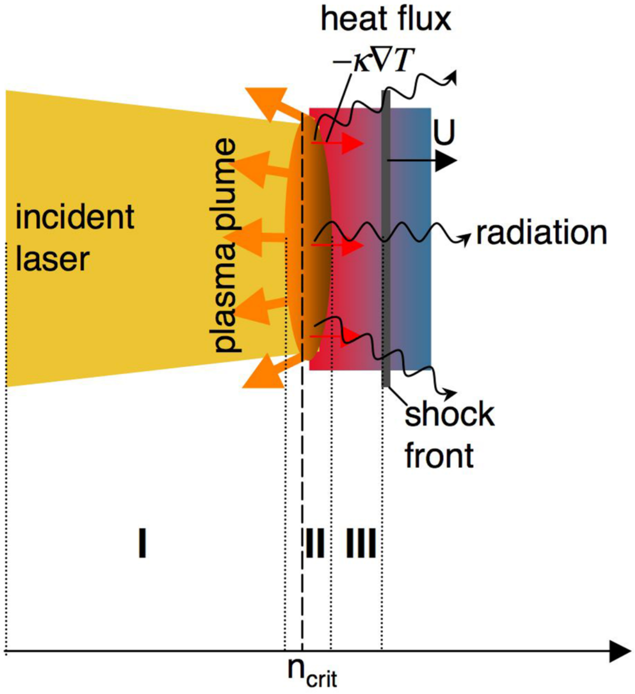
heat flux
$-\kappa\nabla T$
U
incident
laser
plasma plume
radiation
shock
front
I
II
III
n_{crit}

Figure 3.8. Illustration of the laser-target interaction leading to ablation on the target surface and subsequent formation of an expanding plasma. From conservation of momentum a forward propagating pressure wave is generated. Three regions of interest are shown. Region I: low density, collisionless plasma. Region II: dense, collisional plasma with density reaching a critical value at which laser light cannot penetrate further. Region III: compressed condensed matter phase due to shock-loading.

$$\alpha I = \alpha \frac{E}{At_{laser}} = \frac{1}{At_{laser}}\left(\frac{mv^2}{2}\right) \tag{3.24}$$

where A and E the laser spot area and energy respectively and t_{aser} the laser pulse duration. Since the ablated mass flux is related to the density ρ and ion velocity v by

$$\frac{m}{At_{laser}} = \rho v \tag{3.25}$$

(3.24) can be simplified to

$$\alpha I = \frac{\rho v^3}{2}. \tag{3.26}$$

Conservation of momentum (or Newton's 3rd law) requires that a forward pressure front is generated in the sample in reaction to the backward expanding material. The amplitude of this ablation-induced pressure P_a is then given by

$$P_a = \rho v^2 = \rho^{1/3}(2\alpha I)^{2/3}. \tag{3.27}$$

Equation (2.37) associates the ablation pressure in a sample to the incident laser intensity with a power 2/3 scaling. From empirical and theoretical models the simplified rocket engine model generally overestimates the ablation pressure as function of laser intensity. The overestimated pressure scaling could be attributed to the fact that the absorbed laser energy has been applied solely towards the kinetic energy of the ions in the plasma, omitting processes such as heat conduction and thermal radiation. A comprehensive treatment of the ablation pressure as a function of irradiance for a number of materials using a 1D radiation hydrodynamics code (HYADES) can be found in [74]. In Chapter 7 simulations using the same hydrocode will be presented for the materials studied. The processes of laser absorption, heat conduction, and thermal radiation are discussed next.

3.5.2 LASER ABSORPTION IN A PLASMA

The rocket engine model presented above provides an approximate scaling of the ablation pressure with laser intensity if the ablation mass density ρ (or ion density) and absorption coefficient α are known. We can obtain values for these coefficients by looking more closely into the interaction of the laser field with the ablation/plasma front [75].

After the initial breakdown of the target surface the laser energy does not reach the ablation front any longer. Instead it is deposited in the expanding plasma formed whose density variation can be described by the three different regions. Region I, consists of a low density collisionless plasma where the Debye length λ_D is much greater than the ion spacing R where

$$\lambda_D = \sqrt{\frac{kT_e}{4\pi n_e e^2}} \text{ and } R = \left(\frac{3}{4\pi n_i}\right)^{1/3}. \tag{3.28}$$

Region II is the area of a dense collisional plasma with Debye length comparable to the distance of neighboring ions. In this strongly coupled plasma, where Γ the plasma coupling parameter

$$\Gamma = \frac{E_P}{E_T} = \frac{\left(Z^* e\right)^2}{RkT_i} \gg 1\,, \tag{3.29}$$

the plasma density gradient reaches the critical electron density for the incoming laser light. Since the critical density

$$n_{crit} = \frac{\pi m_e c^2}{e^2 \lambda_{Laser}^2} \simeq \frac{1.1 \times 10^{21}}{\lambda[\mu m]_{Laser}^2} \tag{3.30}$$

is the maximum density the laser light can penetrate we can assume that the laser energy is mostly deposited in the plasma near n_{crit}. Therefore, the ablation mass ρ can be approximated to

$$\rho = \frac{n_{crit}}{Z^*} \tag{3.31}$$

where Z^* the ionic charge state. In addition, since in Region II collisional processes dominate we can assume that Inverse Bremsstrahlung (IB) [76-79] is the primary absorption mechanism in the plasma in Region II.

nverse Bremsstrahlung refers to the process in which an electron absorbs a radiation as it scatters in the Coulomb field of an ion. For an exponential electron density profile

$$n_e = n_{crit} \exp\left[-\frac{z}{L}\right] \tag{3.32}$$

the absorption factor *a* [80] is given by

$$\alpha = 1 - \exp\left[-\frac{8 L v_{ei}^{crit}}{3c}\right] \tag{3.33}$$

where ${v^{crit}}_{ei}$ the electron-ion collision frequency at the critical density and L the plasma scale length. Experimentally the fraction of laser energy absorbed in Region II can the inferred from measurements of the scattered light. The fractional amount of energy absorbed is subsequently transported by thermal conduction and radiative heat transport to the ablation front. Therefore, three temperature (ions, electrons, radiation) hydrocode simulations taking into account thermal conduction and radiation diffusion are required to relate the absorbed laser intensity in the expanding plasma to the ablation pressure in the material.

Region III represents the shock-compressed condensed phase whose temperature can be found by measurement of the Hugoniot end state. The propagation of a thermal wave behind the shock front and the radiation from the material is described next.

3.5.3 HEAT CONDUCTION

As mentioned earlier, the energy absorbed at the plasma critical density is carried to the solid target (ablation) surface by electron transport. The build up of “hot” electrons at the ablation surface results in a thermal gradient ∇T and subsequently a thermal wave towards the cold, lower density region of the target. In lattice measurements of shock-compressed solids, it is critical that the interplanar spacing measured by x-ray diffraction corresponds to the lattice strain induced by the shock only. A thermal wave can cause the lattice to expand, which would result in an error in our lattice measurement under shock compression.

Assuming $\frac{\nabla T_e}{T_e} \ll 1$ (diffusive heat transport) as well as Maxwellian electron distribution function, the Spitzer thermal conductivity [81]

$$\kappa_e = \gamma_0 \frac{3}{4} \frac{1}{(2\pi)^{1/2}} \frac{k_B}{m_e^{1/2} Z^* e^4 \ln \Lambda_C} (k_B T_e)^{5/2} \tag{3.34}$$

can be inserted into the equation for conductive heat flux

$$\bar{S} = -\kappa_e \nabla T_e \tag{3.35}$$

where γ_0 (~1) the Spitzer factor depending on the ionization state Z^* and $\ln\Lambda_C$ the Coulomb logarithm. Considering diffusion in one direction e.g. in x, (3.35) can be written as

$$S = C(k_B T_e)^{5/2} \frac{\delta T_e}{\delta x} \approx C(k_B T_e)^{5/2} \frac{T_e}{x_f} = \frac{C}{k_B}(k_B T_e)^{7/2} \frac{1}{x_f} \tag{3.36}$$

where C a constant composed of the conductivity terms in (3.34) left of $\left(k_B T_e\right)^{5/2}$. From energy conservation the conductive heat flux in the sample can be equated to the thermal energy density of an ideal gas. Since the latter is equal to

$$S = \frac{3}{2} n_e k_B T_e \frac{x_f}{t} \tag{3.37}$$

it can be shown by substituting with

$$k_B T = \frac{2}{3} \frac{St}{x_f} \frac{1}{n_e} \tag{3.38}$$

into (3.36) that

$$x_f \propto t^{\frac{7}{9}} \tag{3.39}$$

where x_f the position of the heat front along the x direction. The above relation indicates that the thermal wave front has a sublinear dependence on time (Figure 3.9). On the other hand the position of a shock front $x_s = Ut$ depends linearly on time, which implies that the shock front will overtake the thermal front at some point in time. The distance in the sample at which this happens is equal to

$$
\begin{aligned}
x_{shock=heat} &= \left(\frac{2}{3}\right)^{7/9}\left(\frac{C}{k_B}\right)^{7/9}\frac{1}{n_e^{7/9}}S^{5/9}\left(\frac{x_{shock=heat}}{U}\right)^{7/9} \Rightarrow \\
x_{shock=heat} &= \left(\frac{2}{3}\right)^{7/2}\left(\frac{C}{k_B}\right)^{7/2}\frac{1}{n_e^{7/2}}S^{5/2}\frac{1}{U^{7/2}}
\end{aligned}
\quad . \tag{3.40}
$$

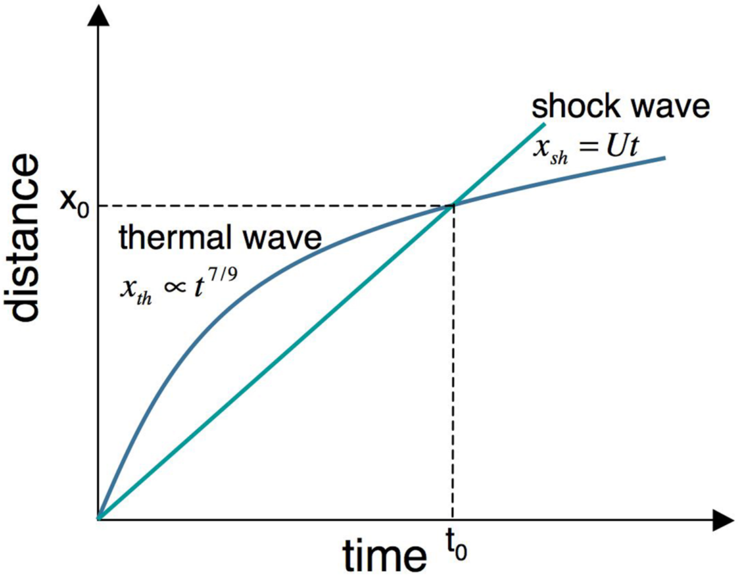

Figure 3.9. The x-t relation for a steady heat conduction front where gradT/T«1. The shock front eventually catches up with the heat front at distance x_0.

3.5.4 EQUILIBIRUM RADIATION TRANSPORT

Blackbody radiation emission in shock-compression is encountered in the context of both a plasma in thermal equilibrium and a shock-heated solid in thermodynamic equilibrium. In the former, radiation heat transport in the ablation plasma contributes to the formation of the shock front. In the material at solid density the radiation mean free path is very small, so radiation transport can be "switched-off" in hydrocode simulations of the shock propagation in the compressed solid. On the other hand, the spectral emissivity [82] of a target heated by the shock front can yield important information about the Hugoniot state. There have been a number of studies, especially in shock-induced phase transformations, where time-resolved pyrometry [83-85] has been implemented in order to measure the temperature profile during loading and release of the shock pressure. In general, it is assumed that the states across the P-V-T discontinuity are in thermodynamic equilibrium so that the Hugoniot jump conditions apply.

Thermodynamic equilibrium implies that emission from the shock-heated target is isotropic. For radiative equilibrium the spectral energy density function, namely the energy per volume per unit frequency interval for a frequency ν is given by Planck's law

$$U_{\nu}(\nu) = \frac{8\pi h\nu^{3}}{c^{3}} \frac{1}{e^{\frac{h\nu}{kT}} - 1} . \tag{3.41}$$

Defining $x = \dfrac{h\nu}{kT}$ and performing integration over dx from 0 to ∞ results in an equilibrium spectral energy density

$$U = \frac{4\sigma}{c} T^{4} = 1.37 \times 10^{2} T[eV]^{4} [erg / cm^{3}] \tag{3.42}$$

where $\sigma = \frac{2\pi^5 k^4}{15h^3c^2}$ is the Stefan-Boltzman constant. It can be shown that spectral energy density maximizes at

$$h\nu = 2.822kT \text{ or } \lambda_{peak} = \frac{2898[\mu m]}{T[K]}. \tag{3.43}$$

Because of (3.35) (Wien's displacement law), there is a lower boundary to the temperatures that can be detected based upon the spectral sensitivity of current pyrometric detectors. This limit is at ~ 1eV which corresponds to a peak emission wavelength of 250 nm. For the temperatures relevant to our experiments measurement of the spectral emission would have been very difficult as the peak emission wavelength would have been around 2-6 μm.

4 X-RAY DIFFRACTION FUNDAMENTALS

The principal experimental goal of this dissertation was to identify shock-induced phase transitions via a time-resolved measurement of the lattice. This goal was achieved by developing x-ray diffraction instrumentation and by applying fundamental x-ray scattering principles to extract information about the atomic arrangement from the captured x-ray signal.

In this chapter, a basic background on x-ray diffraction is presented. A description of the pertinent crystal structures is provided at the start of the chapter followed by an explanation of the Bragg and Laue formulations used in relating diffraction peak position to the lattice plane origin of the diffracted signal. The diffraction peak intensity is qualitatively discussed including crystal (structure factor) and x-ray energy specific factors. Absorption of x-rays as a function of material atomic number Z and x-ray energy is also presented to assess x-ray penetration depth and x-ray filter attenuation for the different x-ray sources used in this study.

Having provided a basic x-ray diffraction background, the effects of lattice compression on the x-ray diffraction signal are presented. The macroscopic material response discussed in Chapter 3 is associated to microscopic lattice measurements. Specifically, a relationship between interplanar lattice spacing and density for the cases of uniaxial and hydrostatic compression is derived. Last, the nanosecond laser-plasma x-ray sources used to probe the lattice during shock compression are described.

4.1 Geometric Description of Crystals

Designating lattice planes and directions within crystal structures is important to both experimental aspects of x-ray diffraction and in describing structure-dependent physical properties. For example, in single crystal x-ray diffraction knowledge of the sample orientation, namely the lattice plane parallel to which the samples are cut and polished from the crystal rod is critical for detector and x-ray source alignment. In addition, the sample orientation is equivalent to the shock propagation direction in ablatively driven shocks, as planar shocks always traverse the sample in a direction normal to the ablated surface. Therefore, in studies of effects with an orientation dependence such as phase transformation mechanisms or slip systems responsible for plastic deformation, a well-characterized sample is crucial to the observed effects and their interpretation.

In this section a description of the crystal structures present in our experiments is given. For Cu and Mg the relevant crystal structures are face centered cubic (fcc), hexagonal close packed (hcp) and body centered cubic (bcc) (after phase transition).

4.1.1 CUBIC LATTICES

In crystallography, a Bravais lattice refers to a periodic array on which single atoms, unit cells, or groups of atoms are attached in a repeated fashion [86, 87]. The Bravais lattice is described by a position vector

$$\vec{R} = m\vec{a}_1 + n\vec{a}_2 + k\vec{a}_3 \qquad (4.1)$$

where m, n, k are integers and $\vec{a}_1$, $\vec{a}_2$, $\vec{a}_3$ are the primitive vectors. These vectors span all Bravais lattice points as *m*, *n*, *k* are varied. For a simple cubic structure the primitive vectors are orthogonal ($\hat{x}$, $\hat{y}$, $\hat{z}$ directions) and have magnitude equal to the length of the cubic cell *a*. An fcc unit cell can be constructed from the simple cubic cell by adding one atom at the center of each of the six faces (Figure 4.1).

The fcc lattice can be represented by the symmetrical primitive vectors

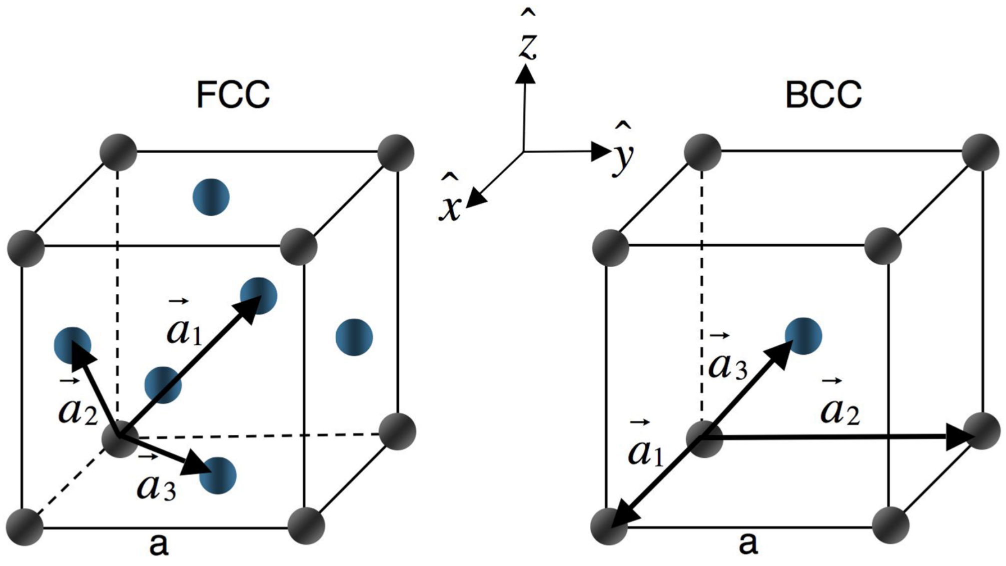

Figure 4.1. Illustration of the conventional FCC and BCC unit cell. The primitive vectors for each lattice structure are also drawn. The additional atoms in the FCC and BCC unit cell compared to a simple cubic cell are shown in blue. Note that the unit cells contain 4 atoms (FCC) and 2 atoms (BCC) .

$$\vec{a}_1 = \frac{a}{2}\left(\hat{y} + \hat{z}\right), \vec{a}_2 = \frac{a}{2}\left(\hat{z} + \hat{x}\right) \text{ and } \vec{a}_3 = \frac{a}{2}\left(\hat{x} + \hat{y}\right). \tag{4.2}$$

The selected fcc unit cell shown here contains four atoms ($\frac{1}{2}\times 6+\frac{1}{8}\times 8$ atoms= 4 atoms). Similarly, the bcc unit cell can be considered as a simple cubic cell containing an additional atom in the center of the cube ($1+\frac{1}{8}\times 8$ atoms= 2 atoms). The primitive vectors for the bcc lattice shown here are

$$\vec{a}_1 = a\hat{x},\ \vec{a}_2 = a\hat{y} \text{ and } \vec{a}_3 = \frac{a}{2}\left(\hat{x}+\hat{y}+\hat{z}\right). \tag{4.3}$$

A table with lattice parameters for cubic metals is shown below. This table will become useful in the calculation of diffraction peak positions later.

Table 4.1 Lattice parameter *a (*Å*)* for representative elements with FCC or BCC crystal structure. [86]

Material	*a* (Å)	Lattice
Al	4.05	FCC
Cu	3.61	FCC
Fe	2.87	BCC
Ta	3.31	BCC
V	3.02	BCC

Designating planes and directions in cubic systems is quite simple. A procedure can be applied to all structures, regardless of the axial coordinate system, known as the Miller index notation. For plane indexing, the intercepts of the plane with the axis coordinates are initially determined. Then the reciprocals of the intercepts are taken and cleared of the fractions so that a set of (*hkl*) integers can be found. Similarly, the Miller index notation for directions dictates that the vector in the desired direction is First expressed in terms of a fraction of the axial coordinates. These fractions are subsequently cleared to result in a set of integers [*UVW*] (Figure 4.2).

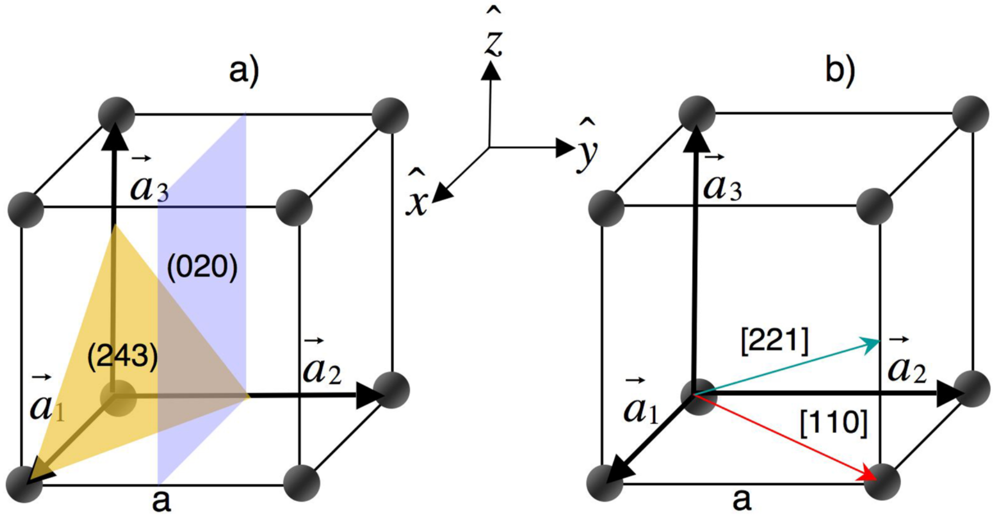

Figure 4.2. Example of crystallographic indexing of a) planes and b) directions. In a) the plane shaded in yellow is the (243) as it intercepts the axial coordinates at 1, 1/2 and 2/3. The plane shaded in purple is the (020) since it intercepts the axes at ∞, 1/2 and ∞. In b) the [110] and [221] directions are shown. For vector [110] the x and y axis intercept is at 1, and z axis intercept at 0. For vector [221] the corresponding x-y-z intercepts are at 1, 1, and 1/2 respectively.

A useful parameter in x-ray diffraction calculations is the interplanar spacing d_{hkl} [88, 89]. For cubic structures

$$\frac{1}{d_{hkl}^2} = \frac{h^2 + k^2 + l^2}{a^2}. \tag{4.4}$$

It is instructive to demonstrate the derivation of d_{hkl} so that it can be calculated for any other crystal structure. As we will see later, evaluating d_{hkl} for a given lattice structure is essential in x-ray diffraction calculations of peak position and lattice compression. From Figure 4.2 and the description of Miller indexing we note that the planes described by (*hkl*) intercept the crystallographic axes at $\frac{|\vec{a}_1|}{h}, \frac{|\vec{a}_2|}{k}, \frac{|\vec{a}_3|}{l}$. If $\hat{n}$ is a unit vector normal to (*hkl*), the perpendicular distance d_{hkl} between parallel (*hkl*) planes becomes

$$d_{hkl} = \frac{\vec{a}_1}{h} \bullet \hat{n} \,. \tag{4.5}$$

Our aim now is to find an expression for $\hat{n}$. We define a vector $\vec{K}$ such that

$$\vec{K} = h\vec{b}_1 + k\vec{b}_2 + l\vec{b}_3 \tag{4.6}$$

where the vectors $\vec{b}_1, \vec{b}_2, \vec{b}_3$ correspond to the reciprocal lattice vectors

$$\vec{b}_1 = 2\pi \frac{\vec{a}_2 \times \vec{a}_3}{\vec{a}_1 \bullet \vec{a}_2 \times \vec{a}_3},\ \vec{b}_2 = 2\pi \frac{\vec{a}_3 \times \vec{a}_1}{\vec{a}_1 \bullet \vec{a}_2 \times \vec{a}_3},\ \vec{b}_3 = 2\pi \frac{\vec{a}_1 \times \vec{a}_2}{\vec{a}_1 \bullet \vec{a}_2 \times \vec{a}_3} \,. \tag{4.7}$$

By definition, the reciprocal lattice vectors are orthogonal to the primitive vectors of different index so that

$$a_i \bullet b_j = \begin{cases} 2\pi, & i = j \\ 0, & i \neq j \end{cases} \,. \tag{4.8}$$

From the orthogonality condition (4.8), it can be shown that the vector $\vec{K}$ is normal to a plane (*hkl*) and therefore the unit vector $\hat{n}$ becomes

$$\hat{n} = \frac{\vec{K}}{|\vec{K}|} \tag{4.9}$$

The perpendicular distance d_{hkl} can then be expressed in terms of the reciprocal lattice vector $\vec{K}$ as

$$d_{hkl} = \frac{\vec{a}_1}{h} \bullet \hat{n} = \frac{\vec{a}_1}{h} \bullet \frac{h\vec{b}_1 + k\vec{b}_2 + l\vec{b}_3}{|\vec{K}|} = \frac{1}{|\vec{K}|} \,. \tag{4.10}$$

In general, the reciprocal lattice formulation is very important in x-ray diffraction problems, as it will become obvious within Bragg's law derivation. Once the primitive lattice vectors are known, a map of the reciprocal space can be drawn. Within this map a vector drawn from the origin to any point is then the vector $\vec{K}$, whose length is equal to the reciprocal of the real lattice spacing and its direction is orthogonal to the corresponding (*hkl*).

4.1.2 HEXAGONAL CLOSE PACKED LATTICE

Besides cubic lattice structures a significant amount of effort was devoted in understanding x-ray diffraction patterns from Mg, an element with a hexagonal close packed structure at room temperature and pressure. The unit cell in hcp is defined by the coplanar (basal plane) vectors $\vec{a}_1$ and $\vec{a}_2$ at 120° with respect to each other and a third normal axis defined by a vector $\vec{c}$ (Figure 4.3). The hexagonal symmetry of the lattice implies that a rotation of 60° around the c-axis will result in an identical lattice. Because of this 6-fold rotation symmetry the Miller indexing scheme applied to cubic structures is in some cases inconvenient since it makes the prismatic planes, i.e. the planes vertical to the basal plane, indistinguishable. For this reason, a redundant axis $\vec{a}_3$ is introduced as seen in Figure 4.3. The index *i* of this additional axis is related to *h*, *k* by

$$i = -(h + k)\,. \tag{4.11}$$

In terms of directions, the 3-indexing system is the most practical. In the Miller indexing system $\vec{a}_1$, $\vec{a}_2$, $\vec{a}_3$, and $\vec{c}$ are given by

$$a_1 = [100],\ a_2 = [010],\ a_3 = [1-10],\ \text{and } \mathrm{c} = [001]\,. \tag{4.12}$$

However, sometimes x-ray diffraction measurements from hcp structures are quoted using a 4-index system. Translating [*UVW*] to [*uvtw*] notation can be accomplished via the following transformations

$$u = \frac{1}{3}(2U - V),\ v = \frac{1}{3}(2V - U),\ t = -\frac{1}{3}(V + U),\ \text{and } w = W\,. \tag{4.13}$$

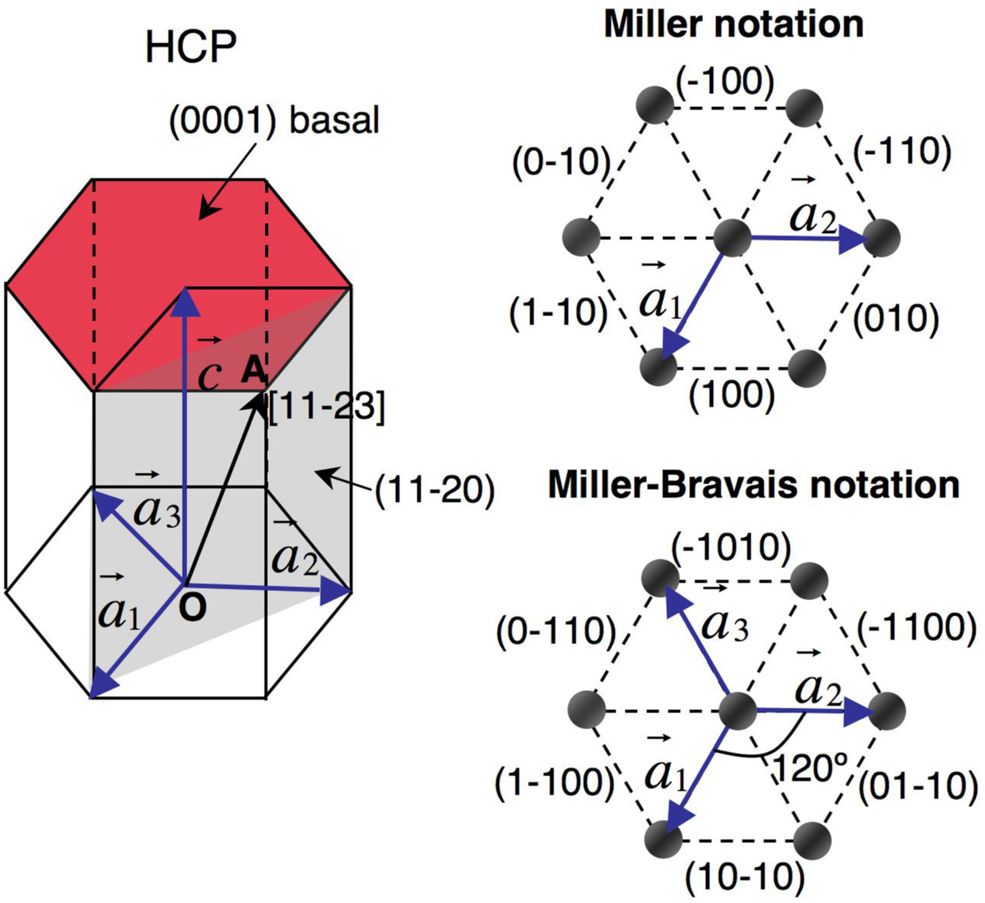
HCP
(0001) basal
$\vec{c}$
A
[11-23]
(11-20)
$\vec{a}_3$
$\vec{a}_2$
$\vec{a}_1$
O
Miller notation
(-100)
(0-10)
(-110)
$\vec{a}_2$
$\vec{a}_1$
(1-10)
(010)
(100)
Miller-Bravais notation
(-1010)
(0-110)
(-1100)
$\vec{a}_3$
$\vec{a}_2$
$\vec{a}_1$
120°
(1-100)
(01-10)
(10-10)

Figure 4.3. Illustration of the hexagonal close packed unit cell and its indexing notation. On the left, the hcp unit cell is outlined by a parallelepiped. The basal plane containing the 3 out of 4 primitive vectors is shown in red. On the right, the 3 and 4-index notation is demonstrated for the prismatic planes forming the basal plane hexagon.

As an example the $\vec{a}_1 = [100]$ lattice vector in terms of the 4-index notation becomes $[2-1-10]$. For the purposes of our data analysis, hcp planes and coordinates will be quoted in the 3-index system. The perpendicular lattice spacing in the hcp lattice can be derived from equation (4.10) to be

$$\frac{1}{d_{hkl}^2} = \frac{4}{3}\left(\frac{h^2 + hk + k^2}{a^2}\right) + \frac{l^2}{c^2}. \tag{4.14}$$

The lattice parameters of Mg and other hexagonal materials of interest are shown in the table below.

Table 4.2 Elements with hexagonal close packed crystal structure.

	***a* (Å)**	***c* (Å)**	***c*/*a***
Be	2.29	3.58	1.56
Mg	3.21	5.21	1.62
Ti	2.95	4.69	1.59

Note that the ideal *c*/*a* ratio in a perfect hcp lattice is 1.633. An hcp structure with a distorted unit cell will have a *c*/*a* ratio that deviates from the ideal value as seen for Be and Ti. The deviation from the static *c*/*a* ratio under compression is a measurement of great interest as the anisotropic behavior of the material upon compression or in other words its strength can be quantified. From Table 4.2 the Mg *c*/*a* ratio is very close to the ideal value. In general, studies of compressed Mg examining the variation of the *c*/*a* have shown only small deviation from the static *c*/*a* ratio.

4.2 X-Ray Diffraction from Crystals

Determining the lattice structure in materials where the interatomic spacing is of the order of a few Angstroms (10^{-10} m) requires electromagnetic radiation with a corresponding energy of several keV ($E = \frac{hc}{\lambda \sim 10^{-10}}$), namely x-ray radiation. In this section, an introduction to x-ray diffraction applicable to both single crystal and polycrystalline materials is presented [88, 89]. We will begin by associating diffraction peak position and crystal structure via Bragg's law. Even though absolute measurement of the diffraction peak intensity was not important for the structural effects studied, a qualitative description of the factors affecting diffraction peak intensity is included. Especially the structure factors of Mg and Cu are derived to indicate the diffraction peaks expected to be detected, allowing texture effects to be evaluated. Last, material Z and wavelength dependent absorption of x-rays and its application to filtering x-ray background signal is discussed.

4.2.1 BRAGG'S LAW

A very useful relation in x-ray diffraction linking the diffraction angle θ, the interplanar spacing d_{hkl} and the x-ray wavelength λ is Bragg's law. W. L. Bragg formulated that for intense diffraction peaks to be observed (Bragg peaks) from scattered radiation originating from parallel planes of ions, the following criteria must be met: 1) x-rays must be specularly reflected from the lattice planes and 2) the reflected x-rays from successive planes should interfere constructively. The latter criterion is illustrated in the figure below (Figure 4.4).

An incident x-ray in the direction of the unit vector $\vec{s}_0$ scatters from the planes denoted as A and B in the direction of the unit vector $\vec{s}$. Assuming specular reflection, the incident and reflected angles are equal to 90° - θ. From geometry, the path difference $\overline{KL} + \overline{LM}$ between the x-rays reflected from the adjacent parallel planes is

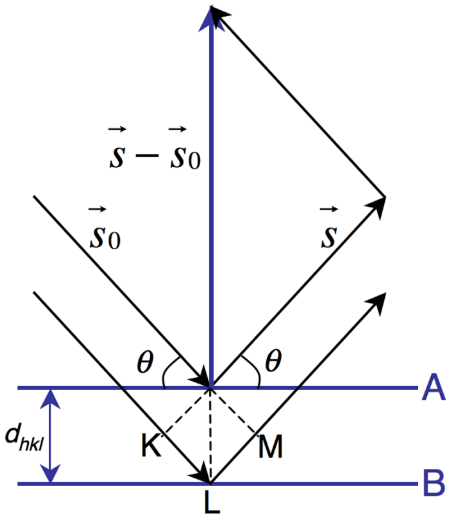

Figure 4.4. Schematic of Bragg diffraction from consecutive (hkl) planes. The difference between the incident and reflected unit vectors corresponds to a vector normal to the planes from which the diffraction condition is satisfied.

$$\overline{KL} + \overline{LM} = 2d_{hkl}\sin\theta\,. \tag{4.15}$$

For constructive interference to occur the path difference must be equal to an integer multiple of the wavelength λ or

$$2d_{hkl}\sin\theta = \lambda \tag{4.16}$$

where the integer multiple is incorporated within d_{hkl}. This simple law leads to an essential understanding of diffraction patterns from polycrystalline and single crystal materials as well as the diffraction geometries required to successfully probe such materials. Bragg's law dictates that to observe diffraction from a given plane (*hkl*) either λ or θ must be varied. Below are some examples where this principle is applied.

In single crystal diffraction, a collimated x-ray source of monochromatic radiation (fixed λ) incident on a sample will diffract from a plane (*hkl*) only when the sample is oriented at the correct angle θ. To form a diffraction pattern from such geometry the sample must be rotated with respect to the x-ray source (vary θ). To avoid rotation of the sample, a process that is generally quite time-consuming, diffraction patterns from stationary single crystals can be generated using a collimated broadband source (variable λ) (Figure 4.5). The resulting diffraction pattern is a set of dots each corresponding to a specific (*hkl*) plane and x-ray wavelength λ. An alternative single crystal x-ray diffraction method employs a monochromatic (fixed λ) point x-ray source allowing θ to vary over 4π. Intersection of the diffracted rings with planar x-ray detectors results in the diffraction pattern shown here for Bi in Figure 4.5.

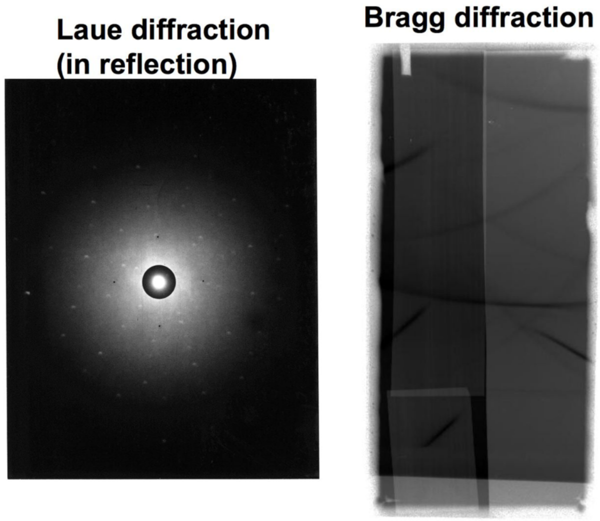

Laue diffraction (in reflection)

Bragg diffraction

Figure 4.5. Laue and Bragg diffraction from single-crystal Bi sample. In the Laue configuration variation in x-ray wavelength is provided by a broadband x-ray source, whereas the sample and source position is fixed. In Bragg diffraction the wavelength is fixed by the monochromatic x-ray source (4.7 keV) whereas a variable angular orientation between the x-rays and sample is provided by a point source emitting over 4π.

On the other hand, polycrystalline samples composed of randomly oriented crystallites (grains) when probed by a collimated monochromatic x-ray source yield diffraction patterns as a result of the variation in angle amongst the grains. Depending on the grain size the diffraction rings recorded can exhibit discontinuities as demonstrated in the figures below. Here Sn and Bi were sputter coated on single crystal LiF substrates. The coating parameters (temperature of the substrate and sputter rate) in the first case resulted in grains as large as 25 μm (Figure 4.6). When probed by a quasi-monochromatic 4.75 keV source the diffraction pattern appeared to be interrupted which is a significant disadvantage for shock compression experiments, since a continuous diffraction ring is necessary in order to check for anisotropies in compression (measurement of strength). On the other hand, large grain size samples may be useful for experiments investigating dynamic grain rotation or texture evolution. In the case of sputter coated Bi on LiF, coating parameters were adjusted such that grains <5 μm were produced. This was verified from the continuity of the Bragg peaks observed (Figure 4.7).

Polycrystalline sample: large grains

Polycrystalline Bragg diffraction

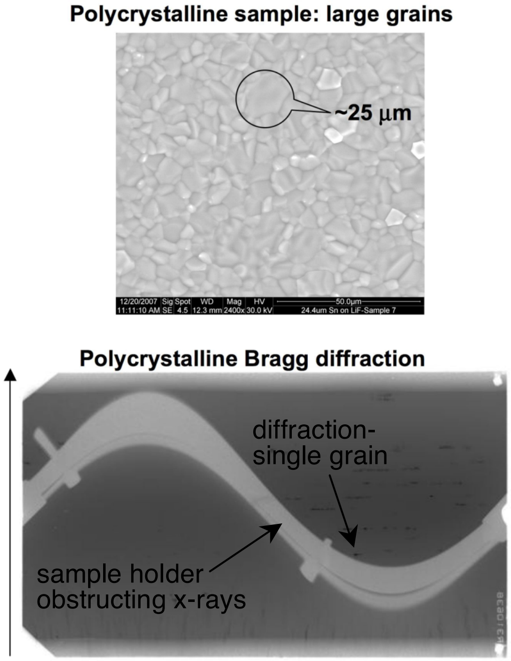
~25 μm
12/20/2007 Sig Spot WD Mag HV 50.0μm
11:11:10 AM SE 4.5 12.3 mm 2400x 30.0 kV 24.4um Sn on LiF-Sample 7
diffraction-
single grain
sample holder
obstructing x-rays
2θ

Figure 4.6. Polycrystalline x-ray diffraction from a tin target sputter coated on a LiF substrate, using 8 keV x-rays. The discontinuous diffraction pattern is attributed to the large grain size. Note that since the pattern was recorded in a cylindrical geometry where the target was placed on the cylinder axis, upon unfolding of the film the diffraction cones became straight lines.

Polycrystalline sample: <5 μm grains

Polycrystalline Bragg diffraction

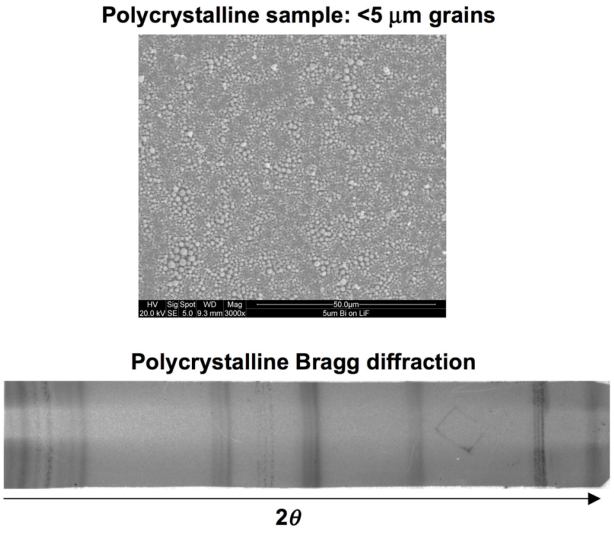
HV Sig Spot WD Mag 50.0μm
20.0 kV SE 5.0 9.3 mm 3000x 5um Bi on LiF
2θ

Figure 4.7. Bragg diffraction pattern from a polycrystalline Bi sample sputter coated on LiF substrate. A section of the diffraction rings is shown. Note that because of the small (< 5 μm) grain size the diffraction pattern appears to be continuous. 4.7 keV x-rays were used for this exposure.

In general, Bragg's law can be satisfied by varying λ or θ. The choice of variable is what distinguishes the various diffraction techniques. Furthermore, it is interesting to note the equivalency between Bragg's law and the reciprocal lattice vector $\vec{K}$ described in (4.6). From Figure 4.4 and Bragg's law

$$\left|\frac{\vec{s}-\vec{s}_0}{\lambda}\right| = \frac{2\sin\theta}{\lambda} = \frac{1}{d_{hkl}} = \left|\vec{K}\right|. \qquad (4.17)$$

The magnitude and angle of the incident and scattering vectors must be equal and their difference divided by the wavelength is equivalent to the magnitude of the reciprocal lattice vector.

Even though Bragg's law provides a fundamental understanding of the diffraction conditions, it does not describe the form of real 3D diffraction patterns since it is only expressed in scalar terms. A description of actual diffraction patterns is more intuitive using equations based on general scattering principles where the phase difference between different scattering centers (atoms in the lattice) is considered. For constructive interference to occur the Laue equations (in 3D) state that:

$$\begin{aligned}
\left(\vec{s}-\vec{s}_0\right)\bullet\vec{a}_1 &= h\lambda \\
\left(\vec{s}-\vec{s}_0\right)\bullet\vec{a}_2 &= k\lambda \\
\left(\vec{s}-\vec{s}_0\right)\bullet\vec{a}_3 &= l\lambda
\end{aligned} \qquad (4.18)$$

where $\vec{s}$ and $\vec{s}_0$ the scattered and incident x-ray unit vectors, $\vec{a}_i$ the lattice vectors and h, k, l are integers. Each of the above equations is satisfied by a series of cones with axes concentric to the row of scatterers.

4.2.2 X-RAY SCATTERING INTENSITY

There are several factors that influence the diffracted intensity which can be divided into two categories: material-related and diffraction geometry-related. In this section the effect of the atomic arrangement on the diffraction intensity is discussed. As it will be explained, satisfying the Bragg condition does not guarantee a diffracted signal. The atoms may be arranged in such a way within the unit cell of the material that the phase difference in the scattered beams may result in the sum of their amplitudes to cancel out. For this reason, the structure factor, a factor determining the amplitude of the scattered radiation from a unit cell must be calculated in order to predict the absence or presence of diffraction peaks and their corresponding intensity. Since the pertinent structures in this study are bcc, fcc and hcp the structure factors for these unit cells are calculated below.

In a unit cell having N atoms with fractional coordinates u, v, w, the structure factor for reflection from an (hkl) plane is given by [88]:

$$F_{hkl} = \sum_{1}^{N} f_n \exp\left[2\pi i(hu_n + kv_n + 1w_n)\right] \tag{4.19}$$

where f_n is the atomic scattering factor with the subscript n referring to different atomic species (e.g. in compounds). The structure factor is generally a complex number and its squared amplitude $|F_{hkl}|^2$ expresses the intensity of the scattered wave from a unit cell. An important remark about the structure factor is that it is independent of the unit cell size and shape, namely it depends only on the atomic positions in the chosen coordinate system. This is illustrated below in the calculation of the bcc, fcc and hcp structure factors.

Bcc structure factor: A body centered unit cell contains two atoms at the origin (0, 0, 0) and center of the cell $(\frac{1}{2}, \frac{1}{2}, \frac{1}{2})$. The structure factor becomes

$$F_{hkl} = f\left(1 + \exp[\pi i(h+k+l)]\right). \tag{4.20}$$

The (*hkl*) expected to result in no signal from a bcc unit cell are therefore combinations of *h, k, l* where $h+k+l = \text{odd}$. Examples of planes where diffraction signal is absent for a bcc structure are the (111), (113), (221) etc.

Fcc structure factor: The face centered cubic cell (Cu) is represented by four atoms at (0, 0, 0), $(\frac{1}{2}, \frac{1}{2}, 0)$, $(0, \frac{1}{2}, \frac{1}{2})$ and $(\frac{1}{2}, 0, \frac{1}{2})$ so that the corresponding structure factor is given by

$$F_{hkl} = f\left(1 + \exp[\pi i(h+k)] + \exp[\pi i(k+l) + \exp[\pi i(h+l)]]\right) \tag{4.21}$$

Cancellation of the structure factor for the fcc occurs when the *h, k, l* are mixed even and odd numbers such as the (112), (223), (100) etc.

Hcp structure factor: A unit cell that exemplifies the size and shape independence of the structure factor is that of the hexagonal close packed. The unit cell of an hcp structure consists of two atoms located at (0, 0, 0) and $(\frac{1}{3}, \frac{2}{3}, \frac{1}{2})$. Even though the lattice is not cubic as in the previous examples the structure factor can still calculated from (4.19). It is

$$F_{hkl} = f\left(1 + \exp[2\pi i(\frac{h}{3} + \frac{2k}{3} + \frac{l}{2})]\right) = f\left(1 + \exp[2\pi i(\frac{h+2k}{3} + \frac{l}{2})]\right) \qquad (4.22)$$

To have F_{hkl}=0, the term in the exponent $\frac{2(h+2k)}{3} + l$ must be equal to an odd number. This implies that $h + 2k = 3n$ where n is an integer and l must be an odd number.

Besides the structure factor, other material specific factors together with geometric terms can be combined in one equation [88] describing the diffracted intensity from a certain plane *hkl* and scattering angle θ

$$I_{diffraction} = |F_{hkl}|^2 \, p\left(\frac{1+\cos^2 2\theta}{\sin^2 2\theta \cos\theta}\right) A(\theta) e^{-2M} \qquad (4.23)$$

where F_{hkl} the material structure factor, p the multiplicity of the diffracting plane, $A(\theta)$ the absorption factor and e^{-2M} the temperature factor. The trigonometric term in brackets is referred to as the Lorentz-Polarization factor and it is geometry dependant. Multiplicity p refers to the number of permutations of (*hkl*) in position and ± sign that correspond to planes of the same interplanar distance d_{hkl} and F_{hkl}. For example the planes (100), (-100), (010), (0-10), (001) and (00-1) of a cubic structure all contribute to the same diffraction peak according to Bragg's law. Therefore, the multiplicity factor for the (100) family of planes is 6 for a cubic crystal.

The temperature factor otherwise known as the Debye-Waller factor is associated to the thermal vibrations of the atoms in the lattice. Because of the uncertainty in d_{hkl} introduced by thermal vibrations diffraction peaks appear to be broadened especially at elevated sample temperature resulting in a lower integrated diffraction peak intensity. The relation of the Debye-Waller factor to the material properties is shown in the expression for M [86] where

$$M = \frac{1.15\times 10^{4} T}{A\Theta^{2}}[\phi(x)+\frac{x}{4}]\left(\frac{\sin\theta}{\lambda}\right)^{2}. \tag{4.24}$$

In equation (4.24) T is temperature, A the atomic weight, Θ the Debye characteristic temperature of the substance in Kelvin, $\phi(x)$ a tabulated function where $x = \Theta/T$ (see Cullity), Θ the scattering angle and λ the wavelength. Using a sufficiently narrowband x-ray source the width of the diffraction peaks could be related to the specific heat at constant volume c_v and thermal expansion coefficient as a function of temperature.

The absorption mechanism of x-rays from a material is discussed in detail next. The geometry specific terms of the diffraction signal intensity will be presented in the instrument descriptions in Chapter 5.

4.2.3 X-RAY ABSORPTION

When x-ray radiation with intensity I_0 is incident on a material, two processes occur that decrease the transmitted intensity I. The first process involves the absorption of x-ray photons, whereas the second process causes scattering of the incident radiation from its direct path. "True absorption" is simply the interaction of x-ray photons with electrons in the material causing electronic transitions and thus, atom excitation. Upon decay to the ground state atoms emit fluorescent radiation which is isotropic (loss of directionality of the incident beam) and has different wavelength ($\lambda_{fluorescence}>\lambda_{incident}$) than the incident x-rays. In x-ray diffraction measurements, fluorescence contributes to the background noise and it is particularly detrimental in diffraction from high Z materials where a large number of possible excited states exist. An example of fluorescence was seen in the Laue diffraction pattern from Bi Figure 4.5. Fluorescence in this particular diffraction measurement was recorded as a white halo that significantly decreased the diffracted signal to noise.

Both "true absorption" and scattering are summed in a mass scattering coefficient μ_m such that the attenuated intensity of a monochromatic x-ray beam on a material of density ρ is given by

$$I = I_0 \exp[-\mu_m \rho x] \tag{4.25}$$

where x the thickness of the material. To understand the dependence of the mass absorption coefficient on the incident x-ray wavelength λ and material Z, the transmission from a large number of materials has been characterized using a broadband (white light) x-ray source. The dependence on λ and Z is given by the relation [88]

$$\mu_m = C\lambda^3 Z^3 \tag{4.26}$$

where C a constant. The plot below (Figure 4.8) illustrates the attenuation length namely the material thickness required for the incident x-ray intensity to decrease by 1/e. The materials chosen correspond to filters commonly used to attenuate the respective K_α x-ray radiation. In addition, the attenuation length from a low and a high Z material (Z_{Bi}=83 and Z_{Mg}=12) is compared on the same plot. Note that the attenuation curves exhibit a sawtooth pattern with peaks at the K, L, M etc. absorption edges, namely the energies where a K, L, or M electron is ejected respectively. Only the K-edge is relevant to our experiments since the K_α line emission was used in our x-ray diffraction measurements.

Another important remark is that for the purpose of blocking continuous background radiation while allowing the most from the characteristic K_α radiation to transmit, the filters and laser plasma source must use the same material. Because of the slightly longer wavelength of the emitted K_α radiation versus the absorption K-edge, filters of the same atomic species as the ions in the plasma source have the highest transmission in the K_α wavelength. Therefore, they are ideal attenuators for x-ray wavelengths other than that of the characteristic K_α line. The reason for this wavelength discrepancy is the fact that the absorbed photon energy is higher than the emitted K_α because of an energy conservation argument; the absorbed photon energy must equal the sum of the ejected K-shell electron kinetic energy plus the photon energy emitted upon decay of an L-shell electron to the K-shell.

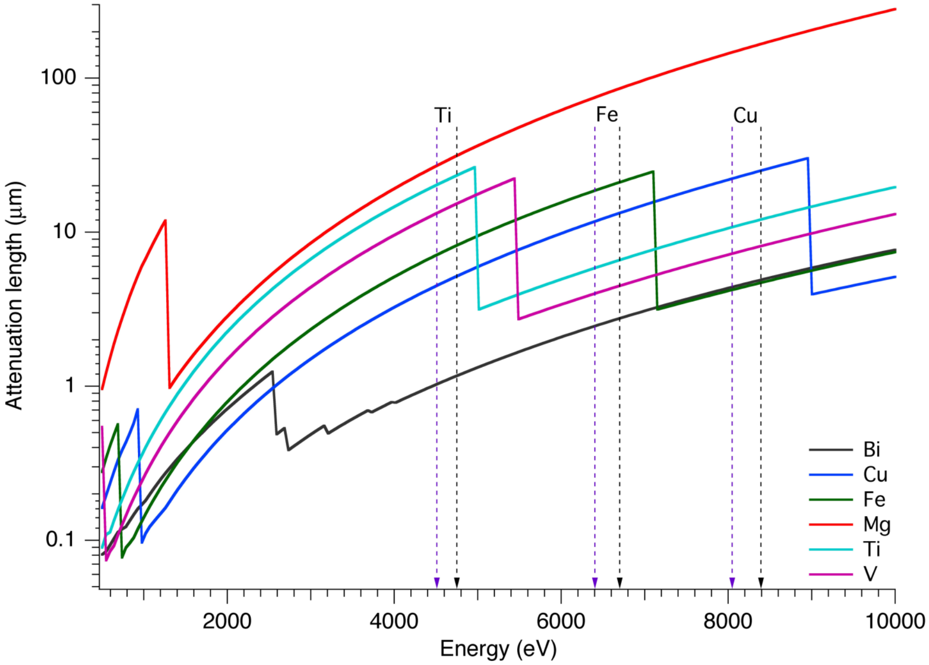

Figure 4.8. Plot of the attenuation length for target (Mg, Cu, Bi) and filter (Ti, V, Fe, Cu) materials used in this study. The vertical black and purple arrows show the energy of the He_α-like and K_α line emission respectively from Ti, Fe, and Cu. (Calculated using the Center for X-Ray Optics x-ray interaction with matter tools, http://www-cxro.lbl.gov/).

In Figure 4.8 the K_α energy of typical x-ray sources is also compared to the absorption energy as well as the He_α-like radiation, namely the K-shell transition in a He-like ion. The difference in energy between the two emission lines comes from the fact that for K_α emission only a single electron is knocked out of the atom, specifically from the K-shell. In He_α-like emission the atom has been stripped of all but two electrons before a K-shell electron ejection and subsequent decay takes place. In the first case the nucleus is screened more effectively by the electrons and therefore, the electronic binding energy is lower than in the He-like ion. The higher energy of the He_α-like emission implies an increase in the attenuation length. A comparison of the He_α-like, K_α and absorption edge wavelength can be found in the table below.

Table 4.3 Wavelength of the K_a, He_a-like emission, and K-edge for Ti, Fe and Cu.

	K_α (Å)	**He_α (Å)**	**K-edge (Å)**
Ti	2.749	2.605	2.497
Fe	1.936	1.851	1.743
Cu	1.541	1.478	1.381

4.3 Measuring the Dynamic Material Response with X-ray Diffraction

In Chapter 3, the properties of the shock wave profile were linked to the bulk material response. For example, shock wave splitting was attributed to elastic-plastic transitions and phase transformations occurring in the shock compressed material. However, information on the material response under shock compression using shock wave characterization methods is not only limited to a bulk material measurement but in some circumstances may be misleading. For instance, in small volume phase changes, no shock wave splitting may be evident which would infer no structural change. For this reason dynamic x-ray diffraction has become in recent years an extremely powerful tool in the studies of materials in extreme environments since it probes the physical processes happening in the evolving lattice at the relevant spatial and temporal scales. Combined with a macroscopic bulk measurement technique such as velocimetry a complete picture of the dynamic material behavior can be assembled. In this section, an interpretation of dynamic x-ray diffraction signal with respect to the lattice level phenomena is provided. Specifically, the diffraction signatures of the elastic (or uniaxial) and hydrostatic response of the lattice under shock compression are described. Material density is an important parameter than can be extracted from x-ray diffraction and used to obtain the material equation of state. The density values obtained via measurement of the interplanar spacing under uniaxial or hydrostatic compression is presented. Our treatment of density measurement is applicable to both single crystal and polycrystalline materials even though from a microscopic point of view the deformation mechanisms in the two structures are expected to be quite different.

4.3.1 UNIAXIAL LATTICE COMPRESSSION

Let us consider a crystalline solid (Figure 4.9). When a planar shock is applied, the lattice initially responds by compressing the planes whose unit normal is (partially) aligned to the shock direction. The lattice response is elastic as long as the applied stress does not exceed the Hugoniot Elastic Limit (HEL). However, above the HEL nucleation of defects can cause the lattice to relax plastically in all three directions or in other words to deform irreversibly as depicted in both the lattice and wave profile picture. In addition, depending upon the shock pressure in the Hugoniot end state and the material phase diagram a structural change may take place. Both plastic relaxation and phase nucleation and growth are time-dependent phenomena and therefore kinetic studies attempting to determine their time constants are extremely important in the formulation of constitutive models.

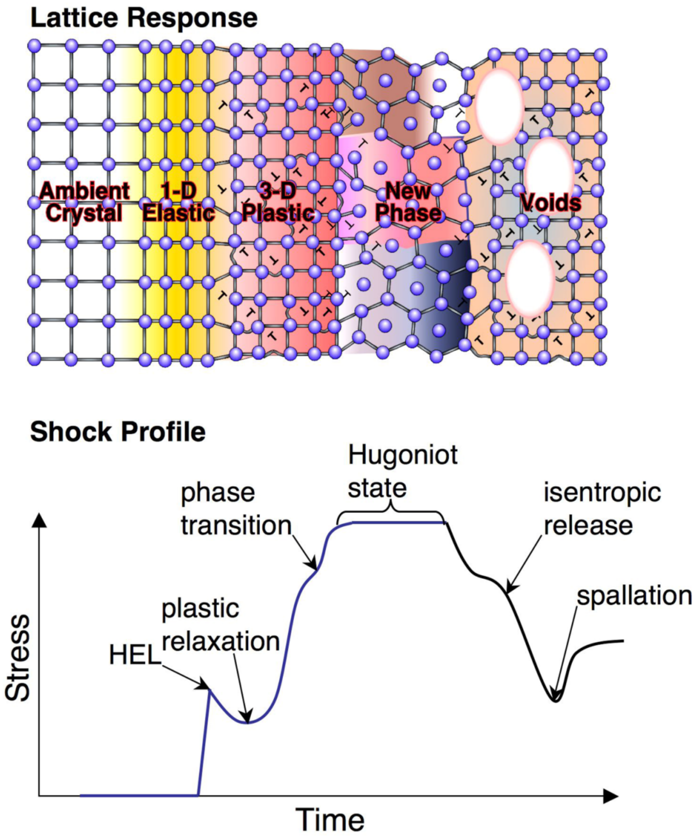
Lattice Response
Ambient Crystal
1-D Elastic
3-D Plastic
New Phase
Voids
Shock Profile
Hugoniot state
phase transition
isentropic release
plastic relaxation
HEL
spallation
Stress
Time

Figure 4.9. Illustration of a shocked crystalline material connecting the lattice processes to the observed bulk material behavior through measurement of the shock wave profile. The latter is typically obtained by velocimetry (VISAR) whereas lattice information can be extracted by x-ray diffraction.

Let us now consider the uniaxial lattice compression in the context of x-ray diffraction. First, from Bragg's law an expression for the change in the interplanar spacing or strain can be derived when the Bragg angle of the static and compressed diffraction peaks is known. This expression is

$$\frac{\Delta d_{hkl}}{d_{hkl}} = \frac{\frac{\lambda}{2}\left(\frac{1}{\sin\theta} - \frac{1}{\sin(\theta+\Delta\theta)}\right)}{\frac{\lambda}{2}\frac{1}{\sin\theta}} = 1 - \frac{\sin\theta}{\sin(\theta+\Delta\theta)}\,. \tag{4.27}$$

Under uniaxial compression the lattice deforms (reversibly) in the direction of the applied shock (Figure 4.10). Since a volume element is given by

$$V = Ax \tag{4.28}$$

where A a unit area and x the height of the volume element, the ratio of the compressed/static volume and hence the density ratio of the static/compressed lattice becomes

$$\frac{V}{V_0} = \frac{x}{x_0} \Rightarrow \frac{\rho_0}{\rho} = \frac{x}{x_0}. \tag{4.29}$$

For a plane (hkl) whose unit normal vector $\hat{n}$ is oriented parallel to the shock direction the density ratio is simply given by the interplanar spacing ratio

$$\frac{\rho}{\rho_0} = \frac{d_{hkl}}{d'_{hkl}} = \frac{\sin(\theta + \Delta\theta)}{\sin\theta}. \tag{4.30}$$

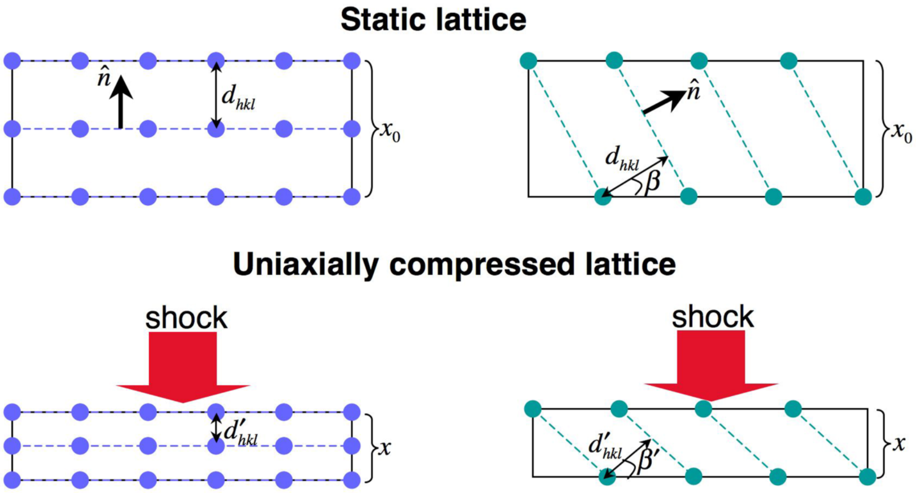

Figure 4.10. Uniaxial lattice compression along the direction of the shock is shown for a plane with normal parallel to the shock direction and a plane with normal at an angle of 90°-β to the shock direction. In the first case only the interplanar spacing decreases upon compression. In the second case both the interplanar spacing and the angle of the plane normal changes.

For planes that are oriented at an angle of $90° - \beta$ with respect to the shock, the density ratio cannot be expressed directly by the static and compressed interplanar spacing ratio. From equation (4.29) and Figure 4.10 for theses planes

$$\frac{\rho}{\rho_0} = \frac{x_0}{x} = \frac{d_{hkl} / \sin(90° - \beta)}{d'_{hkl} / \sin(90° - \beta')} \Rightarrow \frac{\rho}{\rho_0} = \frac{d_{hkl} / \sin\beta}{d'_{hkl} / \sin\beta'} = \frac{\sin(\theta + \Delta\theta)}{\sin\theta} \frac{\sin\beta}{\sin\beta'}. \qquad (4.31)$$

(Note that $\Delta\theta$ and θ in 4.31 and 4.30 are not the same. They represent the respective angular shift and static Bragg angle from the (*hkl*) plane described in each example.) From equations (4.30) and (4.31) the density ratio measured from the planes that are normal and at an angle relative to the shock direction must be the same. In addition the angles $\Delta\theta$ and θ in (4.31) can be determined via diffraction and β is known from the crystallographic orientation of the target. Thus β' can be calculated resulting in a measurement of the shear strain, namely the deformation of the lattice in the direction parallel to the plane surface.

4.3.2 HYDROSTATIC LATTICE COMPRESSSION

Having discussed how x-ray diffraction can provide a strain value for lattice that is compressed elastically in the direction of the shock, we will examine the other extreme of the material response; a lattice compressing hydrostatically. This behavior is induced in a material by applying a stress that greatly exceeds the HEL. In this case a measurement of density with x-ray diffraction should coincide with the hydrostatic (P-ρ) Hugoniot. Furthermore, an absolute equation of state for hydrostatically compressed materials can be experimentally constructed by measuring density and particle velocity simultaneously using x-ray diffraction and Doppler velocimetry (VISAR) respectively.

A schematic of a hydrostatically compressed lattice is shown in Figure 4.11. Since the lattice compresses isotropically by factor α in every direction, the compressed lattice volume becomes

$$V = xyz = \alpha^3 x_0 y_0 z_0 \Rightarrow \frac{V}{V_0} = \alpha^3 . \qquad (4.32)$$

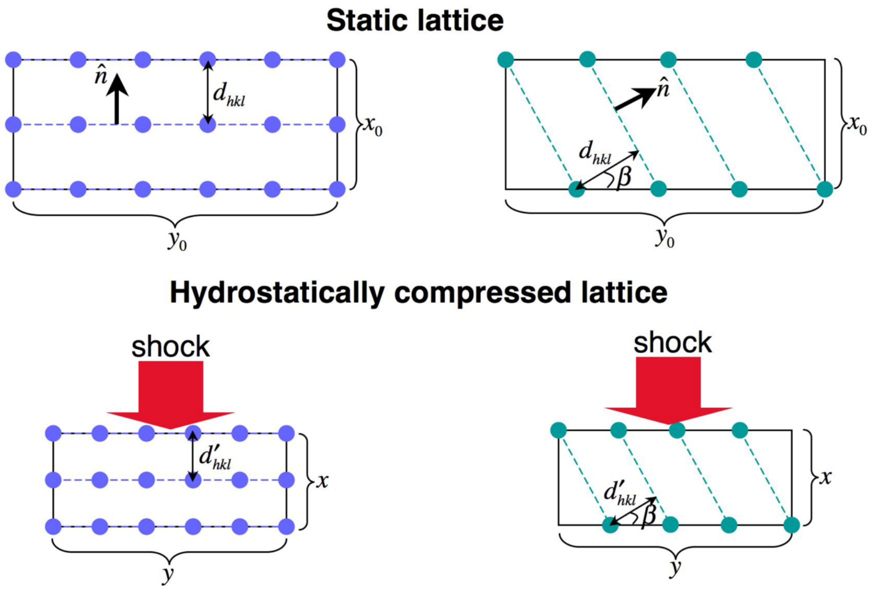

Figure 4.11. Hydrostatic lattice compression in a shocked crystalline material. When the applied stress greatly exceeds the shear strength in the material, the lattice compresses hydrostatically despite the fact that the shock is applied in one direction only. Since the aspect ratio of the lattice remains the same under hydrostatic compression, a plane with normal at an angle of 90°-β to the shock direction does not change orientation as in the case of uniaxial compression.

The interplanar spacing d_{hkl} is also expected to contract by the same factor α hence

$$\frac{d'_{hkl}}{d_{hkl}} = \left(\frac{V}{V_0}\right)^{1/3} = \left(\frac{\rho_0}{\rho}\right)^{1/3}. \qquad (4.33)$$

The hydrostatically compressed material density ratio is therefore given by the diffraction angle θ and the angular shift $\Delta\theta$ from the static diffraction peak by

$$\frac{\rho}{\rho_0} = \left(\frac{d_{hkl}}{d'_{hkl}}\right)^3 = \left(\frac{\sin(\theta+\Delta\theta)}{\sin\theta}\right)^3. \qquad (4.34)$$

Since the lattice aspect ratio is maintained during isotropic compression, planes whose normal is at an angle with respect to the shock direction do not rotate as in the case of uniaxial compression. For this reason, equation (4.34) is also valid for these types of planes. However, a discrepancy in the strain measured for different (*hkl*) above the HEL may indicate strength so it is always necessary to compute strains from all diffraction planes where static and compressed diffraction signal has been captured. In addition, an understanding of the error bars in the measurement of the diffraction peak position is also important in order to be able to distinguish a physical effect such as strength from a systematic error.

4.3.3 PHASE TRANSITIONS

In our study of shock-induced phase transitions, an understanding of both solid-solid (Mg) and solid-liquid transitions (Mg, Bi) was pursued. These types of transitions have been previously determined for the majority of known substances via static x-ray diffraction techniques. Only recently developments in dynamic loading techniques and x-ray sources (mainly based on high power lasers) have excited an interest in the understanding of the dynamics and kinetics of transient phase transitions with timescales ranging from tens of nanoseconds to femtoseconds. The α to ε (hcp to bcc) transition in Fe has been the leading material in dynamic x-ray diffraction studies due to its broad technological and scientific importance. In general, probing solid-solid transitions under shock-loading has enabled an understanding of the lattice mechanisms and kinetics of these processes that was previously unknown.

Specifically using x-ray diffraction and single crystals oriented along different crystallographic planes it is possible to isolate the most probable mechanism(s) of a solid-

solid transformation. However, single crystals samples are quite costly and in certain cases very difficult to prepare (cut and polish) at a specified orientation and thickness. Polycrystalline samples can therefore be used instead. In this case, even though the structure of new phase can be identified it is almost impossible to identify the atomic re-arrangement process leading to the phase. For custom-manufactured samples there may be a way to prepare polycrystalline samples of a specific texture (grain size and orientation) such that changes in the sample texture upon compression may help constrain the phase transition pathway. However, the risk in this technique is that, because of the original strong texture the new phase may not be observed at all. Furthermore, for both single crystal and polycrystalline materials, kinetics play an important role in whether the phase transition will be captured within the duration of the x-ray pulse. Having the shock as a temporal fiducial it is relatively simple to obtain the timescale of a phase transition in the bulk of the material using a nanosecond x-ray source such as this generated in our experiments. If both single crystal and polycrystalline forms of the material of interest are available it is also very interesting to explore discrepancies in the kinetics of the phase transformation which would be attributed to the different phase nucleation and growth mechanisms in either material form.

The solid-liquid phase transformation deserves a special attention since it has been the most challenging problem so far in dynamically induced phase transformations. Even though there exists literature on non-thermal melt (ablation-induced, fs timescale) solid-liquid transformations under shock conditions have never been observed. The main challenge has been the low intensity of the diffraction peaks originating from the amorphous phase. In addition, for the shock pressure required to achieve melt in most of the substances, a high amplitude noise background is always superimposed on the diffraction signal. In the paragraph that follows, I will aim to explain the nature of the signal expected from an amorphous substance, specifically a liquid. This discussion will be useful later in association to the instrumentation design for detecting diffraction signal from liquids.

As explained earlier the main factor contributing to the diffracted intensity is the square of the structure factor F^2. Re-writing equation (4.19) in terms of the reciprocal lattice vector $\vec{K}$ and the atomic positions in a lattice $\vec{x}_n$, we can express the diffracted intensity $I(\vec{K})$ as

$$\begin{aligned}
I(\vec{K}) &= F(\vec{K})F^*(\vec{K}) \\
&= \sum_1^N f_n \exp[-2\pi i\vec{K}\cdot\vec{x}_n] \times \sum_1^N f_{n'} \exp[2\pi i\vec{K}\cdot\vec{x}_{n'}] \\
&= \sum_1^N \sum_1^N f_n f_{n'} \exp[-2\pi i\vec{K}\cdot(\vec{x}_n - \vec{x}_{n'})] \qquad (4.35) \\
&= \sum_1^N \sum_1^N f_n f_{n'} \exp[-2\pi i\vec{K}\cdot\vec{x}_{nn'}] \\
&= \sum_1^N \sum_1^N f_n f_{n'} \cos(2\pi\vec{K}\cdot\vec{x}_{nn'})
\end{aligned}$$

where only the real part is considered. For x-ray diffraction from an isotropic body, such as a liquid, an average intensity is observed since the scattering probability is the same in all directions. Experimentally this is manifested for a given diffraction angle as a ring whose intensity can be determined from equation (4.35) by taking the average of the cosine term. This results in the Debye formula for intensity (also applicable to perfect powders)

$$\overline{I(\vec{K})} = \sum_{1}^{N}\sum_{1}^{N} f_n f_{n'} \frac{\sin(2\pi K x_{nn'})}{2\pi K x_{nn'}} \tag{4.36}$$

where $x_{nn'}$ the distance in a pair of atoms [90]. It can be shown numerically that the average intensity maxima are at

$$K_{\max} x_{\max} = 1.23 \Rightarrow x_{\max} = 1.23 \cdot \frac{\lambda}{2\sin\theta_{\max}} \tag{4.37}$$

where the conversion to scattering angle comes from the equivalence of the reciprocal lattice vector $\vec{K}$ to the Bragg diffraction formulation. The diffraction pattern takes the form shown below (Figure 4.12). Therefore, a measurement of such pattern in a solid-liquid transformation induced by shock-loading would yield the average spacing of the atoms in the liquid and thus a density value, which could subsequently become an input to the material EOS. (On the other hand, experiments where the liquid state would be inferred by a decrease in the intensity and eventually the disappearance of diffraction lines would unable to provide essential EOS data.)

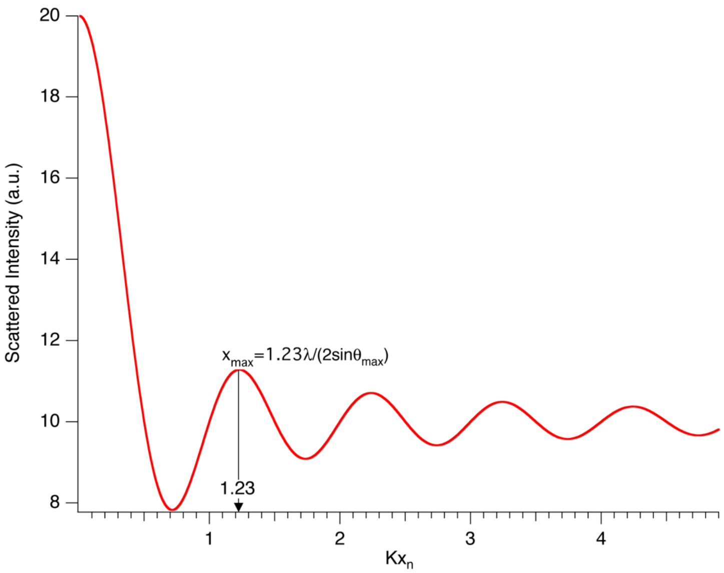

Figure 4.12. Plot of the scattered intensity from an amorphous (isotropic) body.

4.4 X-ray Emission from a Thermal Plasma

Multi-beam kJ level laser facilities such as OMEGA and the National Ignition Facility (NIF) offer the unique capability of probing materials under extreme temperature and pressure conditions [91, 92] with intense x-ray backlighter sources at a broad range of energies. Such capability is critical in understanding for example the symmetry in inertial confinement fusion capsules and in revealing exotic lattice structures for materials approaching TPa conditions. As a precursor to these type of experiments, a significant amount of work has already been dedicated in characterizing laser plasma sources, specifically correlating laser parameters to x-ray conversion efficiency and duration [93]. To date the most detailed characterization of thermal plasma x-ray sources can be found in Phillion's paper [94].

In general, line emission is produced by focusing a laser pulse onto a metal target. For the laser parameters used in our experiments (100-300 J, 1-4 ns, ~200 μm spot diameter) the plasma formed by the laser coupling mechanisms discussed in Chapter 2 consists of highly ionized atoms resulting from electron-ion collisions. Specifically He-α line emission (1s2p-1s^2) occurs when an electron recombines with an ion in a hydrogen-like state. In order to understand the temporal properties of this K-shell line emission the rates of collisional ionization and three-body recombination must be considered.

Assuming that the maximum electron density at which x-ray line generation occurs is the critical density n_e, Seaton's near-threshold collisional ionization cross section yields a timescale

$$\frac{1}{\tau_c} = \frac{256\sqrt{\pi}}{9n}\bar{g}a_0^2\alpha c n_e \left[\frac{E_H}{I}\right]^{3/2} \times \begin{array}{c} \left[\frac{kT}{I}\right]^{1/2} \exp\left[\frac{-I}{kT}\right] \text{ for } kT << I \\ \left[\frac{kT}{I}\right]^{-1/2} \text{ for } kT >> I \end{array} \qquad (4.38)$$

where n = Rydberg shell number
a_0 = Bohr radius = 0.529 Angstroms
$E_H =$ Hydrogen ionization energy = 13.6 eV
c = speed of light = 3x10$^8 m/s$
$\alpha =$ fine structure constant = 1/137
$\bar{g} =$ Gaunt factor of photoionization~0.42.

In between the above two extremes, the factor on the right hand side of equation (4.38) has a maximum value of 0.2541 at kT=3.75I. It can be shown that for He-α lines τ_c is of the order of several hundred ps, so in order to generate such line emission the laser pulse must be also at least several hundred ps.

X-ray emission results from recombination into a Rydberg shell of an electron followed by radiative decay to the ground state. The three-body recombination rate is relevant for this process and it is given by (assuming spontaneous radiative decay)

$$\frac{1}{\tau_{3R}}\ (ps^{-1}) = 0.07\left[\frac{1keV}{T}\right]\left[\frac{n_e}{10^{22}cm^{-3}}\right]\overline{Z} \tag{4.39}$$

where $\overline{Z}$ the effective ionic charge. Based on the above rates it is possible that line emission persists even after the laser pulse has switched off because of highly stripped ions that take longer to recombine. An interesting study showing a comparison between the duration of the laser pulse and x-ray plasma source (K-shell line emission) was conducted by Burnett et al. [95]. Furthermore, Phillion's experiments demonstrated the energy dependence of the x-ray conversion efficiency; intensities that were greater by an order of magnitude but having lower pulse length and energy produced an x-ray flux that was almost 4 times smaller than a laser source with greater energy and pulse duration but lower intensity by one order of magnitude. For our experiments the laser parameters of He-a sources from laser plasmas formed by Ti, Fe and Cu were optimized. The table below shows the laser parameters utilized.

Table 4.4 Laser energy, pulsewidth, and focal spot size for He-α x-ray backlighting.

	E **(J)**	**t_{pulse}(ns)**	***D*** **(μm)**
Ti	300	3	250
Fe	240	3	150
Cu	300	3	100

5 DESCRIPTION OF EXPERIMENTAL TECHNIQUE AND DIAGNOSTICS

Having presented a brief background on the shock physics, dynamic material response, and x-ray diffraction, we now proceed into a detailed description of the experimental approach used to understand the phenomena induced by dynamic loading. The techniques for laser-based shock and dynamic x-ray diffraction (DXRD) experiments conducted at the JANUS laser facility are presented. More specifically, the x-ray diffraction instrumentation developed during our studies, the velocimetry diagnostic for measurement of the transient material response, as well as the imaging diagnostics employed for reliable shock and x-ray drive beam alignment are described.

5.1 General Description of Experimental Setup

Experiments were performed at the two-beam kJ-level JANUS laser facility utilizing each of the laser arms for x-ray backlighting and shock drive. A schematic of the JANUS target chamber and laser beam geometry is shown (Figure 5.1). The EAST JANUS beam was routinely employed towards x-ray backlighting, whereas the WEST JANUS beam towards shock generation. Since the target and x-ray source positioning in the diffraction geometries demanded that the laser beam foci were separated by several centimeters (and off-target chamber center (TCC)) the motorized final lenses of the JANUS arms were translated and/or tilted to accommodate our instrumentation.

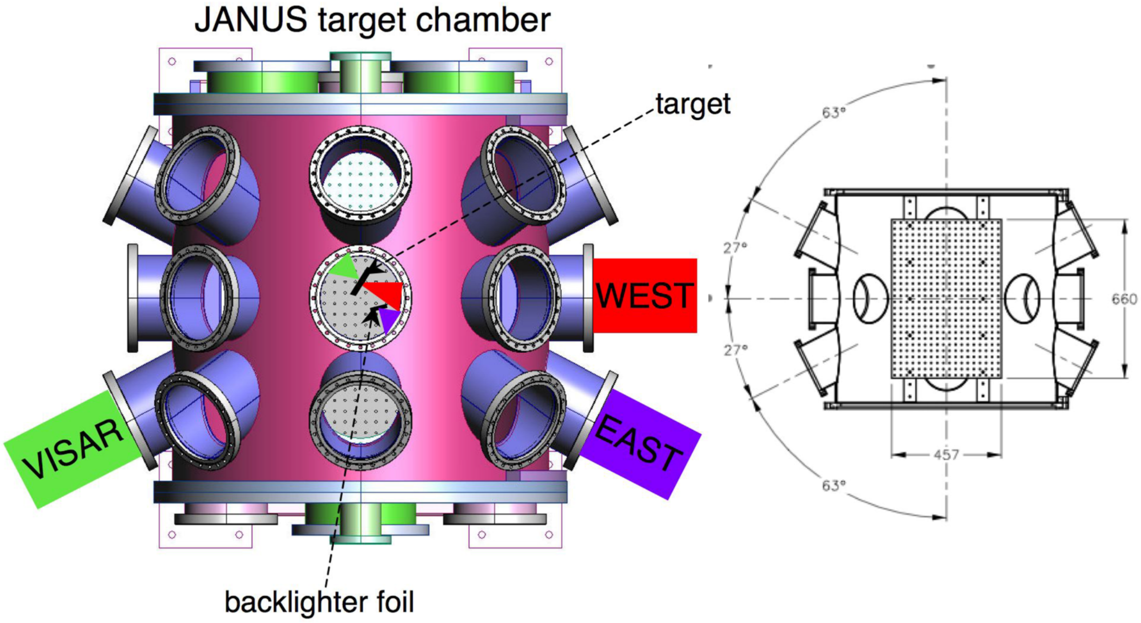

Figure 5.1. Top view of the JANUS target chamber. The input ports for the VISAR, EAST, and WEST beams are shown together with the in-chamber target/beam geometry. Port angles and chamber baseboard dimensions are also included.

The diagnostic configuration for the two types of polycrystalline x-ray diffraction cameras is illustrated below (Figure 5.2, Figure 5.3). Note that an imaging system enabled us to align the x-ray drive beam within ~100 μm from the center of the backlighter foil defined by a Cu washer having a 600 μm aperture. Furthermore, to overlap within ~100 μm precision the x-ray backlighter spot, the shock drive spot, and VISAR probe, an equivalent plane imaging diagnostic was implemented and will be described later in this chapter. We now present each of the experiment components in more detail.

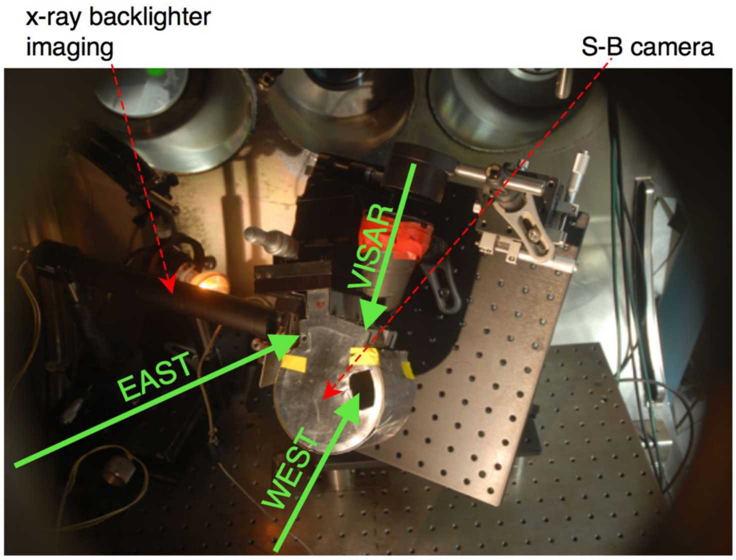
x-ray backlighter imaging
S-B camera
VISAR
EAST
WEST

Figure 5.2. View of the JANUS target chamber with the Seeman-Bohlin (S-B) camera, VISAR, and x-ray backlighter imaging system in preparation for a data shot. The S-B camera was shielded from background noise with a layer of Pb tape.

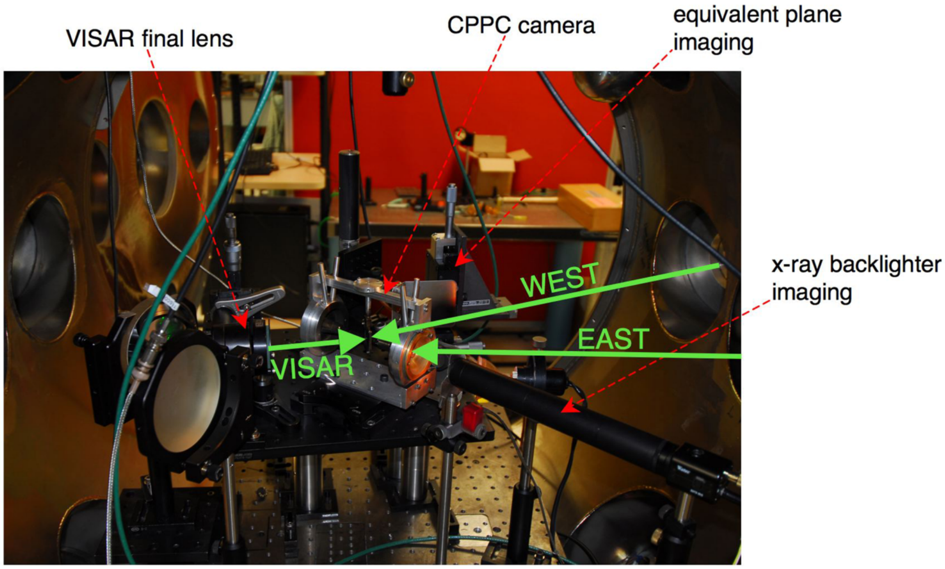
VISAR final lens
CPPC camera
equivalent plane imaging
WEST
EAST
VISAR
x-ray backlighter imaging

Figure 5.3. Photograph of the JANUS target chamber in preparation for dynamic x-ray diffraction experiments with the Cylindrical Pinhole Powder Camera (CPPC).

5.2 The Janus Laser System

Our experiments were performed at the JANUS laser facility at LLNL. The two-beam laser system delivering approximately <350 J in 2ω (527 nm) per arm, in a single 0.2-22 ns pulse, has been the test-bed for x-ray backlighting of dynamically loaded materials for several years. The architecture of the laser system and its specifications are outlined below (Figure 5.4).

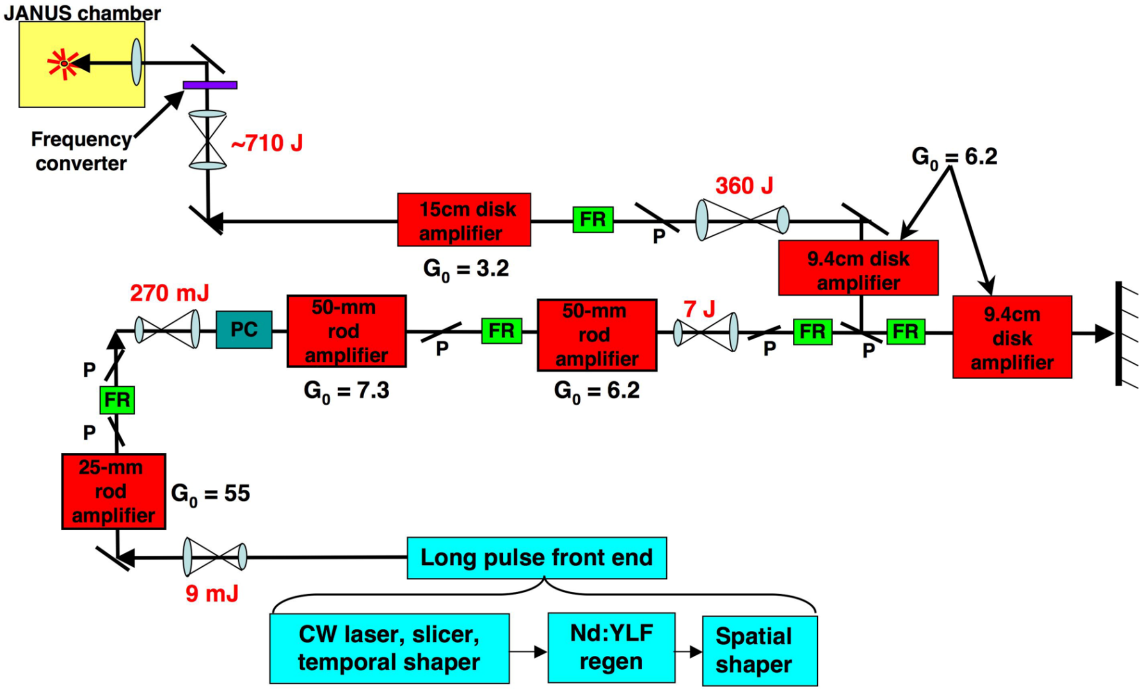
JANUS chamber
Frequency converter
~710 J
15cm disk amplifier
$G_0 = 3.2$
FR
P
360 J
$G_0 = 6.2$
9.4cm disk amplifier
270 mJ
PC
50-mm rod amplifier
$G_0 = 7.3$
P
FR
50-mm rod amplifier
$G_0 = 6.2$
7 J
P
FR
P
FR
9.4cm disk amplifier
P
FR
P
25-mm rod amplifier
$G_0 = 55$
9 mJ
Long pulse front end
CW laser, slicer, temporal shaper
Nd:YLF regen
Spatial shaper

Figure 5.4. Diagram showing the optical design and performance for one of the JANUS long-pulse beams (courtesy of D. Price).

The laser system front end consists of a single longitudinal mode solid-state continuous wavelength (CW) laser at 1053 nm with a linewidth of $<10^{-5}$ nm. The CW output is chopped by a Pockels cell into a 10 Hz pulse train with individual pulses of 100 ns pulsewidth and then injected into a polarized single mode fiber. A Mach-Zehnder optical fiber modulator is employed at this stage to define the desired temporal pulse shape. There are 96 waveform points or "glitches" spaced at 250 ps from each other and with a temporal width of ~300 ps that define the pulse-shape by control of their individual amplitude.

After pulse-shaping the resulting pulse train of ~1 nJ per pulse in energy is injected into a regenerative amplifier (oscillator) with a TEM00 center cavity mode waist and an Nd:YLF gain medium. The typical extracted pulse energy is 9 mJ. After the regenerative amplifier, the initial Gaussian spatial profile of the laser pulse is converted to a top hat profile by passing through a spatial shaping diffractive element. By relay imaging this top hat profile to a 9 mm aperture serrated edge apodizer, a supergaussian waveform is generated and propagated into the laser chain.

To generate the kJ-level (in 1ω) energy output in a single pulse, the beam emerging from the JANUS front-end is fed into a flash-lamp pumped amplifier chain consisting of six Nd-doped phosphate glass amplifiers (three rod and three disk amplifiers) whose details can be found in Figure 5.4. The beam is spatially filtered and relay-imaged by a series of vacuum spatial filters along the amplifier chain. Placement of a Faraday rotator (with a polarizer on the input and output) after each amplifier protects from feedback. A 50 mm Pockels cell is also positioned in the amplification chain to reduce any amplified spontaneous emission. All amplifiers are single-passed except for the first 9.4 cm disk amplifier, which is double-passed. A pulsed Faraday rotator inserted before this amplifier rotates the polarization of the output pulse by 90° such that the output pulse from the disk amplifier is reflected by the polarizer into the rest of the amplifier chain. At the end of the amplifier chain a ~710 J pulse is frequency doubled in a 15 mm Type 2 KDP crystal. The 527 nm pulse is then delivered into the target chamber and is focused at TCC by a 1010 mm focal length lens.

When experiments necessitated a very smooth spatial profile, phase plates were inserted before the final lens. The imaged drive spot using a 1 mm phase plate vs. a drive spot without a phase plate is shown below (Figure 5.5). In general, we preferred adjusting our experimental parameters to accommodate the phase plates available at the facility in order to achieve spatially uniform pressure drives. Otherwise hot spots in the focused beam caused great spatial variations in pressure, which were typically diagnosed in the velocimetry record as variations in the shock breakout time and fringe jump value along the spatial direction (more details on velocimetry are given in section 5.4).

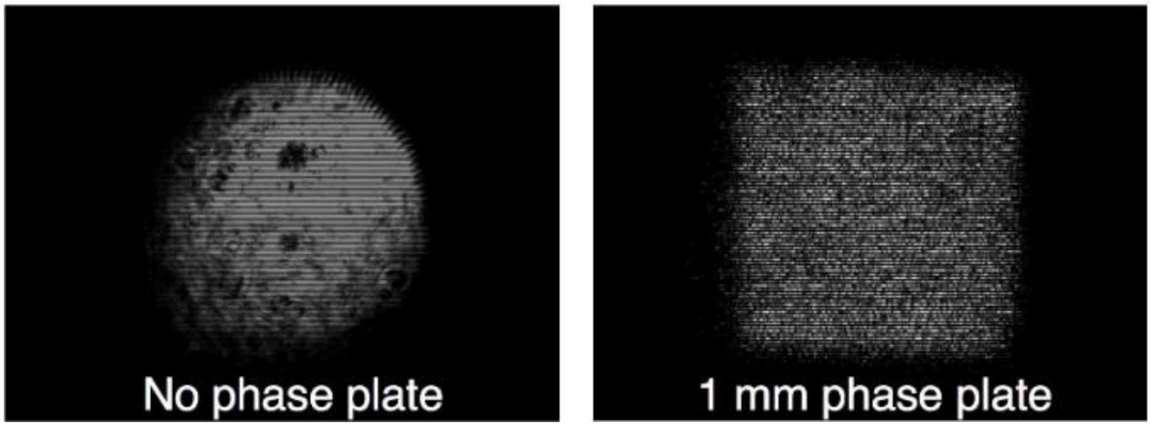

Figure 5.5. JANUS beam profile used for the shock drive without and with a 1 mm phase plate.

In addition, the pulse-shaping capability of JANUS that was described earlier was extremely important for generating a variety of loading conditions ranging from shocks to ramped waveforms of tens of nanoseconds. However, we encountered a change in the output energy as a function of pulse length, which is summarized in the series of shots plotted in Figure 5.6.

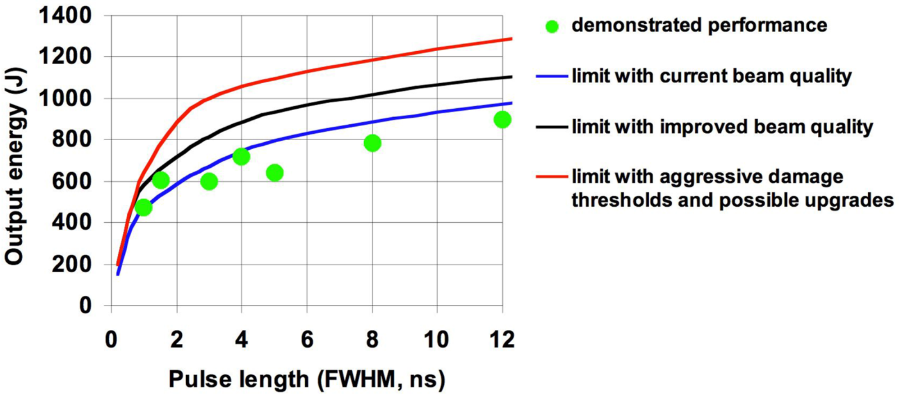

Figure 5.6. Plot of the JANUS laser output energy as a function of pulse length (courtesy of D. Price).

5.3 X-Ray Diffraction Diagnostics

During these studies x-ray diffraction diagnostics were developed in order to understand the lattice response of both single crystal and polycrystalline materials under nanosecond shock-loading. Specifically we designed and implemented diffraction cameras that accommodated laser driven x-ray sources from the K-shell emission of the thermal plasma generated, as well as laser driven shocks. The end goal was to apply this instrumentation to measure shock-induced phase transformations, specifically solid-solid and solid-melt, as well as strength effects in the compressed solids by capturing lattice-level information on a single shot basis. In this section, the two geometries relevant to the experimental results will be discussed. As the author led the development of the focusing-type x-ray geometry, a more detailed characterization of this instrument will be presented.

5.3.1 THE SEEMAN-BOHLIN FOCUSING DIFFRACTION GEOMETRY

The Seeman-Bohlin (S-B) camera [96] is a polycrystalline diffraction geometry that offers improved angular resolution and signal amplitude compared to Debye-Scherrer type cameras by exploiting a geometric focusing effect. Focusing of the diffracted x-rays onto the detector occurs when a point x-ray source, sample, and detector are arranged around a circle. The sample can subtend a large solid angle relative to the x-ray source such that a larger fraction of x-rays emanating from the point source can be used for probing the sample compared to collimated x-ray geometries. In addition, the angular resolution is limited mainly by the spectral bandwidth of the x-ray source, similar to single crystal dynamic x-ray diffraction measurements.

The S-B camera described here is ideally suited for laser based *in situ* dynamic x-ray diffraction experiments, where a tightly focused high energy (>100 J) laser beam onto a metal foil is used to generate the point source of K-shell x-rays. This bright x-ray point source together with a high dynamic range imaging plate detector permits a sample size small enough such that ablatively driven shocks with peak pressure >100 GPa can be produced. Thus, while static diffraction patterns from powder samples have been previously acquired in a S-B geometry [97], we now demonstrate its capability in shocked polycrystalline diffraction performed on a laser platform suitable for both shock and x-ray production.

Seeman-Bohlin camera description

We designed a S-B diffraction camera to serve as a lattice diagnostic in polycrystalline material shock studies. Focusing of the diffracted-x-rays occurred by positioning the point x-ray source, polycrystalline sample, and imaging plate detector [98] (Fujifilm BAS-MS2040) around a circle of diameter D=100 mm (Figure 5.7). On a circle, equal angles are subtended by arcs of equal lengths. Therefore, all x-rays originating from a point S on the camera circle that diffract from a given (*hkl*) plane at an angle specified by the Bragg condition $2d_{hkl}\sin\theta_{hkl} = \lambda$ re-intersect the circle at a single point O.

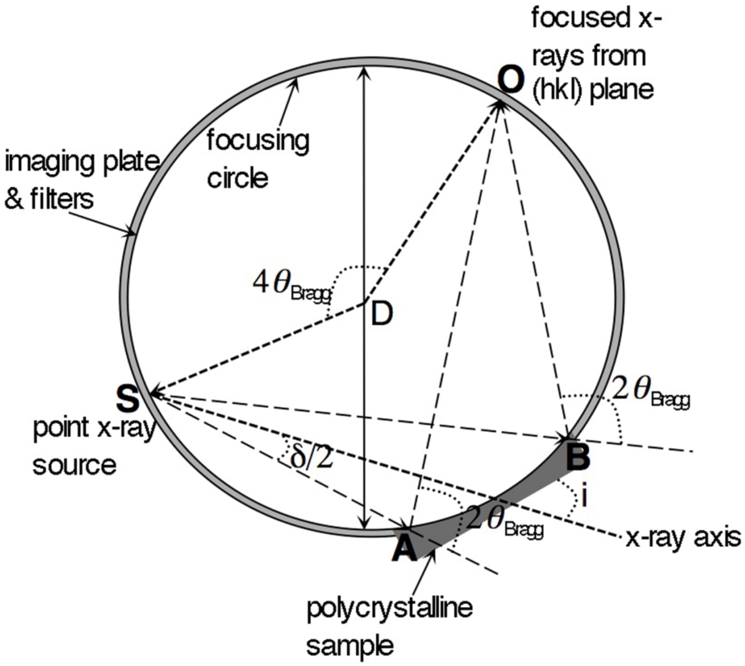
focused x-rays from (hkl) plane
O
focusing circle
imaging plate & filters
$4\theta_{\mathrm{Bragg}}$
D
S
point x-ray source
$2\theta_{\mathrm{Bragg}}$
B
$\delta/2$
i
$2\theta_{\mathrm{Bragg}}$
x-ray axis
A
polycrystalline sample

Figure 5.7. The Seeman-Bohlin focusing geometry. Aligning the point source, sample, and detector along the perimeter of a circle causes all x-rays diffracting at the same θ_{Bragg} from points A, B on the sample to focus at point O on the circle. In the camera presented here x-rays with angular spread δ=8.2° impinge upon the sample. The sample is positioned around a focusing circle of diameter D=100 mm, at an angle i=20.5° with respect to the x-ray axis. An imaging plate wrapped around the focusing circle above the sample and x-ray source captures diffraction cones of 2θ=28°-167°.

Figure 5.8 shows that the 2P level splitting in Fe He_a-like emission (1.8505 Å and 1.8595 Å) upon diffraction from the Cu (311) and (222) planes can be resolved. This example demonstrates that due to the focusing effect the instrument geometry possesses angular resolution of better than ~1° in 2θ, where $\Delta 2\theta = 2(\sin^{-1}(\frac{\lambda_1}{2d_{hkl}}) - \sin^{-1}(\frac{\lambda_2}{2d_{hkl}}))$, limited only by the laser based x-ray backlighter spectrum.

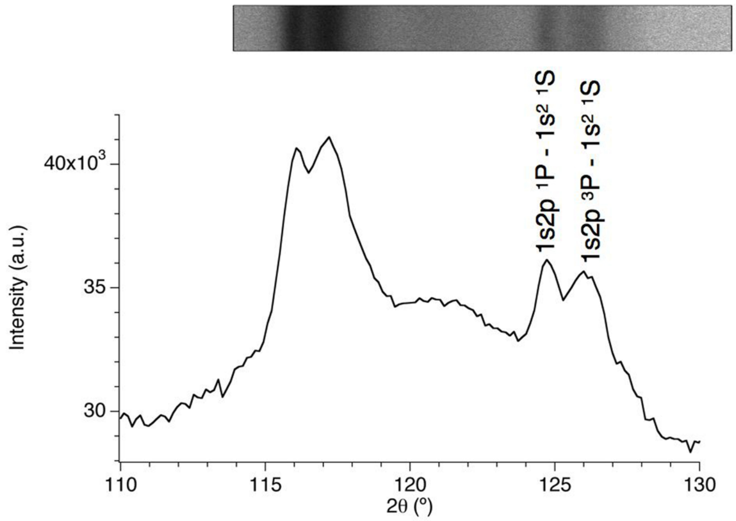

Figure 5.8. Demonstration of the instrument's angular resolution by detecting the 2P splitting in the He$_\alpha$-like emission of Fe. The wavelength difference between the resonance and intercombination lines, $\Delta\lambda$=0.009 Å, corresponds to $\Delta 2\theta$~1°.

Flat, polycrystalline foil samples (~65 mm^2) were positioned 34 mm away from the point x-ray source with their front surface tangent to the focusing circle and at an angle i=20.5° with respect to the x-ray axis (Figure 5.9). This allowed a 2θ detection range between 28° and 167° on the imaging plate, whose alignment around the focusing circle was repeatable to within 500 μm using reference pins. Ideally, the sample curvature is required to match that of the circle for optimal focusing; however, since the sample length was small compared to the diameter of the S-B camera, focusing was limited predominantly by the spectral bandwidth of the x-ray source rather than the mismatch in the sample-circle curvature.

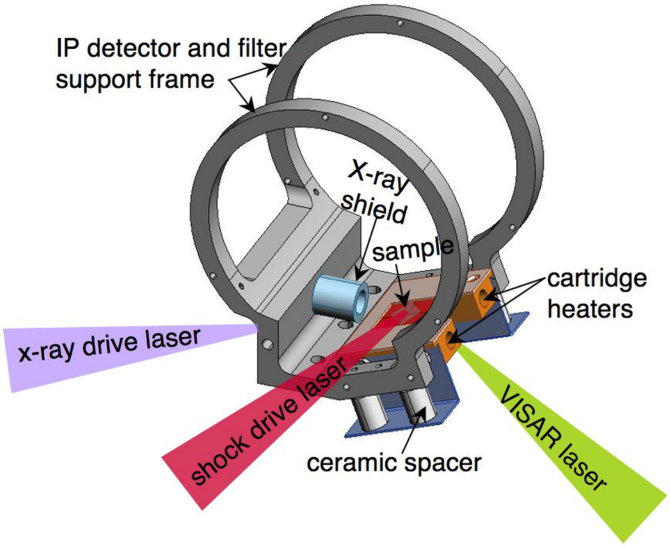
IP detector and filter support frame
X-ray shield
sample
cartridge heaters
x-ray drive laser
shock drive laser
ceramic spacer
VISAR laser

Figure 5.9. The Seeman-Bohlin camera adapted for laser driven shock-compression and x-ray generation. A point source of K-shell x-rays is produced at the focus of a high energy laser beam incident on a metal foil. Shocks are formed via laser ablation on the sample's front surface. Samples can be pre-heated to different initial temperatures <600K. Measurement of the sample's rear surface velocity is obtained by a line-imaging VISAR.

A point x-ray source was generated by focusing one of the high-energy laser beams of JANUS on a metal foil. The laser focal spot was aligned with an uncertainty of <100 μm to the center of a 600 μm diameter aperture placed on the focusing circle. The x-rays emitted from the thermal plasma were confined to a solid angle of δ=8.2° by a stainless steel tube containing a 1 mm diameter pinhole. This shielding construction prevented exposure of the imaging plate from direct line of sight x-rays. It also resulted in a 5 mm by 15 mm elliptically-illuminated region on the sample (Figure 5.10). The relative alignment between the x-ray source and sample center was not critical as the diffraction angles were measured relative to the x-ray source only.

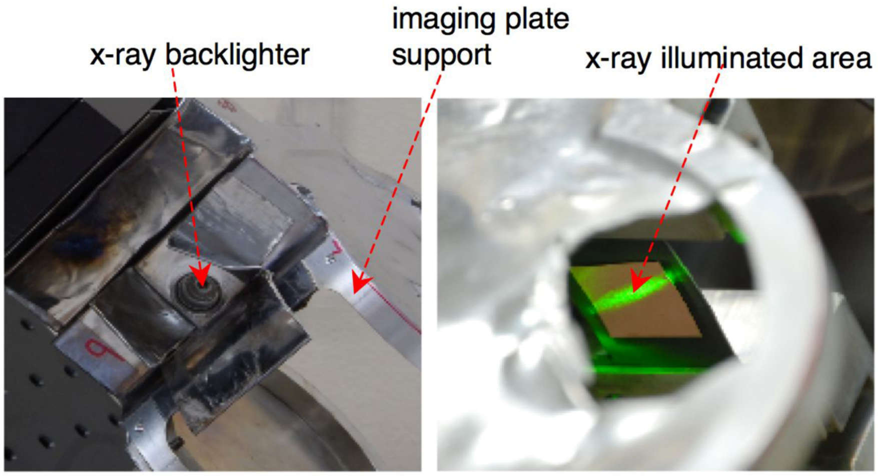

Figure 5.10. View of the x-ray backlighter and projected x-ray spot on the target using a green diode laser. The laser was used to align the target center with respect to the x-ray axis before every data shot.

The instrument response function

Knowledge of the instrument response function is necessary in applications where quantitative diffraction peak intensity information is used to identify texture, the lattice morphology upon phase transformations, or novel material structures. To derive an expression for the instrument response function, we calculated the sample absorption, the Lorentz-polarization factor (a geometric factor) and the filter absorption for the S-B geometry described. Absorption by the sample can lead to significant attenuation of the diffracted x-rays. To calculate the fraction of the incident x-ray intensity reflected by a sample of thickness z_0 as a function of θ, we assumed that a quasi-collimated (small $\delta/2$) x-ray source of unit cross sectional area impinges on the sample surface at an angle i and exits the sample surface at an angle 2θ-i (Figure 5.11).

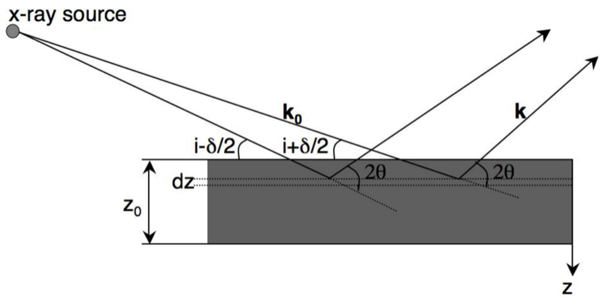

Figure 5.11. X-ray scattering from a layer of thickness dz in a sample. In the calculation of x-ray attenuation as a function of θ_{Bragg} we assumed that: a) the x-ray beam is collimated, since i>>δ and b) the sample width is infinite, since z_0 is of the order of tens of microns whereas the sample is typically several millimeters wide.

For a layer of material dz, at depth z, the volume dV in which x-ray absorption occurs is

$$\mathrm{d}V = \frac{\mathrm{d}z}{\sin \mathrm{i}}. \tag{5.1}$$

The total path length of an x-ray reaching the sample surface after diffraction from the volume element dV, at depth z, and at an angle 2θ is

$$d_{sample} = \left(\frac{1}{\sin \mathrm{i}} + \frac{1}{\sin(2\theta - \mathrm{i})}\right)z. \tag{5.2}$$

Therefore, the intensity of the diffracted beam from element dV exiting the sample is proportional to

$$\mathrm{d}I_{sample} \propto \frac{1}{\sin \mathrm{i}} \exp\left[-\mu_{sample}(\lambda)\left(\frac{1}{\sin \mathrm{i}} + \frac{1}{\sin(2\theta - \mathrm{i})}\right)z\right]dz, \tag{5.3}$$

where μ_{sample} is the wavelength dependent linear absorption coefficient of the material. Integration of equation (5.3) from z=0 to z_0 yields the fraction of the total diffracted intensity as a function of Bragg angle θ from a sample of thickness z_0, tilted at an angle i with respect to the incident x-ray direction, i.e.

$$A(2\theta)_{sample} = \frac{1-\exp[-\mu_{sample}(\lambda)(\frac{1}{\sin \mathrm{i}} + \frac{1}{\sin(2\theta - \mathrm{i})})z_0]}{\mu_{sample}(\lambda)(1+\frac{\sin \mathrm{i}}{\sin(2\theta-\mathrm{i})})}. \qquad (5.4)$$

The Lorentz factor is a trigonometric factor in diffraction peak intensity calculations that combines three geometrical terms: 1) the angular range $\delta\theta$ centered around a specific Bragg angle θ over which appreciable energy is diffracted, shown to be proportional to $\cos\theta$, 2) the fraction of grains whose plane normal is oriented to satisfy the Bragg condition within the angular range $\delta\theta$, proportional to $1/\sin\theta$, and 3) the intersection of the detector-diffraction cone for a given Bragg angle θ. Thus, the Lorentz factor for the S-B geometry becomes $\frac{\cos\theta}{\sin(2\theta-\mathrm{i})\sin 2\theta}\frac{1}{\sin\theta}$. When multiplied by the polarization factor $(1+\cos^2 2\theta)/2$ originating from electron scattering theory [99], the Lorentz-polarization (LP) factor is simplified to

$$\mathrm{LP}(\theta) = \frac{1+\cos^2 2\theta}{\sin(2\theta-\mathrm{i})\sin^2\theta}. \qquad (5.5)$$

We obtained the diffracted intensity factor due to filter absorption following the same steps as in the sample absorption calculation. Since the diffracted x-rays are incident on the filter surface at an angle 2θ-i, the path length in the filter is

$$d_{filter} = \frac{t}{\sin(2\theta - \mathrm{i})}, \tag{5.6}$$

where t is the filter thickness. Therefore, filter attenuation is given by the factor

$$B(2\theta)_{filter} = \exp[-\mu_{filter}(\lambda)\frac{t}{\sin(2\theta - \mathrm{i})}]. \tag{5.7}$$

Finally, combining equations (5.4), (5.5), (5.7), the total diffracted intensity per unit length as a function of 2θ is given by

$$I(2\theta) = \frac{1}{D}\frac{1+\cos^2 2\theta}{\sin^2(2\theta - \mathrm{i})\sin^2\theta} A(2\theta)_{sample} B(2\theta)_{filter}. \tag{5.8}$$

The additional $1/D\sin(2\theta$-i) term in (5.8) comes from the fact that diffracted intensity is proportional to the inverse of the sample-detector distance.

A plot of the instrument response function when all design parameters described in the previous section were inserted into equation (5.8) is shown in Figure 5.12. We chose a 30 μm thick Cu sample and a 25.4 μm thick Fe filter (as in the experiment described in Chapter 6). We also assumed 6.7 keV x-rays (Fe K-shell transition) to obtain the correct linear absorption coefficients for the Cu sample and Fe filter.

The calculated instrument response function exhibits a steep rise in the low 2θ range with a maximum at $2\theta_{\mathrm{max}}$=47.5°, then declining to a minimum of approximately 7.5% of its peak value at $2\theta_{\mathrm{min}}$=114°. For the angular range of 114°-167°, the instrument response increases linearly by a factor of ~2. Therefore, careful consideration must be given to experiments where important data occupies $2\theta<114°$. In most cases, critical data can be shifted from the low angle range by selection of a longer wavelength x-ray source. In addition, filters of thickness ~12.5 μm can enhance signal levels by approximately an order of magnitude. It is also evident that a S-B camera with smaller radius can increase the signal-to-noise ratio; however, potential drawbacks are a decrease in the angular resolution due to the smaller sample-detector separation and an increase in the background noise originating from sample fluorescence.

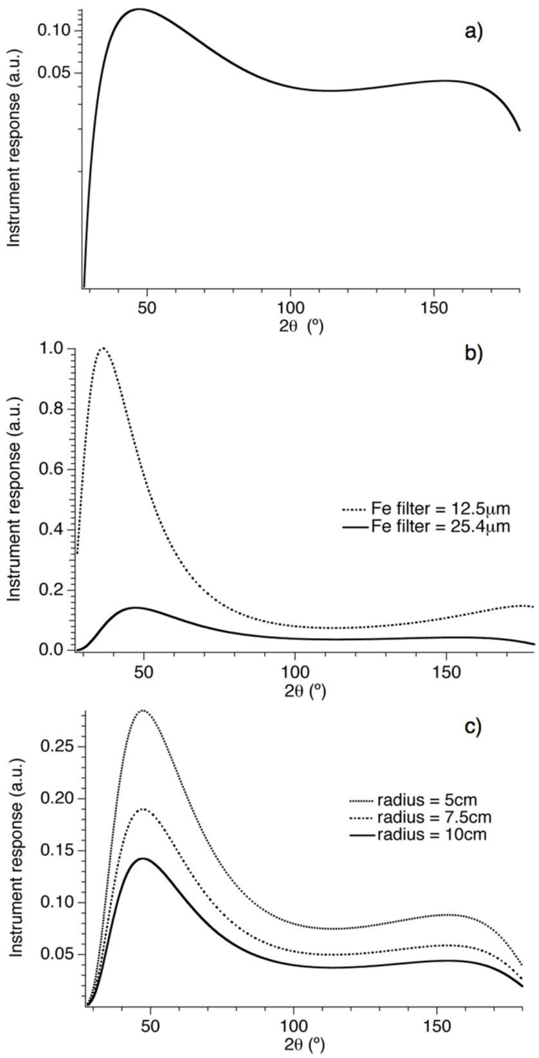

Figure 5.12. a) Plot of the instrument response as a function of 2*θ*. Factors included in the calculation of the instrument response were the x-ray filter and sample attenuation, the Lorentz-polarization, and sample-detector distance. In b), c), the instrument response dependence on filter thickness and camera radius is shown respectively.

The wide angular range of the S-B detector is highly desirable for *in situ* investigation of transient material properties induced by shock-loading. For example, observation of anisotropic compression in multiple lattice planes could be used to infer material strength as a function of loading conditions. *In situ* measurement of stacking fault densities could also be obtained from the diffraction peak shift in the 2nd and 4th orders [100]. Another application of the S-B camera stemming from both its angular range and resolution is in the acquisition of multiphase equation of state data [101-103], where the density of each phase can be extracted via measurement of the mean lattice spacing, and particle velocity via velocimetry. Here we designed a S-B camera with an angular range suitable for shock-induced melt experiments and demonstrated its capability by detecting the first two scattering peaks from an amorphous material (see Chapter 7). From theoretical and synchrotron based studies, metals of interest that undergo melt typically exhibit their first two scattering maxima between q values of 2-6 Å-1 [104, 105]. Since $2\theta = 2\sin^{-1}(\frac{q\lambda}{4\pi})$, for λ=1.85 Å (Fe K-shell wavelength), $2\theta_{\mathrm{min}}$=34° and $2\theta_{\mathrm{max}}$=124°, which is within the angular range of our S-B camera. On the other hand, the camera's limited lateral range (finite detector width) implies that diffraction rings are only partially captured. Therefore, sample texture must be pre-characterized with a diagnostic such as electron backscatter diffraction (EBSD) [106] to ensure that directional diffraction effects associated with a textured microstructure are considered.

Finally, precise determination of diffraction peak location is necessary to extract information on lattice compression and phase transitions reliably. Radial sample displacement from the focusing circle due to the finite sample/substrate thickness and the sample curvature are the primary contributors to peak location error in the S-B geometry. Mathematical expressions of these two error factors for the S-B geometry are given by $\frac{s}{2R}\frac{\sin 2\theta}{\sin \mathrm{i} \sin(2\theta - \mathrm{i})}$ and $\frac{\delta^2}{12}\frac{\sin 2\theta}{\sin \mathrm{i} \sin(2\theta - \mathrm{i})}$ respectively [107]. Assuming that the sample position is reproducible to within s=0.5 mm from the focusing circle and δ=8.2° the x-ray beam full angle, yields the error in 2θ plotted in Figure 5.13.

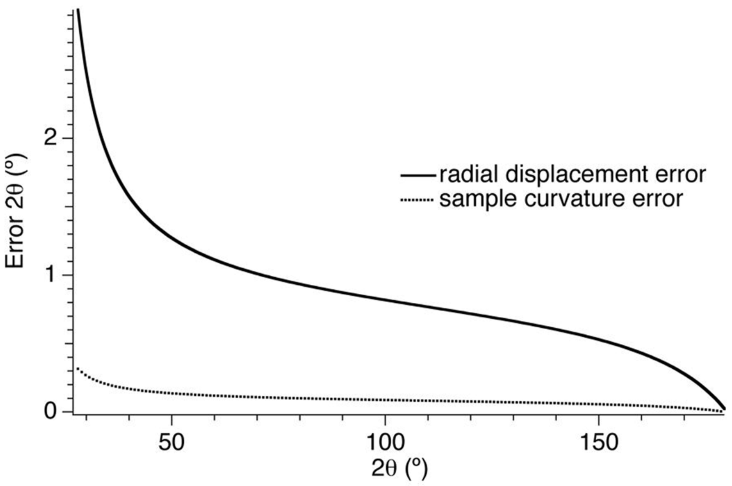

Figure 5.13. Calculation results of the error in 2θ. For the radial displacement error, a 0.5 mm displacement from the focusing circle was assumed. The error related to sample curvature was estimated considering a flat sample irradiated by an x-ray beam of 8.2° full angle.

5.3.2 THE CYLINDRICAL POWDER PINHOLE CAMERA

During the development of x-ray diffraction instrumentation to study the material response under dynamic loading, we quickly realized that the diffraction camera geometry had to be matched to the observables of the phenomenon to be studied; in other words, a single polycrystalline diffraction camera of either a Debye-Scherrer type or focusing type would have been unable to provide all the necessary information. A cylindrical Debye-Scherrrer geometry was therefore developed in parallel to the focusing geometry that allowed full diffraction rings (azimuthal angle $0 \le \phi \le 2\pi$) to be captured in contrast with the focusing geometry previously described where only a section of the rings was recorded. Such capability was aimed towards the study of the texture of the sample as a function of compression revealing possibly dynamic grain rotation [108, 109]. In addition, dynamic strength effects [110] as a function of strain rate could be quantified by the deviation of the diffraction rings from a circular to an elliptical form.

On the other hand, this cylindrical Debye-Scherrer geometry was expected to have inferior signal to noise ratio and angular resolution compared to the focusing geometry because of the divergence of the diffraction rings as a function of sample-detector distance.

The cylindrical geometry for x-ray diffraction from polycrystalline (and amorphous) materials named Cylindrical Pinhole Powder Camera (CPPC) [38] is shown below (Figure 5.14).

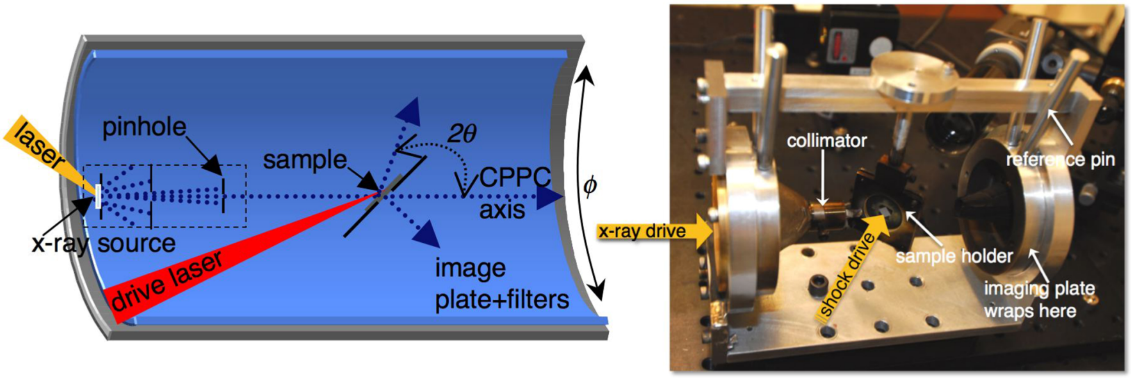
laser
pinhole
sample
2θ
CPPC
axis
φ
x-ray source
drive laser
image
plate+filters
x-ray drive
collimator
reference pin
sample holder
shock drive
imaging plate
wraps here

Figure 5.14. Illustration and photograph of the actual CPPC diffraction camera. The imaging plate detectors are not shown here in order not to obstruct the target view. Normally, the imaging plates were wrapped around the cylindrical frame of the camera.

It comprised of a cylinder with inner diameter equal to 6.5 cm and length of 12 cm. A point x-ray source was generated by laser irradiation of a thin metal foil and was subsequently collimated by two pinholes (500 μm and 1 mm in diameter) to a ~2 mm diameter spot size on the target. Since the pinholes were interchangeable, different x-ray spot sizes could be used to illuminate the target. The x-ray source and target distance was 6 cm. Positioning of the target center on the x-ray source axis was accomplished via illumination of the x-ray source pinholes with a green diode laser and subsequent alignment of the illuminated spot on the target. The Debye-Scherrer diffraction rings from grains satisfying the Bragg condition $2d_{hkl}\sin\theta=\lambda$ were recorded on imaging plate detectors wrapped around the perimeter of the cylinder. Both transmitted and reflected diffraction signals from the sample, oriented at 45^{o} with respect to the quasi-collimated x-ray source, were recorded on the imaging plate detectors. The sample orientation was selected to be at 45^{o} with respect to the x-ray axis in order to capture information on the elastic component of the strain transverse and parallel to the shock direction from as many grains as possible. In other words capturing strain information from a large number of grains in different orientations could enable an anisotropy measurement of strain along these orientations.

Appropriate filter foils (depending on the energy of the line emission) were mounted in front of the imaging plate detectors to block the continuum emission from the plasma, fluorescence from the sample itself and other noise originating from the shock drive. A typical filter package for Ti 4.7 keV He_a-like emission consisted of 37.5 µm thick Ti foil and ~25 µm thick aluminized Mylar. The latter was used to prevent exposure of the imaging plates to the 527 nm laser radiation during a shot, which would have degraded the exposure. (Exposed imaging plates are scanned by a green diode laser causing fluorescence in the regions where atoms had been excited by x-ray irradiation. Therefore, exposure to optical radiation before scanning can result in atomic de-excitation, thus reducing the signal amplitude emitted from the imaging plate during scanning). For Fe 6.7 keV x-rays we found that a combination of 25 µm thick Fe foil and 25 µm thick aluminized Mylar provided the signal to noise necessary for x-ray diffraction measurements from Mg. In general, the above filter assemblies were customized depending on the x-ray scattering properties of the material in question by increasing or decreasing the foil thickness corresponding to the x-ray backlighter material by 12.5 μm until the desirable signal to noise ratio was attained. The same approach for signal to noise optimization was also used in the focusing geometry described earlier.

The diffraction signal recorded in this cylindrical arrangement took the form of straight lines in the transmitted and reflected directions at the corresponding Bragg angle 2θ upon unfolding the imaging plates. Thus, the data analysis was simplified considerably by the use of a cylindrical geometry. The dispersion relation for the CPPC that was used to translate distance on the imaging plate (or pixel) to angle 2θ was

$$\begin{aligned} 2\theta &= \tan^{-1}\left(\frac{3.25cm}{6cm - C\left[\frac{cm}{pixel}\right]\cdot pixel\,\#}\right) \text{ for pixel\# } < \frac{6cm}{C\left[\frac{cm}{pixel}\right]} \quad \text{(in reflection)} \\ 2\theta &= 180^\circ - \tan^{-1}\left(\frac{3.25cm}{C\left[\frac{cm}{pixel}\right]\cdot pixel\,\# - 6cm}\right) \text{ for pixel\# } \geq \frac{6cm}{C\left[\frac{cm}{pixel}\right]} \quad \text{(in transmission)} \end{aligned} \qquad (5.9)$$

where $C\left[\frac{cm}{pixel}\right]$ a distance/pixel calibration obtained from the known imaging plate dimensions and the corresponding number of pixels in that dimension. In this case, the dimension of interest was along the cylinder axis so that distance along this axis was converted to Bragg angle 2θ. A plot of the dispersion relation is also shown below (Figure 5.15). A more detailed characterization of the CPPC camera and its signal properties can be found in J. Hawreliak's publication [38].

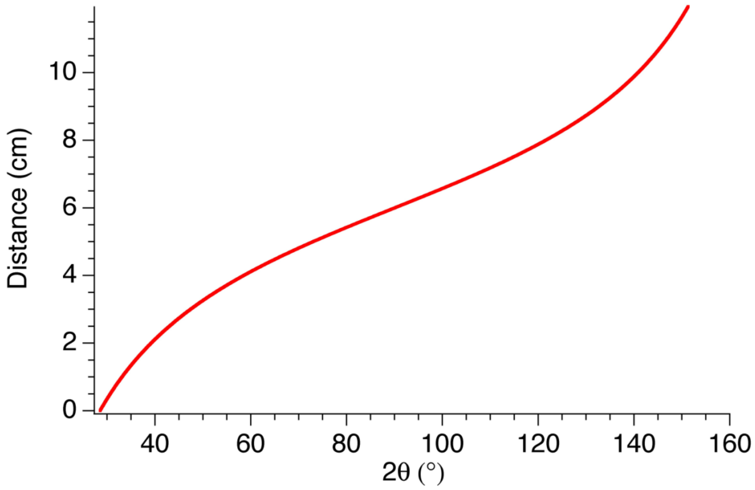

Figure 5.15. Plot of the CPPC angular dispersion as a function of distance of the unwrapped imaging plate.

5.4 Two-Channel Line-Imaging Velocimetry

Optical diagnostics have been the principal tools in the characterization of shocked materials for several decades. Interferometric diagnostics in particular have been widely used in shock-wave experiments since the development of the velocity interferometer system for any reflector (VISAR) by Barker et al. [111] to measure gas-gun and explosively driven shocks. Since then VISAR has been implemented for a variety of measurements in the realm of dynamic loading such as free surface and interface velocity measurements, equation of state and reflectivity measurements, as well as a means for synchronization of x-ray backlighter pulses with shocks. Currently VISAR systems available at facilities such as OMEGA, JANUS, and NIF are capable of recording shock/interface velocities as high as 50 km/s and with precision of ~1% [112]. In our experiments VISAR served as a diagnostic of free surface velocity and shock speed. In addition, VISAR assisted in the timing of our pump-probe measurements when parylene-N coated targets were used. In these experiments the x-ray pulse had to be synchronized with the shock arrival at the parylene-N/sample interface, so VISAR shock breakout data coupled to hydrodynamic simulations facilitated this timing. Furthermore, observation of Mg in its elastic-plastic regime was achieved by resolving the elastic and plastic waves in VISAR traces.

5.4.1 BACKGROUND ON DOPPLER VELOCIMETRY

A VISAR system typically employs a single-mode pulsed laser probe that is incident normally on the surface whose velocity needs to be measured. Upon back-reflection from this moving surface the Doppler shifted probe beam is split into the two arms of an interferometer and recombined on the 2nd beamsplitter as shown in Figure 5.16. An image of the interference pattern is then relayed onto the slit of a streak camera detector where spatial and temporal information is captured.

The VISAR interferometer is a Mach-Zehnder configuration with a temporal delay τ introduced in one of its arms. This temporal delay is achieved by placing an etalon of precisely known length h and refractive index n in the interferometer arm and by displacing the etalon-mirror assembly along a direction perpendicular to the mirror plane. The displacement is such that the *apparent* position of the mirror plane as viewed through the etalon is equal to the original mirror plane position without the etalon, that is the mirror position where there is zero path delay between the two interferometer arms.

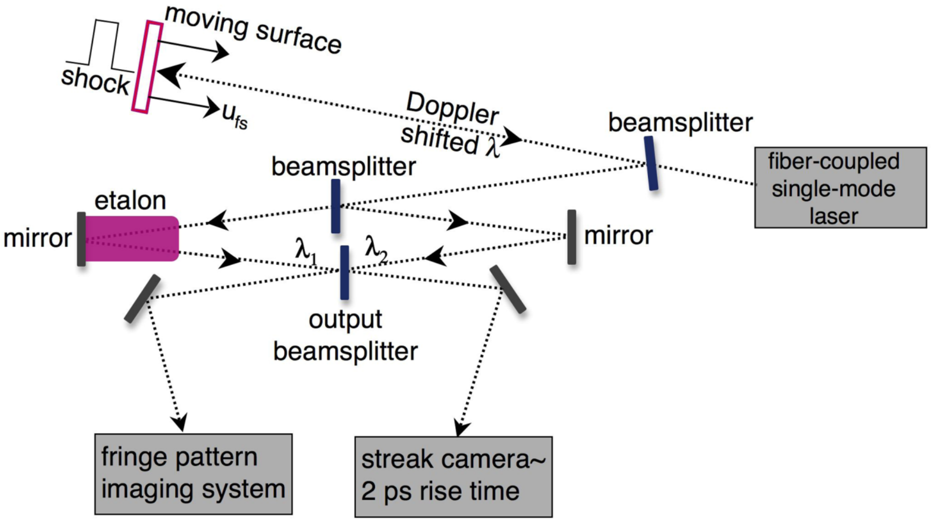
moving surface
shock
u_{fs}
Doppler shifted λ
beamsplitter
fiber-coupled single-mode laser
beamsplitter
etalon
mirror
mirror
λ1
λ2
output beamsplitter
fringe pattern imaging system
streak camera~ 2 ps rise time

Figure 5.16. Diagram of a typical VISAR system. The Doppler shifted VISAR probe beam is injected into a Mach-Zehnder-type interferometer after back-reflection from the moving surface. An etalon introduces a temporal delay in one of the interferometer arms resulting in interference of beams with slightly different wavelength on the reflecting surface of the output beamsplitter. The fringe pattern formed is imaged onto a streak camera to obtain temporal and spatial information .

The resulting temporal delay τ from such an arrangement is

$$\tau = \frac{2h}{c}\left(n - \frac{1}{n}\right) \tag{5.10}$$

where c is the speed of light. The etalon-mirror translation distance d required for correct placement of the apparent mirror plane is

$$d = h\left(1 - \frac{1}{n}\right) \tag{5.11}$$

Since the interfered beams have a relative time delay, a change in the Doppler shifted wavelength of the VISAR probe e.g. because of acceleration of the probed surface, results in interference of beams with a wavelength difference $d\lambda$. Considering that the optical phase difference ϕ in the arms is given by

$$\phi = \frac{2\pi}{\lambda}(c\tau) \tag{5.12}$$

we can represent the resulting phase shift due to a wavelength shift by

$$|d\phi| = \frac{2\pi c\tau}{\lambda}\left|\frac{d\lambda}{\lambda}\right|. \tag{5.13}$$

Since the Doppler shift can be associated to a moving surface velocity u_{fs} by

$$\left|\frac{d\lambda}{\lambda}\right| = \frac{2u_{fs}}{c} \tag{5.14}$$

the phase obtained in the VISAR trace is related to the free surface velocity by

$$|d\phi| = \frac{4\pi\tau}{\lambda}u_{fs} \tag{5.15}$$

A phase shift is typically demonstrated in a VISAR trace by a fringe displacement *y(t)* along the spatial axis of the streak camera record (Figure 5.17). Quantitatively, the phase shift is associated to $y(t)$ $d\phi = 2\pi \cdot y(t) / D$ where D the fringe spacing. Therefore, the expression for the surface velocity measured by VISAR becomes

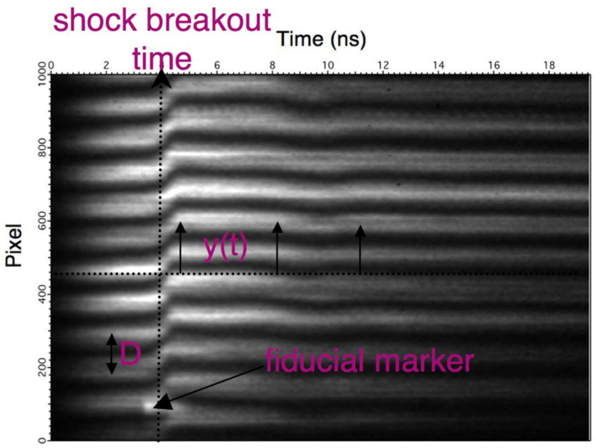

Figure 5.17. Example of a VISAR trace, namely a streaked interferogram with subnanosecond temporal resolution. The quantities extracted from a VISAR trace are typically the fringe shift y(t) and spatial frequency 1/D, the shock breakout time and occasionally reflectivity as a function of time. From the first two quantities the fringe phase can be extracted from which the surface velocity can be calculated.

$$u_{fs}(t) = \frac{\lambda}{2\tau D} y(t) . \tag{5.16}$$

There are several corrections introduced to the above expression to account for the dispersion in the etalon material, the angle of incidence of the VISAR laser probe on the target and possible window materials used as target substrates. These corrections and values for different window materials can be found in the paper by Celliers [112].

5.4.2 JANUS VISAR DESCRIPTION AND OPERATION

The two-channel line-imaging VISAR system employed in our surface velocity measurements from single and polycrystalline materials was that of the JANUS laser facility. The author also setup two additional VISAR systems at the Sandia National Laboratory Z-beamlet facility, Los Alamos National Laboratory Trident facility, and constructed a portable VISAR system for synchrotron dynamic measurements at the Argonne Photon Source. Only the JANUS VISAR is presented here since this system was used for the measurements relevant to this dissertation.

A schematic of the JANUS VISAR is shown in Figure 5.18. A 532 nm, 50 mJ, 50 ns Nd:YAG single-mode laser was coupled into a large core (1mm diameter) multimode fiber and propagated for several meters in order to accomplish a smooth speckle pattern. The use of a single-mode (injection seeded type) laser having a coherence length of ~2 m (130 MHz linewidth) was required to obtain interference from the two temporally separated beams in the VISAR interferometer. The output of the multimode fiber was relay imaged to the target surface with a 1:1 ratio. The focusing/collection lens from target was a multi-element achromatic lens with a 14.5 cm focal length and 2 in. diameter. This was the shortest focal length (largest numerical aperture) lens we could have accommodated in our setup for efficient light collection from the shock-breakout surface. To protect the lens from shocked material debris a blast shield (~2 mm thick AR coated glass substrate) was placed in front of the lens and was replaced on every shot. The collected light reflecting from the target's moving surface was subsequently relayed back to the interferometer table shown in Figure 5.18 and split into the two interferometers. Having two velocimetry channels enabled us to choose two etalons (UV grade fused silica, AR coated) one with high and one with low fringe sensitivity or VPF (velocity per fringe [km/s/fringe]). This capability proved to be necessary for data where multiple fringe jumps occurred or where the fringe shift direction in one of the velocimetry channels was ambiguous. The etalon lengths used in our experiments and the corresponding VPF is shown in Table 5.1. The VPF was calculated from the expression $VPF = \frac{\lambda}{2\tau(1+\delta)}$ for a wavelength of 532 nm taking into account a dispersion factor $(1+\delta)$ where $\delta = 0.0318$ for fused silica.

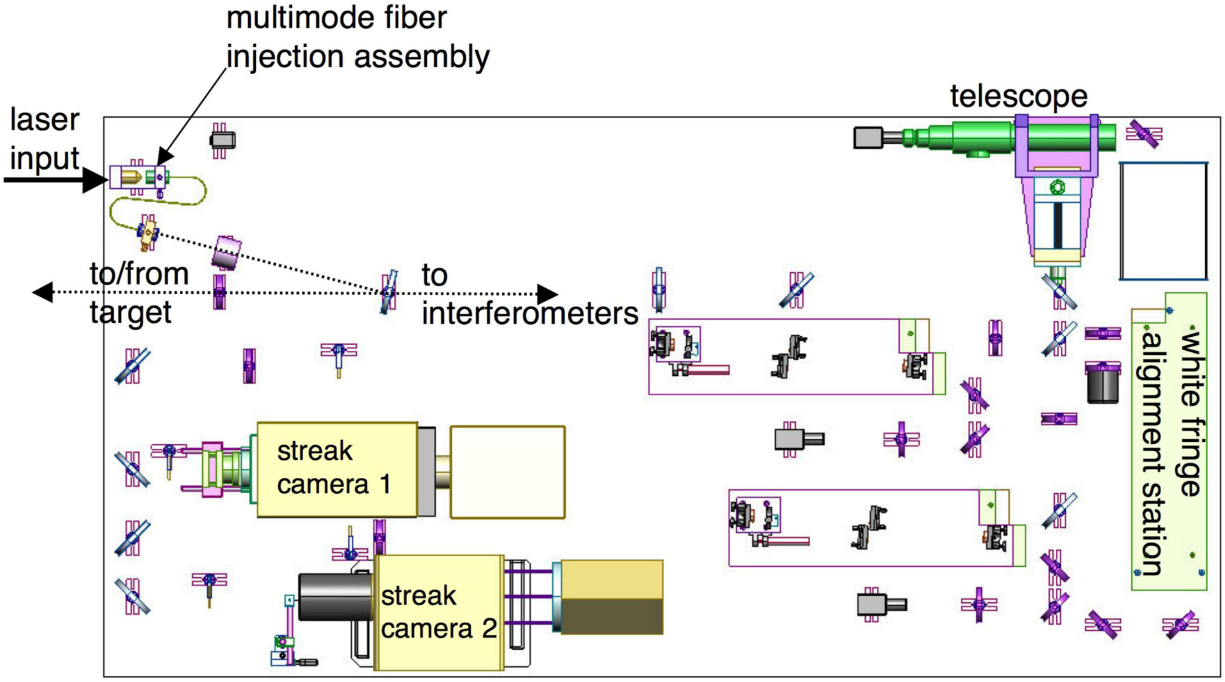
multimode fiber injection assembly
laser input
telescope
to/from target
to interferometers
streak camera 1
streak camera 2
white fringe alignment station

Figure 5.18. JANUS two-channel line imaging VISAR system.

Table 5.1 Selected etalon characteristics used in JANUS experiments.

Etalon thickness *h* (cm)	End mirror displacement (μm)	Time delay τ (s)	VPF (km/s/fringe)
0.466	1472.29	2.415 E-11	**10.677**
0.815	2574.47	4.222 E-11	**6.106**
1.164	3678.71	6.033 E-11	**4.273**
1.518	4797.53	7.868 E-11	**3.277**
7.391	23358.72	3.831 E-10	**0.673**

In each interferometer the image of the target was relayed onto the output beamsplitter. To ensure that the image of the target was relayed on the face of the output beamsplitter, a telescope was setup imaging that plane. The multi-element VISAR lens in front of the target was translated until a well-focused image appeared on the telescope monitor. An interference pattern superimposed on the target image appeared on the face of the output beamsplitter when light from both arms were allowed to overlap. The tip-tilt adjustments of the output beamsplitter were adjusted to produce the desired fringe spacing and orientation. It is important to note that at the beginning of an experimental campaign the zero delay position of the interferometer arms was checked with a white light source. The extremely short coherence length of such a light source enabled determination of the zero delay position to ~1 μm.

Last, when an interference pattern with satisfactory fringe contrast was established on the output beamsplitter, it was relay imaged to the streak camera (Hamamatsu C7700) ~100 μm wide slit such that the full width (~ 2.5 cm) of the slit was illuminated. A cylindrical lens before the streak camera slit condensed the image to a line in order to increase the streak record intensity. In addition to the interference pattern, a fiducial was injected into the streak camera to establish a relative timing with the shock drive (WEST) beam. Temporal overlap of the fiducial and WEST beam was accomplished by directing the WEST into the VISAR path and imaging it on the streak camera. An appropriate delay was then introduced by a DG 535 (digital delay generator) box such that the fiducial and WEST beam signal were temporally overlapped.

5.4.3 VISAR FREE SURFACE VELOCITY EXTRACTION

The interferograms recorded in our experiments were analyzed to extract fringe phase and thus, surface velocity as a function of time and space. There are several methods that can extract phase information from interferograms. We used a Fourier transform method (FTM) developed by Takeda and others [113, 114] where the fringe intensity is initially represented by a function

$$\begin{aligned} S(x,t) &= B(x,t) + C(x,t)\exp\left(2\pi i f_0 x + i\delta_0\right) + c.c. \\ &= B(x,t) + A(x,t)\exp\left(i\phi(x,t)/2\right)\cdot\exp\left(2\pi i f_0 x + i\delta_0\right) + c.c. \end{aligned} \tag{5.17}$$

where $B(x,t)$ the average un-modulated intensity background, $A(x,t)$ the fringe amplitude, $\phi(x,t)$ the phase to be determined, f_0 the fringe frequency, and δ_0 an arbitrary constant phase. The FTM then proceeds by taking the Fourier transform of equation (5.17) at fixed time

$$s(f,t) = b(f,t) + c(f - f_0,t) + c^*(f - f_0,t)\,, \tag{5.18}$$

and applying a filter that isolates the power spectrum around the c-lobe. An inverse Fourier transform of the filtered power spectrum yields a "wrapped" phase (bounded in a $[-\pi,\pi]$ interval), which is subsequently unwrapped removing any 2π discontinuities. The phase background given by $2\pi f_0 x+\delta_0$ is also subtracted. An illustration of this process using a VISAR algorithm developed by D. Hicks at LLNL is shown in Figure 5.19.

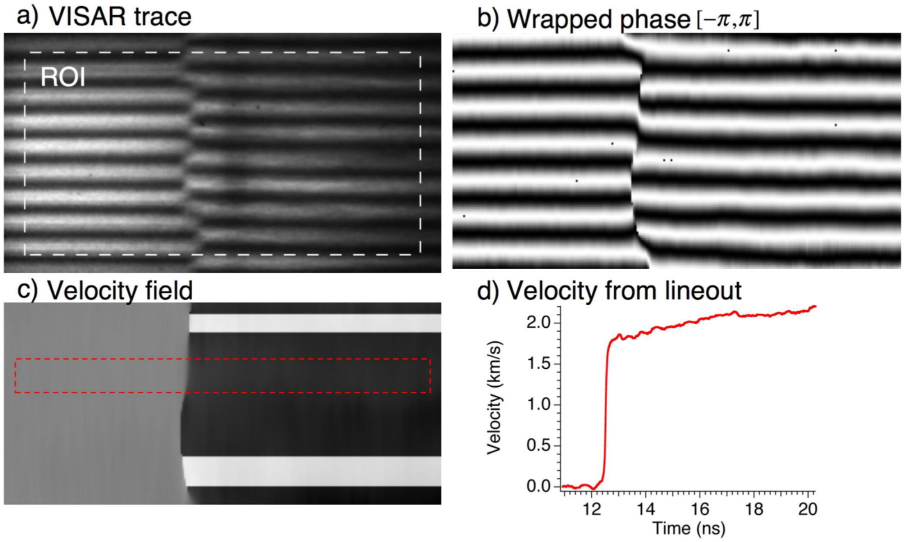

Figure 5.19. Surface velocity extraction procedure from VISAR streak camera record. a) The VISAR trace recorded depicting the region of interest (ROI) selected. b) After application of a Fourier transform algorithm and further processing steps involving frequency filtering and an inverse Fourier transform, a wrapped phase function W(t) is extracted. c) The velocity field obtained after unwrapping the phase function and d) the velocity profile from the lineout (in red) .

This method successfully extracted the surface velocity from the fringe patterns recorded except for the cases where discontinuities in the fringes at shock-breakout were present or when substantial loss of reflectivity from the interrogated surface occurred (Figure 5.20). For the former data, the user had to "guess" the correct direction of the fringe jump by observing the direction of the fringe jump for lower pressure records where discontinuities were not evident or by comparison with the second VISAR channel. Another way to define fringe jump direction was by an estimate of the expected velocity from hydrodynamic simulations. Subsequently, the program was instructed to implement the correct fringe jump direction. For VISAR streak records where fringe loss occurred due to poor target reflectivity upon shock-breakout, the breakout time and target thickness was used to infer the shock speed and thus, the shock pressure using a tabulated equation of state.

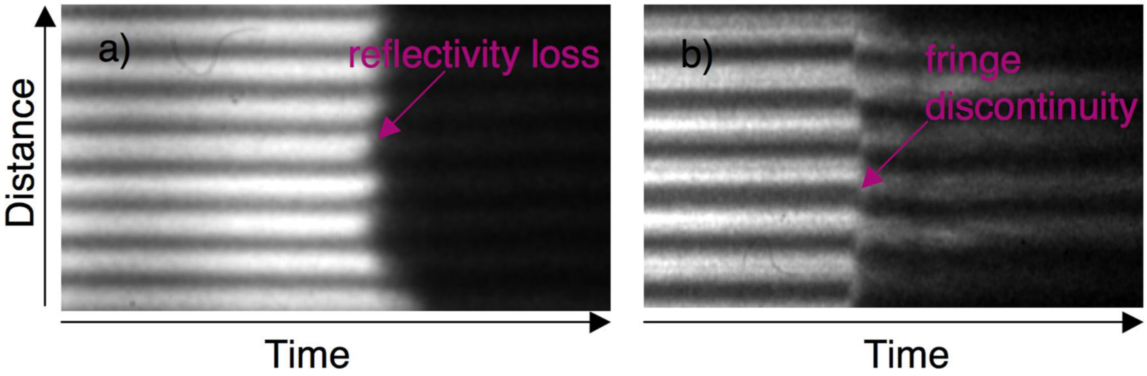

Figure 5.20. Examples of ambiguous VISAR traces because of a) reflectivity loss upon free surface expansion, b) fringe jump discontinuity. In the latter type of traces, an educated guess of the fringe jump direction was made based upon the irradiance of the shock drive and comparison with the second VISAR channel.

5.5 Beam Alignment Diagnostics

We performed single lens imaging of the x-ray backlighter and shock drive laser spot size. We used achromatic AR coated lenses with a variety of focal lengths for adjusting the magnification of the imaging system such that the CCD chip (6 mm x 4 mm) of the WATEC camera used was almost completely filled. For imaging the laser focus on the x-ray back lighter foil, the imaging system was placed at the entrance of the diffraction camera as shown in Figure 5.3, and a motorized shield ensured that the lens was blocked before every shot. The 10 Hz alignment beam was pointed in this way with an accuracy of ~ 100 μm to the center of a 600 μm diameter washer that held the x-ray backlighter foil.

Alignment of the shock drive was even more critical for our experiments since any misalignment compromised both the VISAR probe overlap and the x-ray backlighter overlap. Since the imaging plate detectors used in our diffraction cameras obstructed the direct view of the target, an equivalent plane imaging system was setup to confirm the location of the shock drive spot before every shot. Specifically, after the shock drive location was defined on the target, a mirror was placed to deflect the shock drive beam away from the target. The equivalent target plane on the deflected laser beam was then imaged by looking at the distance where the spot size (the image of the 1 mm phase plate) was at best focus. The image of the equivalent target plane was marked on a monitor. After replacing the target for a data shot, the beam was aligned into the marked area on the monitor (Figure 5.21). The mirror deflecting the shock drive laser beam was then removed and the target was irradiated on the pre-determined area with an accuracy of ~100 μm.

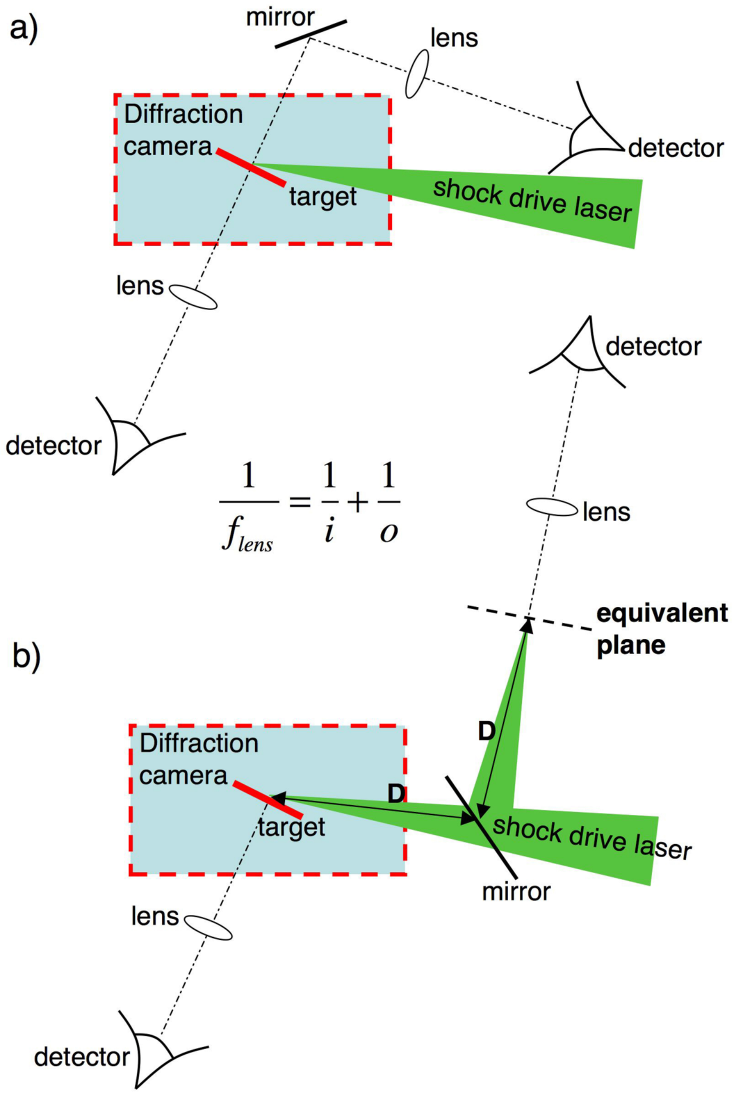
a)
mirror
lens
Diffraction camera
target
shock drive laser
detector
lens
detector
detector
$\frac{1}{f_{lens}} = \frac{1}{i} + \frac{1}{o}$
lens
equivalent plane
b)
D
Diffraction camera
D
target
shock drive laser
mirror
lens
detector

Figure 5.21. Optical setup for imaging the shock driven area by a) standard single lens imaging, and b) by an equivalent plane imaging configuration. In the latter, a motorized vacuum controlled mirror is inserted in the path of the shock drive laser and the equivalent target plane, i.e. the plane at a distance equal to the mirror-target distance is imaged.

6 EXPERIMENTAL RESULTS

In this chapter, the results of the three main experiments executed during the course of this PhD study are presented. The common premises of these experiments were laser-induced shock-loading of polycrystalline samples, nanosecond lattice measurements obtained by the diffraction instrumentation developed throughout this research effort, and free surface velocimetry for characterization of the material response.

We begin with the results of a proof of principle density measurement using dynamic x-ray diffraction in the Seeman-Bohlin diffraction geometry. The purpose of this measurement was to demonstrate the superior signal to noise and angular resolution of the focusing diffraction geometry, thus assessing its capability in future equation-of-state measurements, as well as experiments where the diffracted signal amplitudes are expected to be low. The relevant example for this study is phase transition experiments, where low diffraction signals are expected from the partially transformed lattice. The second experiment presented in this chapter describes our time-resolved measurement of the hcp to bcc phase boundary on the principal shock Hugoniot in Mg. The results here are of great significance since the low uncertainty of our data allowed us to define the hcp-bcc boundary in Mg, thus differentiating for the first time among various hcp-bcc boundary models with considerable discrepancies in pressure and temperature. Finally, our experimental efforts in diagnosing shock-induced melt are described. Even though direct evidence of melt was not attained due to low signal to noise in x-ray diffraction and loss of reflectivity in velocimetry, the progress towards shock-induced melt studies is presented.

6.1 Density Measurement of Shock-Compressed Copper

Our early experiments aimed in demonstrating the capability of the focusing Seeman-Bohlin camera in equation-of-state measurements, where particle velocity and material density must be captured simultaneously. We performed these experiments using the Seeman-Bohlin camera described earlier to detect lattice compression and thus density of shocked Cu, together with VISAR for free surface velocity measurement (Figure 6.1). Experiments were performed in the JANUS target chamber for generating a laser plasma x-ray source synchronous to nanosecond shock-loading. A thermally excited He-like plasma was generated on the surface of a 9 µm thick Fe foil by focusing the JANUS EAST beam (527 nm, 2 ns, ~300 J) to a ~120 µm diameter focal spot. X-rays resulting from the 1s2p -1s^2 ^{1}P-^{1}S (1.8505Å) and 1s2p - 1s^2 ^{3}P-^{1}S (1.8595 Å) e$^-$ transitions were emitted over 4π steradians. Approximately 35% of the 6.7 keV Fe K-shell x-rays were transmitted through the Fe foil.

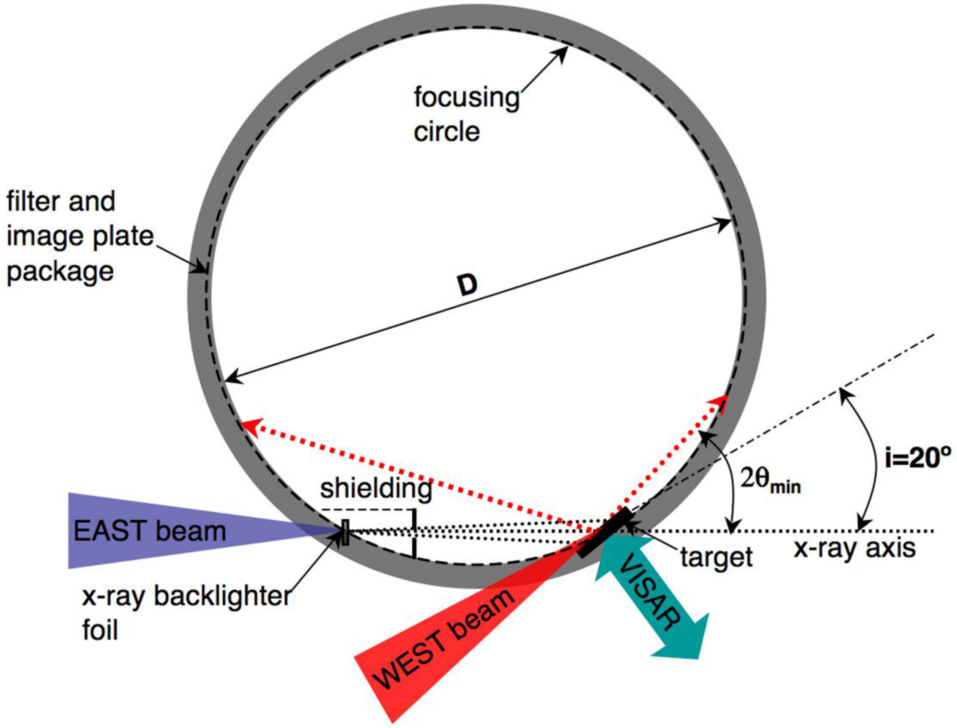
focusing
circle
filter and
image plate
package
D
i=20°
$2\theta_{min}$
shielding
EAST beam
target
x-ray axis
x-ray backlighter
foil
WEST beam
VISAR

Figure 6.1. (not to scale) The experimental geometry for laser driven shocks and dynamic x-ray diffraction studies in Cu using the S-B camera.

Samples of 25 μm thick, 99.99% pure, Cu rolled foil were ablatively shock-loaded with an irradiance of around $4x10^{11}$ W/cm^{2} provided by the JANUS WEST beam (527 nm, 4 ns). An example of our shock and x-ray backlighter drive waveforms is presented in Figure 6.2. Despite requesting for a smooth flat top temporal profile, there existed considerable fluctuations in the laser waveforms because of problems in the pulse-shaping code input. However, we did not expect that the fluctuations depicted here to result in significant pressure variations since these irradiance variations are smoothed out during the shock formation process. On the other hand, spatial intensity fluctuations in the laser spot contributed to significant discrepancies in the pressure calibration between shots, as it will be explained later.

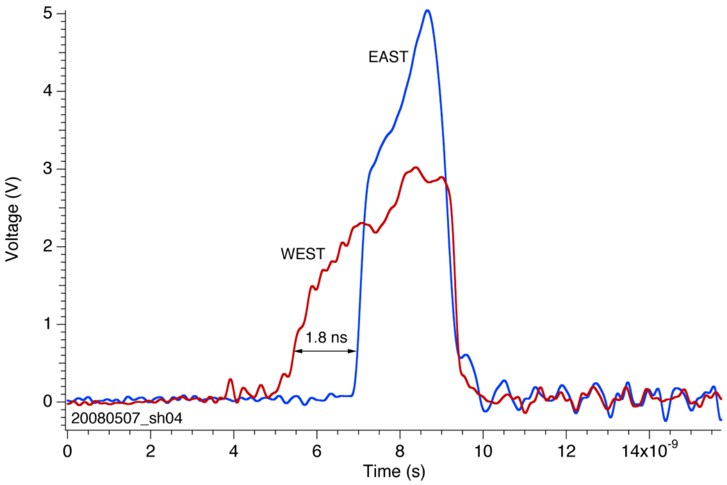

Figure 6.2. Laser waveforms for the EAST (x-ray backlighting) at 313 J, 2ns, and the WEST (shock drive) at 224 J, 4 ns. A delay of 1.8 ns delay was present in the EAST relative to the WEST beam. Even though there were considerable fluctuations in the amplitude of the WEST, hydrodynamic simulations have shown that the material response smoothes these fluctuations out during shock formation.

The 4.7 μm x-ray probe depth (attenuation length of 6.7 keV x-rays at 20.5 ° incidence in Cu) was sufficient for interrogating the lattice structure past the ablation front (<1 μm). The velocity history of the sample's rear free surface was measured for every shot over a ~1 mm diameter spot by the two-channel line-imaging VISAR. The fringe constant for each channel was 0.997 km/s/fringe and 3.316 km/s/fringe respectively. Because of an oxide layer that was present on the back surface of the foils, the reflectivity of the VISAR probe was low. Upon breakout reflectivity dropped dramatically and for this reason (and because of limited number of available shots), only two data points with good VISAR data were obtained for Cu (Figure 6.3).

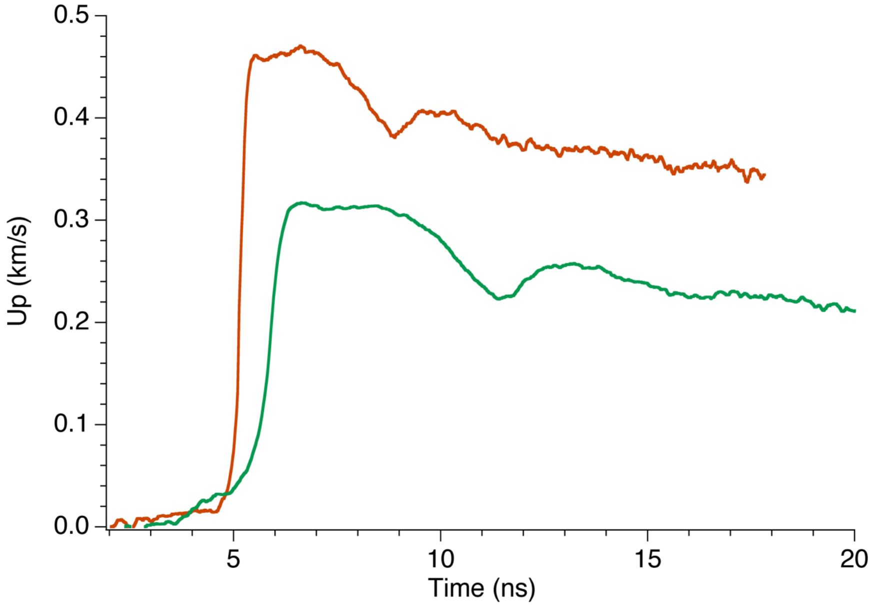

Figure 6.3. Particle velocity profiles extracted from VISAR interferograms after probing the free surface expansion of shock-compressed Cu foils. The peak particle velocity of the two records shown are 0.48 km/s and 0.32 km/s respectively. Spallation is evident as a "dip" in the velocity sometime after the release wave has back-propagated into the sample.

In most dynamic x-ray studies, it is important to record diffraction patterns from the static lattice to provide an absolute instrument calibration as well as to measure material texture and peak width for each sample. In our geometry we acquired signals from both the un-shocked and shocked region of the Cu foil in a single shot by having an x-ray source projection that was ~4x the drive area in addition to appropriate pump-probe timing. The temporal overlap between the drive and x-ray pulse was arranged such that the ~2 ns pulse of 6.7 keV x-rays arrived at the sample surface 1.5 ns after the leading edge of the flat top, 4 ns, drive pulse. This allowed the shock front to propagate a distance of approximately 7.5 μm into the sample before the x-rays turned on. The static sample texture was also pre-characterized using the cylindrical (CPPC) geometry described in Chapter 5 coupled to a laboratory Cu Kα source. In this way, we were able to deduce qualitatively that there was no significant texture (preferential grain orientation) that would have affected our measurements, especially since the Seeman-Bohlin camera only partially records the diffraction rings from the sample (Figure 6.4). As it can be seen in Figure 6.4, the grain size of the sample was small enough that the diffraction rings from the rolled Cu foil appeared to be smooth (no granularity).

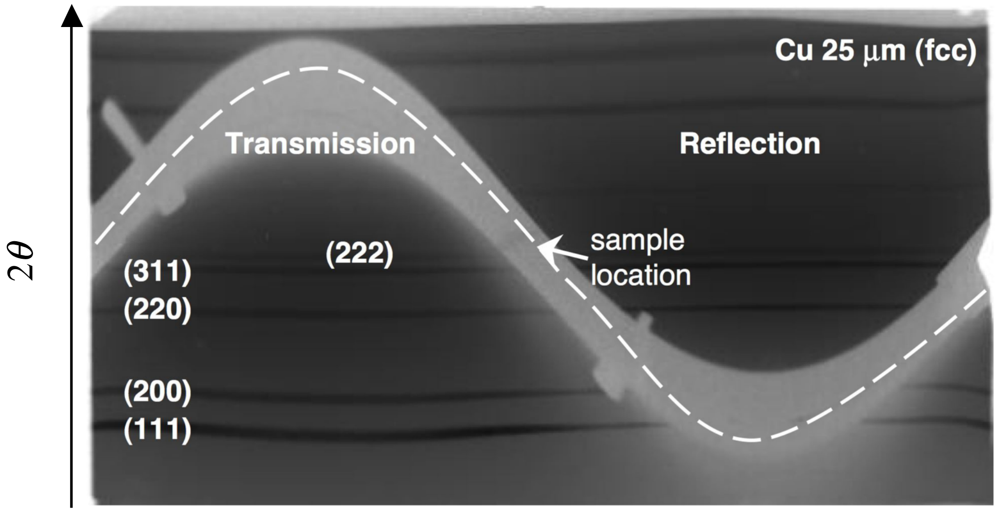

Figure 6.4. Static diffraction data from a 25 μm thick rolled Cu foil illunimated by a collimated laboratory Cu Kα source for a qualitative texture and grain size characterization.

From this study, we reported the first lattice-level measurement from a shock-loaded polycrystalline target using a S-B focusing x-ray diffraction geometry. Spatially and temporally integrated x-ray signal from the un-driven regions of the Cu foil exhibited sharp diffraction lines (Figure 6.5). Line profiles were extracted from the central 1mm portion of the imaging plate, as 3D effects were evident in the curvature and broadening of the diffraction peaks away from the center of the diffraction pattern because of focusing in a single plane.

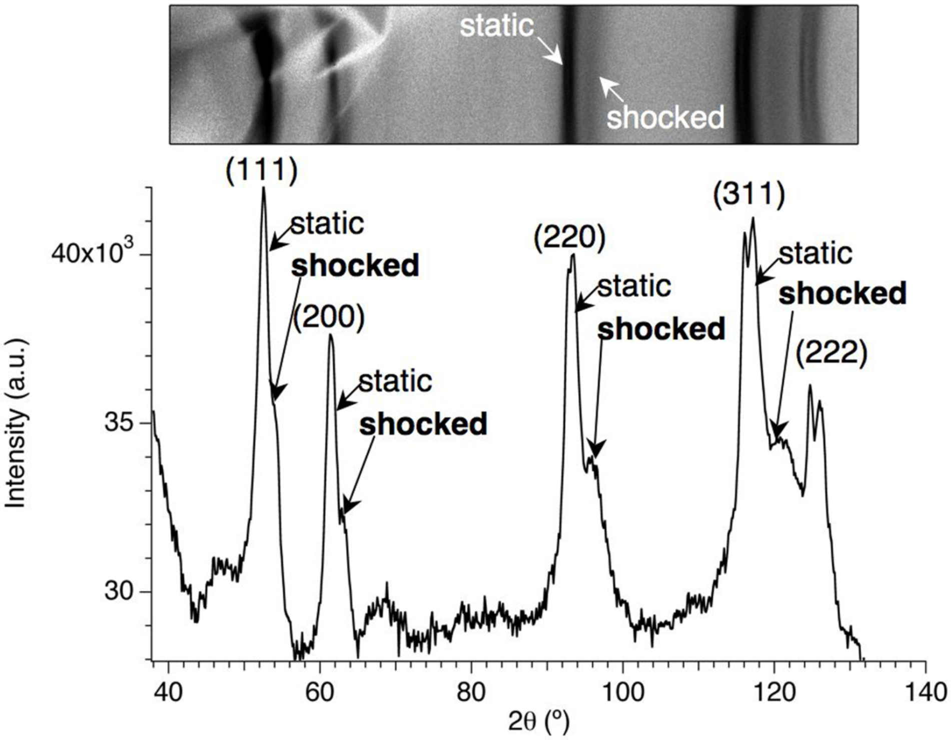

Figure 6.5. Diffraction image from shocked polycrystalline Cu at 13 GPa probed by a 6.7 keV, 4 ns x-ray pulse. Line profiles taken from the center of the diffraction pattern clearly depict static and shocked diffraction signal from all Cu (*hkl*) planes within the angular range of the detector except for (222) (low shocked signal amplitude).

Cu (*hkl*) planes were assigned to the corresponding diffraction peaks by using the relation $2\theta = 2\theta_0 + \Delta 2\theta = \frac{\mathrm{X}}{\mathrm{D}} + 2\theta_{\min}$, where θ_0 the static Bragg angle, $\Delta 2\theta$ the measured peak shift, and X the distance between a fiducial marker at $2\theta_{\min}$=28 ° and a diffraction peak along the length of the imaging plate. Furthermore, the ratio of the Hugoniot end-state to the initial material density in the (220) plane was calculated. Assuming hydrostatic compression, the ratio of compressed to static density becomes

$$\frac{\rho}{\rho_0} = (\frac{d_0}{d})^3 = (\frac{\sin({}^{2\theta}\!/_{2})}{\sin({}^{2\theta_0}\!/_{2})})^3, \tag{6.1}$$

where d, d_0 is the compressed and static interplanar spacing respectively. The calculated Bragg angle 2θ as a function of the density ratio for different lattice planes in Cu using either a 6.7 keV (Fe) or 8.4 keV (Cu) x-ray backlighter is illustrated in Figure 6.6.

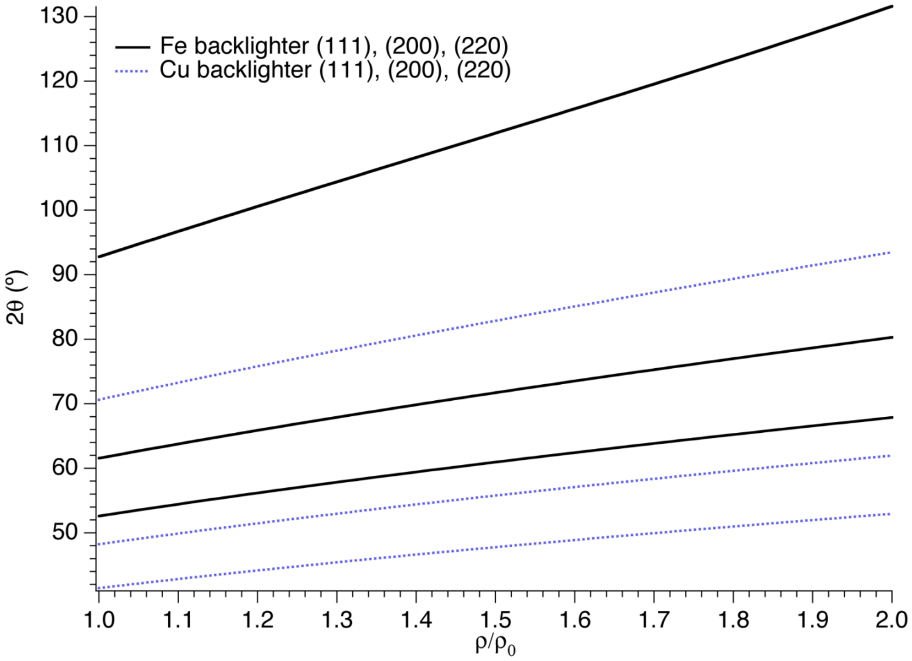

Figure 6.6. Plot of diffraction angle 2θ vs. compressed to static density ratio for the fcc lattice of Cu. The expected angle as a function of density is shown for compressed (111), (200), and (220) planes probed by a 6.7 keV (Fe) and an 8.4 keV (Cu) x-ray source.

The above plot was used as a quick reference during experiments to identify the range of compressions captured for different loading conditions, from the diffraction peak shift of a given lattice plane.

We estimated a peak shock pressure of 13+/-1 GPa from the velocity profiles of Figure 6.3 by combining the Rankine-Hugoniot equation $P = \rho_0 U_s U_p$ and a Cu EOS given by $U_s = 3.94\times10^3 (m/s) + 1.49\times U_p$ [43], where P is the shock pressure, U_s the shock speed, and U_p the particle speed. It is important to note that as the shocked material released into vacuum, we assumed that U_p was approximately 1/2 the free surface velocity measured by the line-imaging VISAR. In addition, the particle velocity measured by velocimetry and the compressed to static density ratio determined from diffraction were plotted (Figure 6.7).

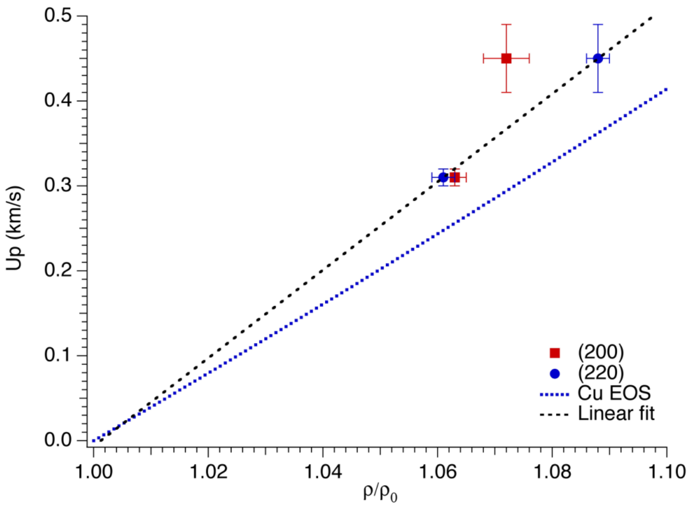

Figure 6.7. Plot of the particle velocity as a function of the compressed to static density ratio for polycrystalline Cu. This was a proof of principle equation-of-state measurement using velocimetry for particle velocity and x-ray diffraction for density determination .

Thus, we were able to demonstrate an equation-of-state measurement from Cu where in terms of U_p and $\frac{\rho}{\rho_0}$, $U_p = \dfrac{C_0}{\dfrac{1}{1-\left(\frac{\rho}{\rho_0}\right)^{-1}} - S}$ (see Chapter 2). For $\frac{\rho}{\rho_0} \rightarrow 1$, $U_p \approx -C_0 + C_0 \cdot \frac{\rho}{\rho_0}$ and from our data $C \sim 5.19\, {}^{km}\!/_{s}$. Unfortunately, as previously mentioned, the surface finish of our targets resulted in poor VISAR reflectivity for several of our data points. For only the two points displayed we were able to capture good diffraction and velocimetry data. Furthermore, the discrepancy between the linear fit provided by our two data points and the Cu EOS could be explained by spatial variations in the laser intensity profile, which would have resulted in pressure fluctuations. These variations stemmed from the fact that in order to accomplish a large drive area on the sample (and thus a large diffraction area) we did not employ a phase plate to focus the drive laser beam. Therefore, the driven target area imaged on the streak camera of our VISAR may have sampled free surface velocities that did not exactly translate to the average lattice compression measured by x-ray diffraction over a larger area. Thus, even though the S-B instrument proved to be suitable for EOS studies, accurate measurements would require the use of appropriate drive beam smoothing.

In addition, to declare EOS measurements as "absolute" the shock speed should have been obtained instead of particle velocity, since particle velocity is not measured directly from velocimetry (free surface velocity is). In these experiments, even though the shock speed was captured by observation of the shock-breakout time and knowledge of the sample thickness, the oxide layer present on the back surface of our samples and the use for some shots of parylene-N coated samples introduced a large uncertainty in the sample thickness determination which would have translated to an uncertainty in the shock speed. Typically, shock speed is precisely determined by using stepped thickness targets and/or impedance matched substrates [115-117]. In this way, the shock does not release into vacuum, which results in a backward propagating release wave in the sample. Interaction of this release wave with the incoming portion of the shock wave caused spallation, as seen in the "dip" of the velocity profile of the free standing Cu foils in Figure 6.3.

6.2 *In situ* Lattice Measurement of the Bcc Phase Boundary in Magnesium Along the Principal Hugoniot

The critical role of the pressure–induced *s* to *d* band electron transfer on the structural stability and physical properties, such as superconductivity, of transition metals has been studied extensively over the years [118-120]. Recently, high pressure structural sequences in 3rd period metals [121, 122] have also been elucidated when taking into account the lowering and filling under compression of the initially vacant *d*-band. The hcp to bcc phase transition in Mg is an example of such structural change attributed to a pressure-induced *d*-band population. A number of first principles calculations within the framework of density functional theory [123-126] have attempted to define the hcp-bcc phase boundary in Mg, however with great discrepancies. These discrepancies are generally attributed to the extremely small enthalpy barrier between the hcp and bcc phases (~1.1 mRy at P=35 GPa and T=0 K).

In our study, we attempted to capture lattice evidence of the hcp to bcc phase transition in Mg on the principal Hugoniot, thus providing an evaluation of the various bcc phase boundary calculation methods in Mg. The reason behind choosing shock-loading to induce the phase transition was twofold: First, via shock-loading, the desired pressure (and temperature) regime for the hcp-bcc transition in Mg can be easily accessed and characterized with velocimetry. Second, the shock itself provides a fiducial for measuring time-dependent processes in the lattice, yielding important information on the kinetics of the phase transition during dynamic loading. In Mg, the proposed martensitic-type transformation [68, 69] implies that the kinetics should be extremely fast (<ps).

Therefore, a large volume of material should transform within the nanosecond timescales of our pump-probe experiment.

6.2.1 EXPERIMENT DESCRIPTION

The experiment was performed at the JANUS two-beam, kJ-level laser utilizing the sample and x-ray source geometry of the cylindrical camera described in Chapter 5. The reason behind replacing the S-B camera for these measurements was that at the higher shock pressures needed to induce the phase transition in Mg, a large noise background was present originating mainly from the shock drive. To reduce such noise background it was beneficial to detect diffraction in transmission allowing the sample itself to act as a noise filter. In addition, a phase plate with a focal spot comparable to the size of the collimated x-ray source was used in the drive laser beam to provide a spatially uniform shock front. A diagram of the experimental setup is drawn in Figure 6.8.

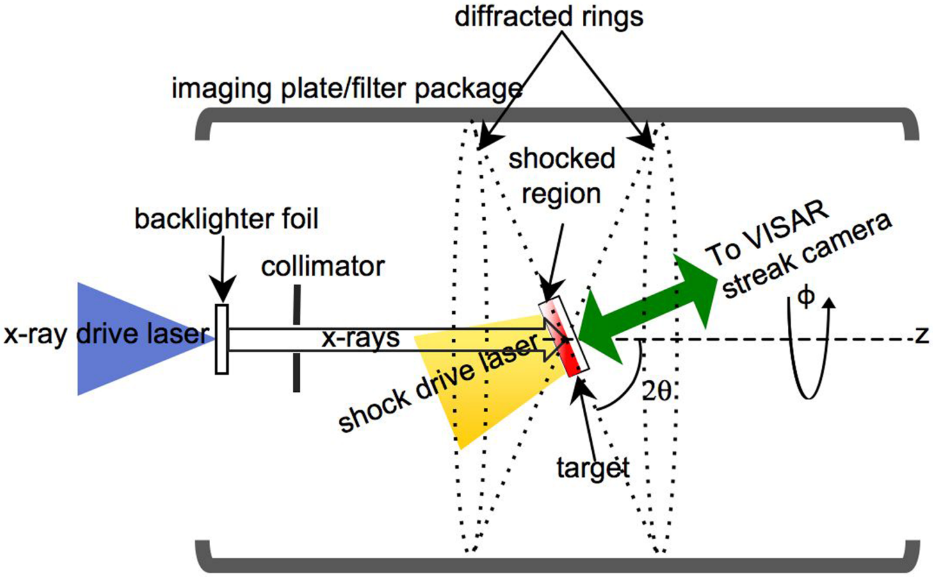
diffracted rings
imaging plate/filter package
shocked region
backlighter foil
collimator
To VISAR streak camera
ϕ
x-ray drive laser
x-rays
shock drive laser
z
2θ
target

Figure 6.8. (not to scale) Experimental geometry for laser driven shocks and dynamic x-ray diffraction studies in Mg using the CPPC camera.

A 4.7 keV, 3 ns, point x-ray source was generated by one of the 527 nm laser beams when incident on a 12 μm thick Ti foil with a peak intensity of ~4x10^{14} W/cm^2. Approximately 60% of the 4.7 keV line emission was transmitted through the Ti foil. The He$_\alpha$-like x-rays emitted over 4π sr from the thermal plasma were collimated by a series of pinholes to a ~2 mm diameter spot size on the target. The Debye-Scherrer diffraction rings from grains satisfying the Bragg condition $2d_{hkl}\sin\theta=\lambda$ were subsequently recorded on imaging plate detectors wrapped around the perimeter of the cylinder.

Samples of 50 μm thick, 99.98% pure rolled Mg foil coated with a 39 μm parylene-N/80 nm Al ablator layer were used in the experiments. The static texture of the samples was characterized with a continuous Cu K$_\alpha$ laboratory source prior to shock-loading. The texture and orientation of the samples relative to the collimated x-ray source resulted in certain Mg planes appearing exclusively in reflection ($(002)_{hcp}$ and $(102)_{hcp}$), or in transmission ($(100)_{hcp}$), or both ($(101)_{hcp}$) (Figure 6.9). All allowed diffraction planes (see Chapter 4, equation (4.22)) were captured. Texture did not compromise our measurements here as the cylindrical diffraction geometry was able to record full Debye-Scherrer rings. We also obtained a quantitative measurement of the Mg grain size (and orientation distribution) by imaging an area from the cross-section of an Mg foil with Dark Field-Transmission Electron Microscopy (DF-TEM) [127]. In this technique, an electron beam is incident on the specimen, in this case Mg that was cut and polished by a focused ion beam. The grains whose plane normals satisfy the diffraction condition with respect to the direction of the electron beam are “illuminated”. The DF-TEM image appears dark in the areas consisting of grains that do not diffract and bright in the areas of the grains that diffract (Figure 6.10). From the images obtained we deduced that the grains in the Mg foil were <3 μm and that there was no strong orientation preference.

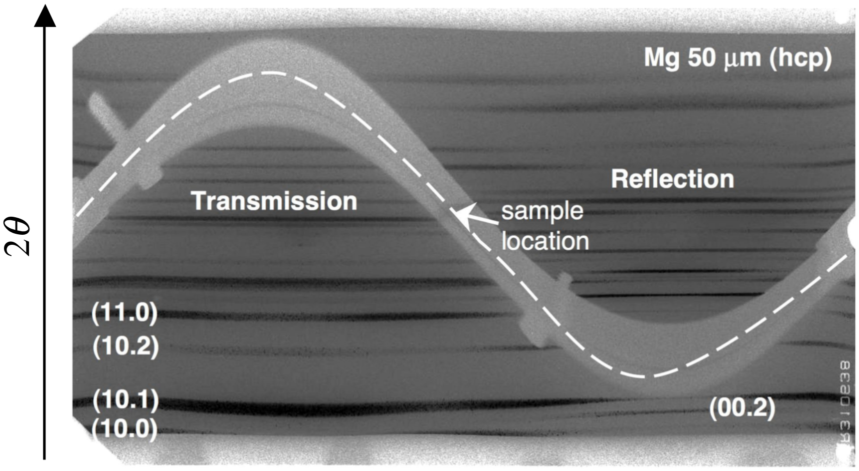

Figure 6.9. Static diffraction data from a 50 μm thick rolled Mg foil illuminated by a collimated laboratory Cu Kα source for a qualitative texture and grain size characterization.

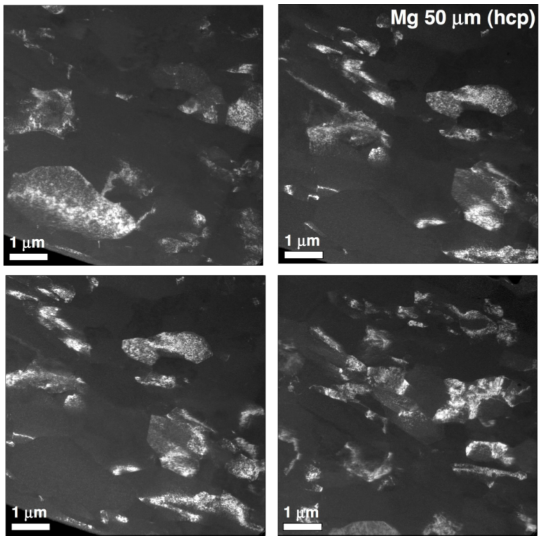

Figure 6.10. DF-TEM images from the cross-sectional area of a 50 μm Mg rolled foil captured at different k-vector orientations. The grains illuminated have dimensions no larger than ~3 μm.

Shocks were ablatively driven in the parylene-N coating of the samples using single 527 nm laser pulses with peak intensity between 4×10^{11}-1.5×10^{12} W/cm^2 resulting in shock pressures in Mg between 12 and 45 GPa. A trapezoidal laser temporal profile with <500 ps rise time and 6 ns duration was chosen to provide a steady amplitude shock front at the ablator/Mg interface (Figure 6.11) [74, 128]. To ensure spatially uniform shock-loading over a 1 mm^2 area, we placed the sample front surface at the focus of a KPP phase plate. The shock propagation behavior in the sample was confirmed by 1D Lagrangian hydrodynamics simulations, which are presented in detail in Chapter 7.

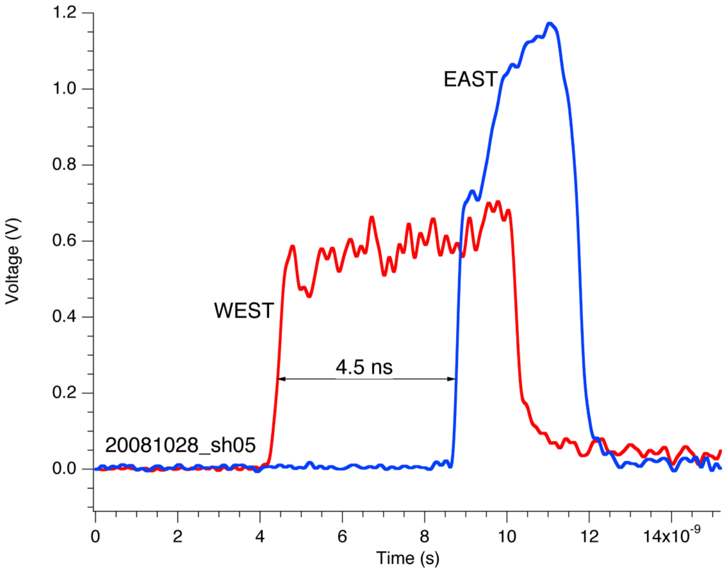

Figure 6.11. An example of laser waveforms used in the shock-compression experiments of polycrystalline Mg. For this data shot, the EAST (x-ray backlighting) delivered 338 J, 3ns, and the WEST (shock drive) 83 J, 6 ns. The leading edge of the EAST was delayed by 4.5 ns with respect to the leading edge of the WEST pulse.

Two-channel line-imaging Doppler velocimetry was implemented to verify the Hugoniot end state pressure and material response via measurement of the sample's rear free surface velocity upon shock breakout. Because of the free surface velocity range of our shock pressure scan (1.5-6 km/s), etalons with fringe constants from 0.993 km/s/fringe to 10.677 km/s/fringe were used inside the VISAR interferometers.

6.2.2 RESULTS FROM X-RAY DIFFRACTION AND VELOCIMETRY

Single shot diffraction data integrated over the x-ray pulse duration were recorded in the transmitted and reflected direction from the sample. The sample thickness probed corresponded approximately to the attenuation length of the 4.7 keV x-rays incident on Mg at 45° with respect to the sample surface, namely 22 μm. A static reference signal was captured on every shot by timing the x-ray pulse to start ~1 ns before the arrival of the shock front at the ablator/Mg interface. An example of diffraction signal is shown in Figure 6.12 for a shock pressure of 12.7±0.5 GPa. The static hcp planes are overlaid by dashed lines, whereas the signal from the compressed hcp planes is depicted by dash-dotted lines. Note that the difference in the noise background between the transmitted and reflected directions was found to scale by a factor of ~1/2.

For shock pressures below 26 GPa, compression of the hcp (100), (002), (101) and (102) planes was evident in the diffraction images as additional lines parallel to the static reference lines at a higher Bragg angle 2θ. Gaussian profiles were fitted by least squares optimization to the line profiles extracted from the imaging plate detectors. Lattice compression for each (*hkl*) plane was calculated from the shift in 2θ measured relative to the corresponding un-shocked diffraction peak for every shot. In the data shown here, the (100) was compressed by 7.3%, the (002) by 6.8%, the (101) by 7.4% and the (102) by 6.8%. Within the uncertainty of our measurement (~0.2%), the observed lattice strains along different orientations were approximately equal implying hydrodynamic compression.

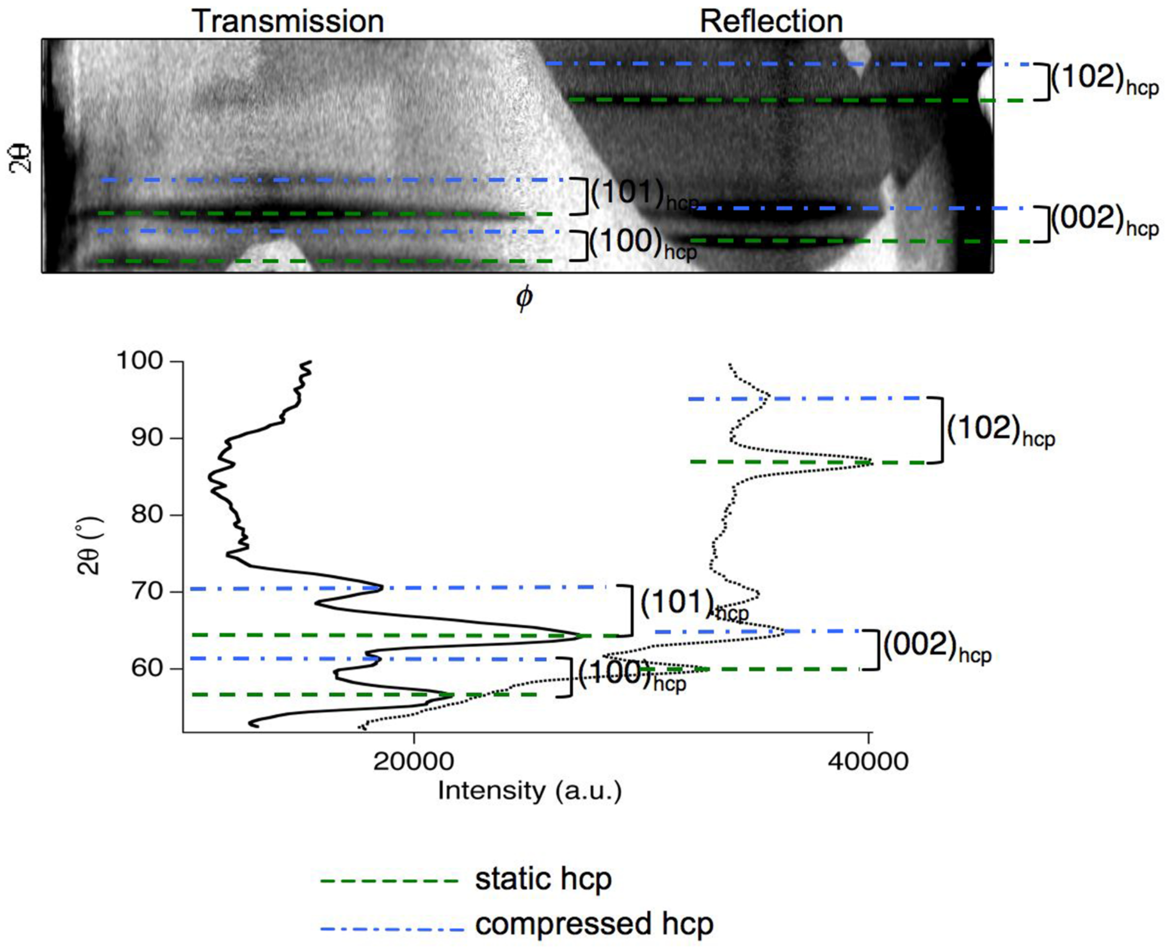

Figure 6.12. Diffraction data and line profiles taken at 12.7±0.5 GPa displaying static and compressed diffraction signal from the Mg (100), (101), (002), and (102) hcp planes.

Our compression measurements below 26 GPa in which good diffraction and velocimetry data were acquired on a single shot basis are summarized in the table below.

Table 6.1 % compression of the lattice planes diffracting in transmission (T) and in reflection (R) as a function of shock pressure, where P<26 GPa.

Pressure (GPa)	(100) T	(002) R	(101) T	(102) R
7.8±0.7	–	–	4.8	–
8.4±0.7	5.7	–	5.7	–
12.7±0.5	7.3	6.8	7.4	6.8
16.6±0.9	–	9.3	9.2	9.0
17.5±1.0	–	–	8.4 (?)	–
19.4±0.8	–	–	9.6	–
20.7±1.2	–	–	9.2 (?)	–
22.2±0.6	–	–	9.8	–
23.2±1.0	–	–	10.5	–

For shock pressures above 26 GPa, the number of diffraction lines from shock-compressed planes decreased, as shown in Figure 6.13. Apart from the static reference lines, only a single diffraction line was observed from the shocked state in both the transmitted and reflected orientations. To interpret this line as either a compressed hcp or bcc phase, the measured material density assuming either phase was compared against the Mg shock Hugoniot. In the paragraphs that follow, the essential steps in obtaining density from the diffraction peak shifts are explained as they will eventually lead to an understanding on how the bcc phase was identified from our data. Note that lattice compression measurements from only the (101) hcp plane were available throughout our pressure range. The diffraction peak from the (100) plane above 13.0 GPa merged with the static (101) plane and could not be resolved. The compressed (002) and (102) diffraction peaks suffered from low signal to noise being detected on the side of the shock drive. For this reason, for pressures greater than 18 GPa, it was very difficult to obtain a reliable measurement of their position.

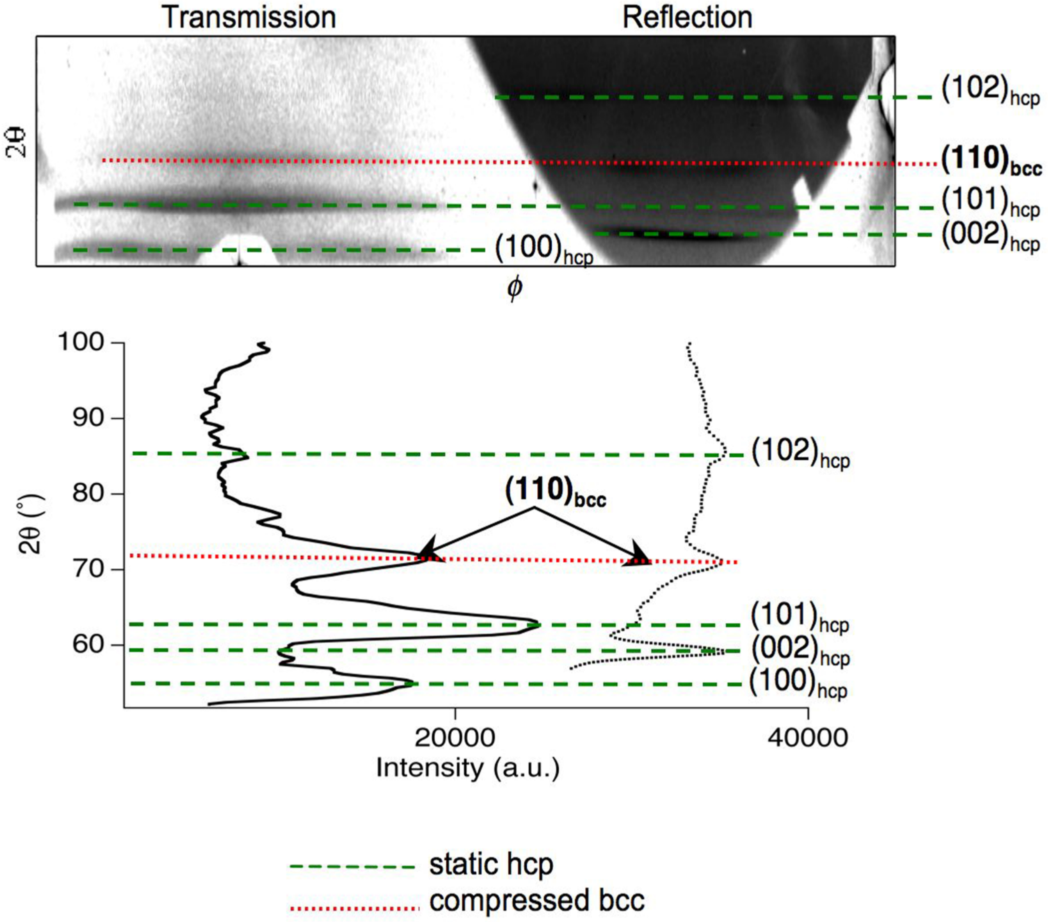

Figure 6.13. Diffraction data and line profiles taken at 44.5±1.1 GPa indicating signal from the compressed Mg bcc phase .

To obtain Mg density from the interplanar spacing measured via x-ray diffraction, we assumed an isotropically compressed end state. This assumption was supported in our diffraction measurements by the absence of significant strength effects that would have been exhibited as a variation in the measured lattice strain along the azimuthal direction ϕ. In other words, if strength effects were present we would have measured a variation in the $\Delta 2\theta = 2\theta - 2\theta_0$ along the length of the imaging plate detector for each diffracting plane. (Diffraction rings, in the presence of strength, take an elliptical form. In our experiments, such deviation in the shape of the diffraction rings due to strength was not observed.)

The density ratio between the compressed and the static state in the hcp phase was calculated, as before, from the expression $\frac{\rho}{\rho_0} = (\frac{d_0}{d})^3 = (\frac{\sin {2\theta}/{2}}{\sin {2\theta_0}/{2}})^3$. For the bcc phase, a calculation of the expected diffraction angle 2θ as a function of the density ratio proceeded in the following way. First, from the definition of density, ρ in the bcc phase is given by

$$\rho = \frac{2}{a^3}\frac{M_{Mg}}{N_A} \tag{6.2}$$

where a the lattice constant, N_A=Avogadro's number=$6.022\text{x}10^{23}$ and M_{Mg}=24g/mol^{-1} the atomic mass of Mg. The factor 2 comes from the presence of two atoms in the bcc unit cell. The lattice constant a can thus be expressed as

$$a = \left(\frac{2M_{Mg}}{N_A \cdot \rho_0}\right)^{1/3}\left(\frac{\rho_0}{\rho}\right)^{1/3} \tag{6.3}$$

where ρ and ρ_0 the compressed and uncompressed density in the bcc phase of Mg. Since the interplanar distance d_{bcc} in the bcc phase and the lattice constant a are related by

$$d_{bcc} = \frac{a}{\sqrt{h^2 + k^2 + l^2}} \,, \tag{6.4}$$

where h, k, l, the Miller indices of a plane, d_{bcc} can be re-written in terms of the density ratio of the compressed and un-compressed bcc phase as

$$d_{bcc} = \frac{\left(\dfrac{2M_{Mg}}{N_A \cdot \rho_0}\right)^{1/3}}{\sqrt{h^2 + k^2 + l^2}} \cdot \left(\frac{\rho}{\rho_0}\right)^{-1/3} . \tag{6.5}$$

Here the density ρ_0 was taken as equal to that of ambient density Mg namely 1.738 g/cm^3. Combining Bragg's law $2d_{hkl}\sin\theta = \lambda$ with the assumption of isotropic compression and equation (6.5), the 2θ angle of diffracting bcc planes becomes

$$2\theta = 2\sin^{-1}\left(\frac{\lambda\sqrt{h^2 + k^2 + l^2}}{2\left(\dfrac{2M_{Mg}}{N_A \cdot \rho_0}\right)^{1/3}}\right) \cdot \left(\frac{\rho}{\rho_0}\right)^{1/3} . \tag{6.6}$$

The diffraction angle 2θ for a number of hcp and bcc planes in Mg is plotted as a function of the density ratio for a 4.75 keV x-ray backlighter in Figure 6.14. The same plot was generated using 6.7 keV x-rays to illustrate the effect of a higher energy x-ray backlighter in the placement of the diffraction lines (Figure 6.15). As it is observed from the plots, using a 6.7 keV (Fe) backlighter would have resulted in diffraction peaks positioned too closely to be resolved. Especially, the $(110)_{bcc}$ plane would have diffracted extremely closely to the $(101)_{hcp}$ and the $(002)_{hcp}$ making its identification quite difficult.

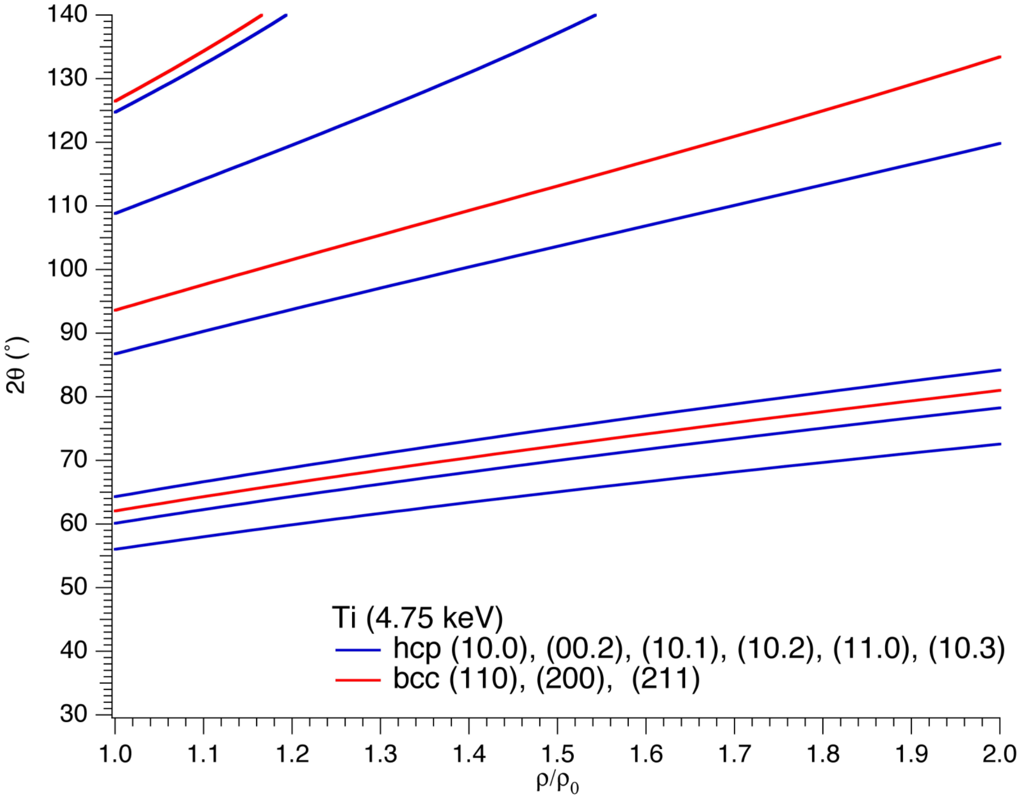

Figure 6.14. Plot of diffraction angle 2*θ* vs. compressed to static density ratio for the hcp and bcc lattices of Mg probed by a 4.75 keV x-ray source.

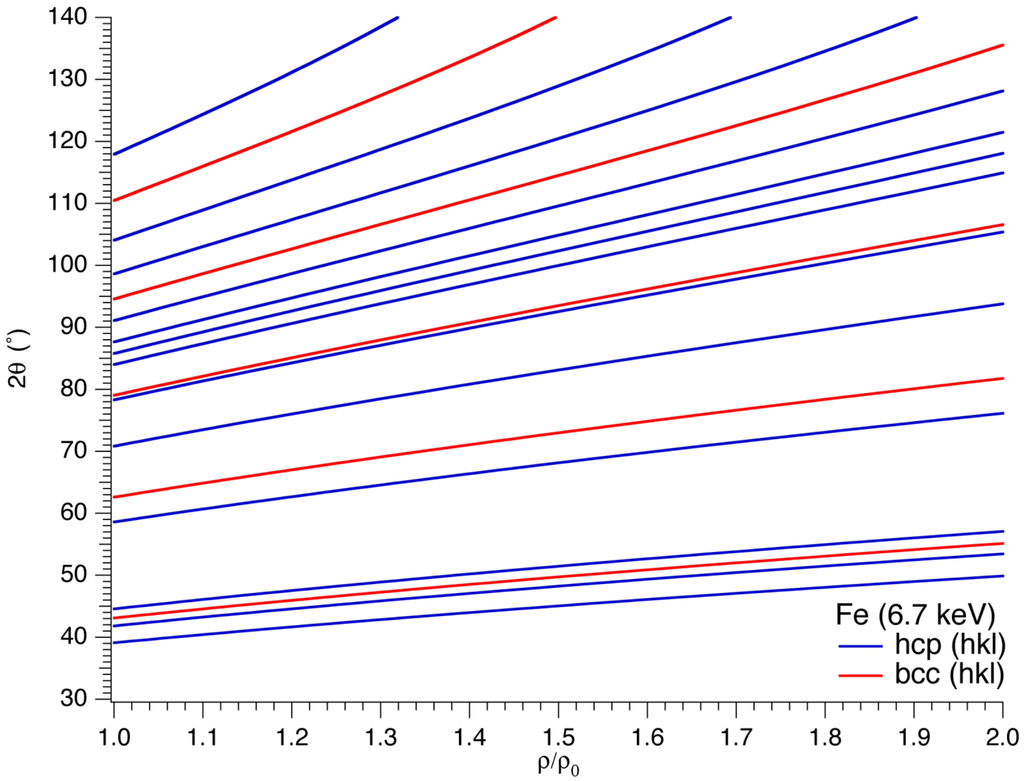

Figure 6.15. Plot of diffraction angle 2θ vs. compressed to static density ratio for the hcp and bcc lattices of Mg probed by a 6.7 keV x-ray source.

We performed two-channel line-imaging velocimetry for an experimental characterization of our shock conditions. The shock pressure calibration provided by velocimetry was also crucial in identifying the single compressed peak captured for shock pressures above 26 GPa via the measured $P-\rho$ Hugoniot. The particle velocity profiles extracted ($U_p \approx \frac{1}{2}U_{fs}$) at 12.7 GPa and 44.5 GPa are shown in Figure 6.16. The velocity profile at 44.5 GPa exhibited no wave splitting, as expected, because of the small $\Delta V/V_0$ of <1% in the hcp to bcc transition in Mg. The interferometric data for this Hugoniot state is also shown (Figure 6.17).

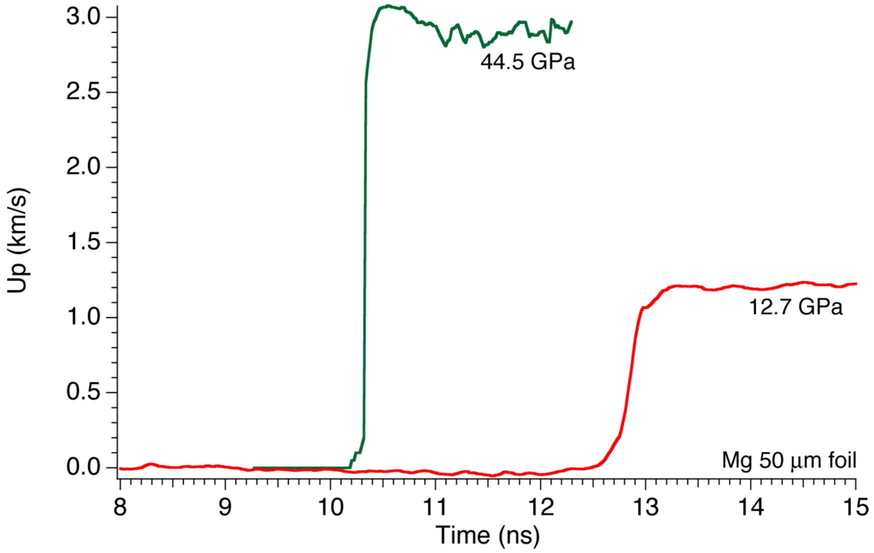

Figure 6.16. Particle velocity profiles extracted from VISAR interferograms after probing the free surface expansion of shock-compressed Mg foils. The peak particle velocity of the two records shown are 3.1 km/s and 1.2 km/s corresponding to a peak pressure of 44.5 GPa and 12.7 GPa respectively.

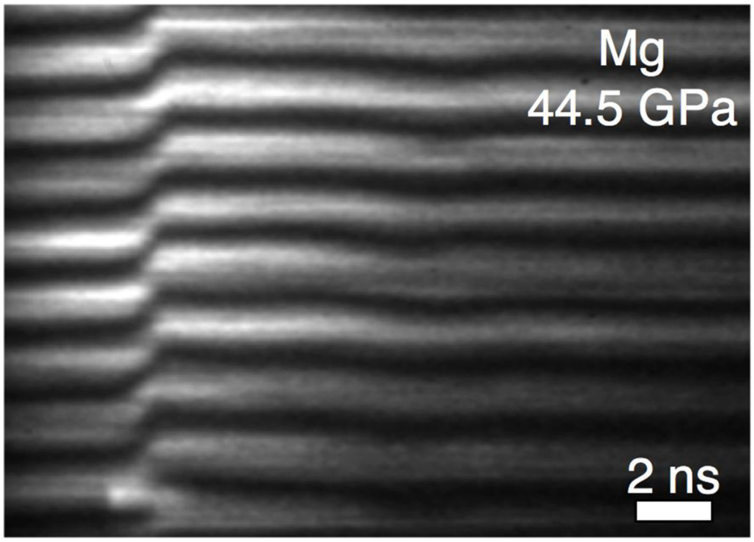

Figure 6.17. Example of a VISAR interferogram from Mg acquired at a pressure (44.5 GPa) above the phase transition. No shock-wave splitting is evident in the VISAR record as a result of the phase transition.

A summary of the compression values from the single compressed peak that appeared in diffraction above 26 GPa, assuming an hcp or a bcc lattice, is presented in the table below. Comparison of the % compression in the (101) hcp plane calculated below and above 26 GPa (Tables 6.1 and 6.2) shows a downward jump in compression from 10.5% at 23.2 GPa to 8.5 % at 26.2 GPa, which clearly indicates that the compressed peak observed above 26 GPa does not correspond to the hcp phase. If it did, the trend in increasing compression with pressure for the (101) hcp plane should have continued above 26 GPa. Instead for pressures exceeding 23.2 GPa the compression in the (101) hcp appeared to be <10.5 %. On the other hand, the hypothesis of a (110) bcc peak is in agreement with the expected trend of increasing % compression with pressure, having a % compression value of 11.3 % at 26.2 GPa. We now discuss a more rigorous method in proving that the observed diffraction peak belonged to the bcc (110) plane.

Table 6.2 % compression assuming diffraction from either (110) bcc or (101) hcp planes above 26 GPa. The uncertainty in compression is ~0.2%.

Pressure (GPa)	(110) bcc	(101) T
26.2±1.2	11.3	8.5
26.9±1.4	11.2	8.4
29.5±1.3	11.5	8.7
31.2±3.8	11.6	8.8
31.8±1.8	11.9	9.1
36.0±1.5	12.2	9.5
37.7±2.0	12.5	9.7
44.5±1.1	13.1	10.3

6.2.3 IDENTIFICATION OF THE BCC PHASE IN MG

In order to confirm the presence of a bcc phase in the shock-compressed Mg above 26 GPa, the pressure estimated by velocimetry and the compressed to static density ratio measured by nanosecond x-ray diffraction assuming isotropic compression was plotted (Figure 6.18).

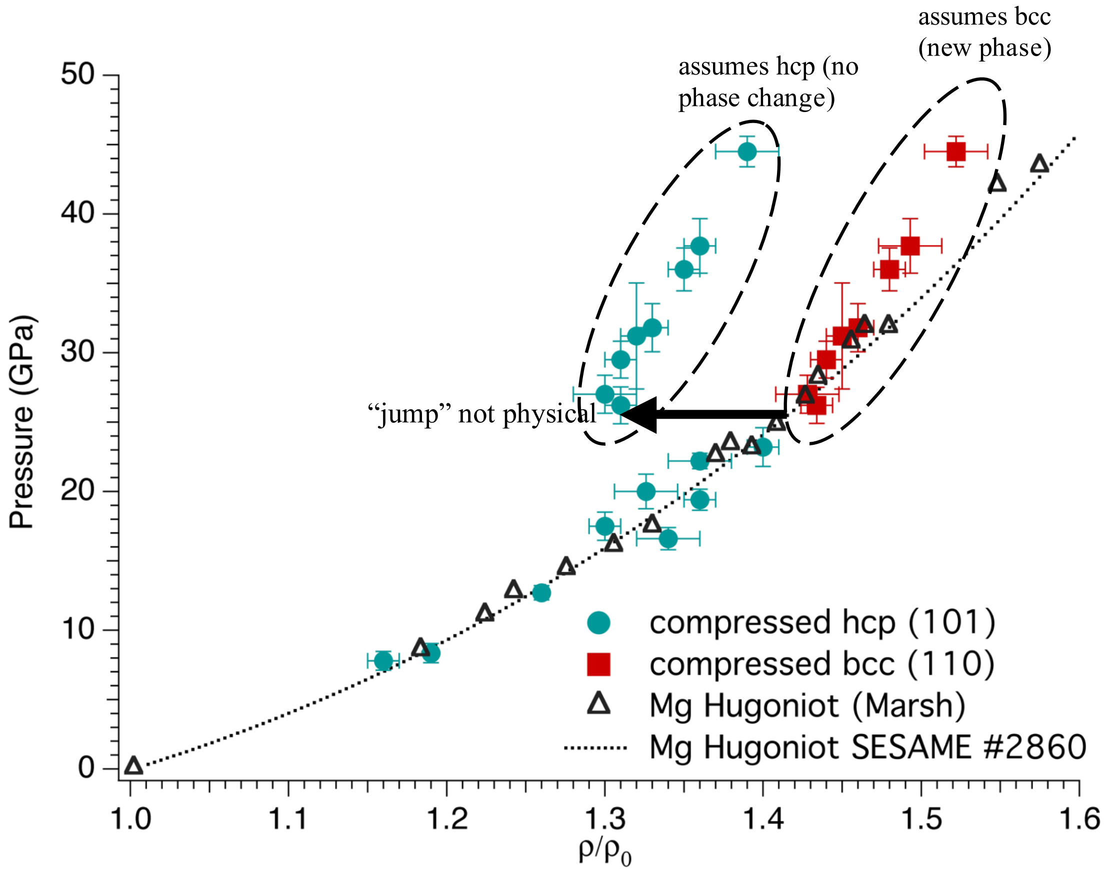

Figure 6.18. Plot of shock pressure against the material compressed to static density ratio. The principal Hugoniot from SESAME table #2860 and that measured by Marsh et al. are also shown. Above 26 GPa, a bcc interpretation of the data appeared to be consistent with the Mg shock Hugoniot and the small volumetric change of the hcp to bcc phase transition.

Below 26 GPa, the data were in good agreement with the shock Hugoniot. Significant strength effects, which would have caused a discrepancy between the density obtained from x-ray diffraction and the value predicted by the Mg EOS for a given pressure, were not evident. Above 26 GPa, the diffraction angle 2θ measured was assumed to originate from either an hcp or bcc compressed lattice as explained earlier. Calculation of a density ratio assuming diffraction from compressed (101) hcp planes resulted in a significant deviation from the Mg shock Hugoniot. A similar result was obtained assuming diffraction from compressed (002) hcp planes. In contrast, assignment of a density ratio from compressed (110) bcc planes overlaid our data points the closest to the Mg Hugoniot and in close proximity to the experimentally measured Hugoniot by Marsh et al. [129]. Since the expected hcp-bcc $\Delta V/V_0$ of <1% corresponds to a lattice distortion with an imperceptible discontinuity in the pressure-volume plot, we deduced that the new diffraction peak observed above a shock pressure of 26 GPa belonged to compressed (110) bcc planes. Thus, from the data shown in (Figure 6.13) at 44.5±1.1 GPa, the lattice strain in the (110) bcc plane was measured to be 13.1% in transmission and 12.3% in reflection resulting in a material density ratio of 1.52 and 1.49 respectively.

Measurement of a compressed bcc phase on the principal Hugoniot was verified above P=26.2±1.3 GPa. The uniformity of the new line representing the compressed (110) bcc suggested no significant texture in the new phase. This could be attributed to an original hcp phase texture that was favorable towards the atomic re-arrangement mechanism, as well as a highly degenerate transition pathway. The proposed hcp to bcc transition mechanism in Mg consisting of a shuffling of planes such that the (100) hcp coincides with the (110) bcc has a twelve-fold degeneracy due to the rotational symmetry of the hexagonal structure [130]. A schematic of this mechanism was presented earlier in Figure 3.7. Furthermore, the intensity of the new (110) bcc relative to the compressed hcp lines is in agreement with Olijnk's [131] DAC diffraction data above the transition pressure. Specifically Olijnyk reported a strong decrease in the intensity of the compressed hcp peaks upon appearance of the (110) bcc signal, similar to our observed diffraction intensity above 26 GPa, which would support a fast transformation from the hcp to the bcc phase in the bulk of the material. Such timescale (<1 ps) is characteristic of martensitic transformations, i.e. the hcp to bcc. In addition, the low scattering intensity observed by Olijnyk in bcc planes other than (110) bcc supports the absence of additional bcc diffraction peaks in our experiments due to the limited signal to noise ratio of our technique. A dhcp phase claimed by Errandonea [132] in the low pressure-high temperature region of the Mg phase diagram could not be verified by our measurements; a diffraction geometry with improved angular resolution [133] would have been required for the detection of such small structural change from the original hcp phase.

6.2.4 COMPARISON BETWEEN *AB INITIO* BCC BOUNDARY CALCULATIONS AND EXPERIMENTS IN MG

In this study, shock-loading to end states on the principal Hugoniot provided access to a P-T region in the Mg phase diagram where calculated bcc phase boundaries vary significantly. In this way, we were able to assess the performance of different first principles electronic structure calculation methods within the framework of the density functional theory, unlike data previously obtained at 300 K where phase boundary predictions overlap closely. Figure 6.19 shows the calculated bcc phase boundaries in Mg together with the locus of end states that we probed on the principal Hugoniot. The principal Hugoniot intersects the bcc general gradient approximation (GGA) boundary at P=32 GPa, T=1270 K, the local density approximation (LDA) bcc boundary at P= 30

GPa, T=1155K [134] and the LDA-GPT (generalized pseudopotential theory) bcc boundary at P=27 GPa, T=1020 K [59].

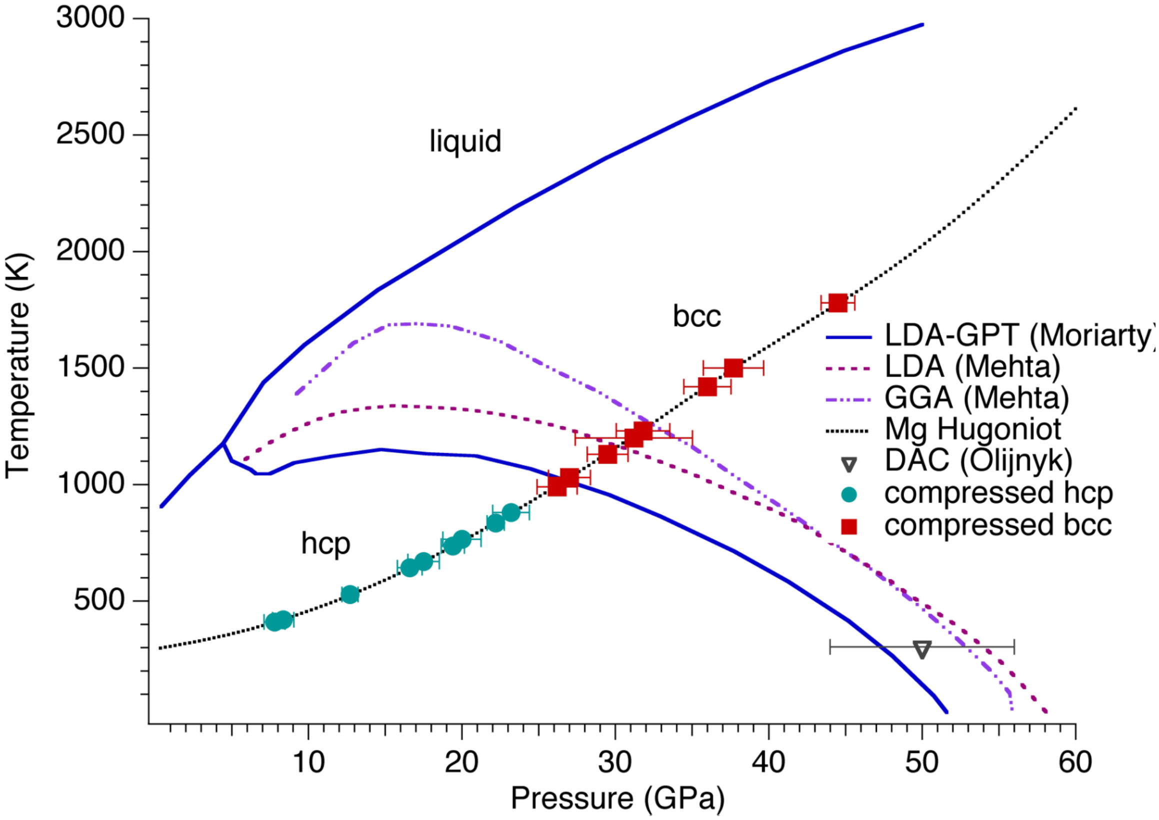

Figure 6.19. The calculated P-T phase diagram of Mg from various *ab initio* methods including the experimental points obtained in this study and by Olijnyk et al. The bcc phase measured above 26 GPa agrees well with the phase boundary calculated from generalized pseudopotential theory.

Our lattice measurement of a bcc phase above 26 GPa closely agrees with the LDA-GPT approximation. Thus, the lower pressure predicted for the bcc phase boundary by the LDA-GPT method is consistent with our experimental observation. In order to verify the bcc phase boundary in Mg along more than one P-T points, an experiment with samples pre-heated at a range of temperatures would have been necessary. Specifically, the material response close to the triple point would have been an interesting area to investigate. Not only this is the region with the greatest variation in the boundary location amongst various density functional theory calculations, but it is also the region of a well-debated dhcp (possibly metastable) phase. This dhcp phase has not been predicted before by any of the models discussed here and the DAC experimental results by Errandonea et al. [132] have not been confirmed so far by other experiments. To obtain a measurement from such phase (if it actually exists) an instrument with better angular resolution than that of our CPPC camera would be needed.

A brief introduction to the *ab initio* calculations within the framework of density functional theory (DFT) is now presented in order to gain a high-level understanding of the methods used to predict the bcc phase boundary in Mg. An excellent primer on DFT can be found in references [135, 136].

Density functional theory

Predictions of the properties of materials stemming from interactions between the electrons and nuclei, require a solution of the Schrödinger equation for the *N*-electron system in question. However, Schrödinger's equation is rarely solvable analytically, even in the approximation of stationary ions expressed by

$$\hat{H}\Psi = \left\{ -\frac{\hbar^2}{2m_e}\sum_{l=1}^{N}\nabla_l^2 + \sum_{l=1}^{N} V_{ion}(\vec{r}_l) + \sum_{l<l'} \frac{e^2}{\left|\vec{r}_l - \vec{r}_{l'}\right|} \right\}\Psi = \mathrm{E}\Psi \ , \tag{6.7}$$

where $\hat{H}$ the Hamiltonian composed by an electron kinetic energy term, an ionic potential energy term, and the Coulombic interaction potential for the N electrons, Ψ is the N-electron wavefunction and E the total energy of the system in its ground state.

Because of the immense computational effort required to solve the Schrödinger equation for the large number of electrons required to represent the unit cell in most solids of interest, a number of numerical approaches have been developed for electronic structure calculations. To the problem, Hohenberg and Kohn [124] re-casted Schrödinger's equation from 3N spatial coordinates to only 3 spatial coordinates by introducing functionals of the electron density $n(\vec{r})$. More specifically, by realizing that the electron density $n(\vec{r})$ encapsulates all the information of the N-electron wavefunction since

$$n(\vec{r}) = N\int d\vec{r}_1 .. d\vec{r}_N \Psi^*(\vec{r}_1 .. \vec{r}_N)\delta(\vec{r}-\vec{r}_1)\Psi(\vec{r}_1 .. \vec{r}_N)\,, \tag{6.8}$$

Hohenberg and Kohn constructed a ground-state energy E functional of the form

$$E[n] = T[n] + V_{ion}[n] + V_{ee}[n] \tag{6.9}$$

where T the electron kinetic energy, V_{ion} the ionic potential and V_{ee} the electron-electron potential all expressed as functions of the density $n(\vec{r})$. Thus, density functional theory was introduced in electronic structure calculations in which the only constraint for minimizing the ground state E was

$$\int n(\vec{r})d\vec{r} = N \ . \tag{6.10}$$

By expressing the ionic potential functional in *E*[n] as

$$V_{ion}\left[n\right] = \int V_{ion}(\vec{r})n(\vec{r})d\vec{r} \tag{6.11}$$

one needed to find a functional that represented the sum of the electron kinetic and potential energy. In other words, the exchange-correlation contribution to the Hamiltonian (in a functional form) could be isolated completely from the ionic or any other external potential.

A number of approximate forms of the electronic energy functional have been constructed and later compared with experimental data. The approximations considered here in the calculation of the Mg bcc boundary resulted from the Kohn and Sham formulation [125] in which the *N*-electron wavefunction Ψ is replaced with a single electron wavenefunction $\psi_l(\vec{r})$ resulting in an electron density distribution given by

$$n(\vec{r}) = \sum_{l=1}^{N} \left| \psi_l(\vec{r}) \right|^2 \ . \tag{6.12}$$

In this case, the many-body Schrödinger equation is also modified to solve for single electron wavefunctions, and has the form

$$\left\{-\frac{\hbar^2}{2m_e}\nabla^2 + V_{ion}(\vec{r}) + \int \frac{e^2 n(\vec{r}')}{|\vec{r}-\vec{r}'|} d\vec{r}' + \frac{\delta E_{xc}[n(\vec{r}')]}{\delta n(\vec{r}')}\right\}\psi_l(\vec{r}) = E_l \psi_l(\vec{r}) \qquad (6.13)$$

where $E_{xc}[n(\vec{r})]$ the exchange-correlation energy functional of the free electron gas whose density is assumed to be uniform. A simple illustration of the classic Schrödinger picture versus the Kohn-Sham DFT formulation is shown below (Figure 6.20). The complicated problem of interacting electrons in an external potential is simplified to non-interacting particles in the "effective" potential of the Hamiltonian in equation (6.13).

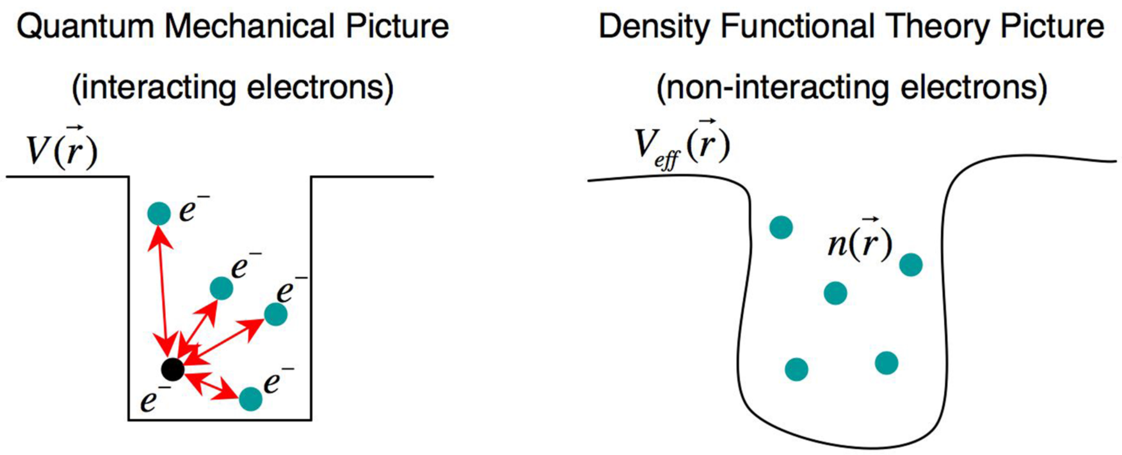

Quantum Mechanical Picture (interacting electrons)

Density Functional Theory Picture (non-interacting electrons)

Figure 6.20. A comparison between the classic quantum mechanical view of electrons interacting in a potential and the density functional theory view of non-interacting electrons (Kohn-Sham) in an effective potential. Agreement between the actual and effective potentials depends on the form of the exchange correlation functional.

A number of approximate forms of the exchange-correlation functional $E_{xc}[n(\vec{r})]$ exist. For example, in the local density approximation (LDA) $E_{xc}[n(\vec{r})]$ becomes

$$E_{xc}[n] = \int \varepsilon_{xc}[n]\, n(\vec{r})d\vec{r} \quad \text{(LDA)} \tag{6.14}$$

namely it depends only on the electron density at the spatial coordinate where the functional is evaluated. On the other hand, in the general gradient approximation (GGA) the gradient of density at the specific spatial coordinate and electron spin is considered

$$E_{xc}[n_\uparrow, n_\downarrow] = \int \varepsilon_{xc}[n_\uparrow, n_\downarrow, \nabla n_\uparrow, \nabla n_\downarrow]\, n(\vec{r})d\vec{r} \quad \text{(GGA)}\,. \tag{6.15}$$

Last, after observing that material properties are mostly influenced by the behavior of the valence electrons in the atoms, a further simplification of *ab initio* electronic structure calculations was implemented via the application of pseudopotentials [126, 137, 138]. Pseudopotentials effectively replace the explicit treatment of core electrons with an effective core potential. However, the caveat for such simplification is that if the pseudopotential is inaccurate then the electronic structure calculation will be too, potentially affecting any EOS prediction. Phase boundaries depend on small differences between large ground state energies and therefore, are particularly sensitive to inaccuracies in electronic structure calculations. As an example, Moriarty showed that Mg should remain in its original hcp phase at densities up to ten times its ambient density when the *d*-band population was omitted [122].

In general, for Mg, a number of first principles calculations within the framework of density functional theory have attempted to define the hcp-bcc phase boundary taking advantage of Mg's simple atomic arrangement and nearly-free electron properties up to pressures of ~100 GPa [59, 122, 134, 139, 140]. In this work, our experimental data were compared with bcc boundary calculations within the LDA, GGA, and LDA-GPT frameworks. Amongst these *ab initio* studies the location of the hcp-bcc phase boundary in Mg was predicted with a variation of ~5 GPa at room temperature, to >8 GPa for T>500 K because of the small free energy difference between the competing crystal structures. We found our results consisted with Moriarty's pseudopotential (GPT) treatment at the location of the principal Hugoniot. More details on the forms of the exchange correlation potentials used in these calculations can be found in their respective references.

6.3 Shock-Induced Melt Studies Using Dynamic X-ray Diffraction

6.3.1 DEMONSTRATION OF SINGLE SHOT NANOSECOND X-RAY DIFFRACTION FROM AN AMORPHOUS MATERIAL

The capability of determining the atomic distribution in an amorphous material is extremely important in shock-induced phase transition studies such as solid-melt, where the crystalline structure may be completely or partially lost. In general, x-ray diffraction studies of amorphous materials and materials undergoing shock-induced melt require a detection geometry with sufficient signal-to-noise ratio and angular range 2θ to capture the broad peaks associated with the scattering function S(q) as explained in Chapter 5. The high signal amplitude and wide angular range of the S-B camera could therefore prove to be important for such experiments.

We performed static diffraction from an amorphous metal foil MetGlas® [$Ni_{55}Fe_{27}Co_{15}Si_{1.6}Al_{1.4}$] as a proof of principle for amorphous signal detection in the S-B camera, a camera specifically designed with an angular detection range suitable for melt studies. A laser-produced 6.7 keV, 4 ns, x-ray source was used to probe the amorphous material. These results are presented below (Figure 6.21).

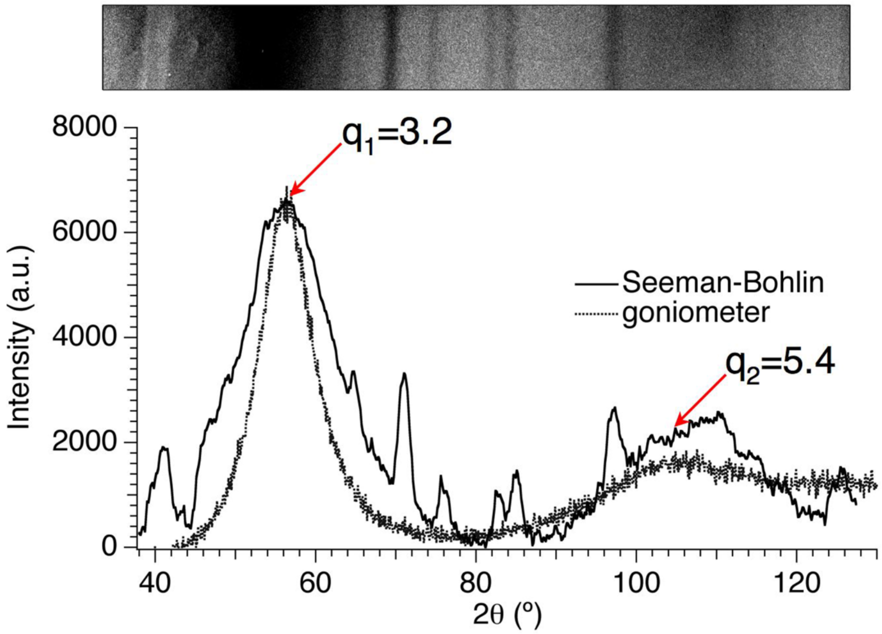

Figure 6.21. Diffraction data from MetGlas® with a 6.7 keV, 4 ns x-ray source. Broad peaks at q=3.2 and 5.4 are evident and are in good agreement with peaks measured with a continuous x-ray source. The sharp lines present originated from un-shielded camera edges.

We detected the first two peaks of the scattering function S(*q*) from Metglas® at q_1=3.2 and q_2=5.4. This result was in good agreement with scattering measurements from MetGlas® performed with a laboratory Cu Kα source coupled to a Philips vertical goniometer. The exhibited sharp peaks were attributed to diffraction occurring from the Al camera fixture. They were subsequently eliminated using appropriate shielding.

Having demonstrated diffraction from an amorphous solid we also attempted diffraction from a static liquid. Gallium was chosen since it melts at T=303 K. Ga pieces were packaged inside two layers of 100 μm thick black Kapton, a plastic material used in all diffraction experiments for mounting our targets on the diffraction camera target holder. We heated this Ga/Kapton assembly above the melting point of Ga with a radiative heat source (fiber lamp) and then performed in vacuum x-ray diffraction with the same x-ray source as for Metglas. No diffracted signal from the liquid Ga was observed. We deduced that for this experiment to succeed, a vacuum-sealed cell with liquid Ga had to be prepared in order to probe a liquid layer of uniform thickness. Even though Ga has a very low vapor pressure (4.7×10^{-3} mTorr at 456 K), its vapor pressure was comparable to our vacuum conditions ($\sim 3 \times 10^{-3}$ mTorr), so most of the liquid Ga sample prepared must have evaporated during evacuation of the target chamber.

6.3.2 DETERMINATION OF THE SOLID-LIQUID BOUNDARY IN SHOCKED BISMUTH

Motivated by a desire to understand the dynamics of phase transitions in high Z materials with complex phase diagrams, an experimental campaign was proposed at the start of this PhD work that involved studying the solid-liquid boundary in shocked Bi. Bismuth has been an attractive material for shock induced transformation studies for a variety of reasons: a low pressure (< 5 GPa) is required to drive pre-heated Bi samples into the solid-liquid phase boundary and, interestingly, the negative slope of the solid-liquid boundary at low pressure yields re-solidification of the material upon isentropic release from the shocked liquid state (Figure 6.22).

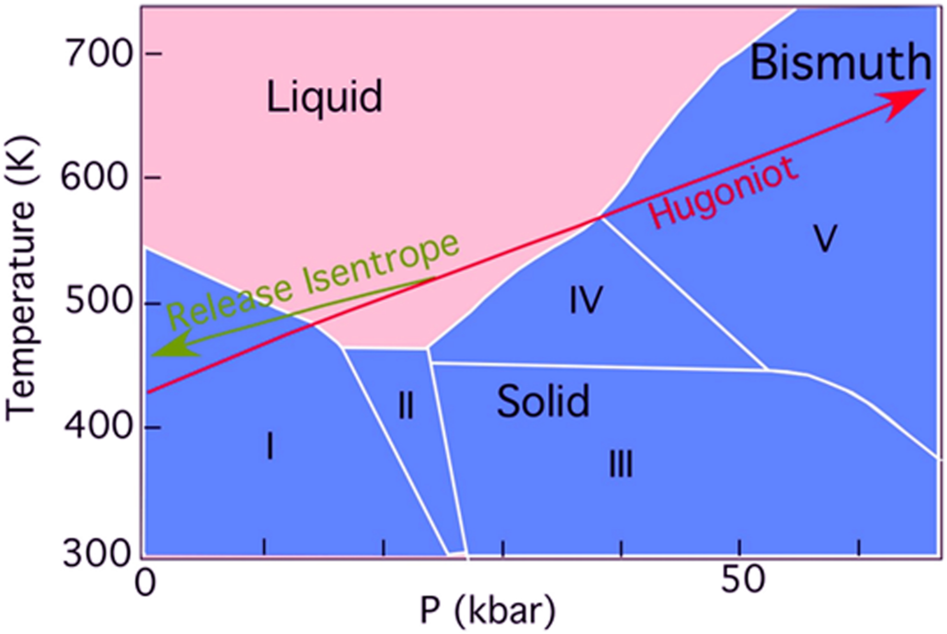

Figure 6.22. The phase diagram of Bi, depicting the shock Hugoniot from T=425 K and the isentropic release path from a shocked liquid state.

However, the unknown phase transition kinetics of Bi have historically posed a great challenge in capturing the solid to liquid phase transition. The two extreme cases that have been postulated are the following: 1) if the melt transition takes place at an infinite rate (shock duration>phase transition time) a three-wave structure should be evident in the shock pressure as indicated by calculations utilizing a multiphase Bi EOS, or 2) if the melt transition has a finite rate (shock duration< phase transition time) a two-wave structure should appear corresponding to a transition between the Bi I phase and a metastable Bi II compressed phase (Figure 6.23). In the former case, the three-wave structure would result from a) intersection of the shock Hugoniot with the liquid phase boundary, b) further compression upon isentropic flow along the phase boundary to the triple point (negative slope) and c) a second shock wave compressing the material to the driving stress. In the case of slow melt kinetics, the phase boundary of the metastable Bi

II phase would extend into the liquid phase of Bi resulting in a solid Bi I-solid Bi II phase transition.

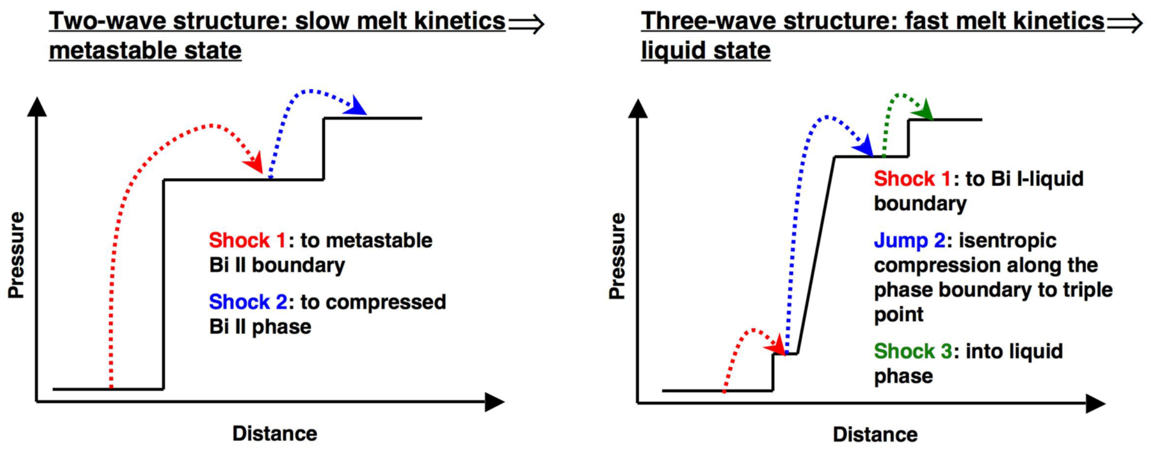
Two-wave structure: slow melt kinetics⟹ metastable state
Pressure
Distance
Shock 1: to metastable Bi II boundary
Shock 2: to compressed Bi II phase
Three-wave structure: fast melt kinetics⟹ liquid state
Pressure
Distance
Shock 1: to Bi I-liquid boundary
Jump 2: isentropic compression along the phase boundary to triple point
Shock 3: into liquid phase

Figure 6.23. The effect of the melt kinetics in Bi on the stability of the shock wave is shown. Two and three wave structures are possible depending on whether the phase transition timescale is slower or faster than the shock-loading conditions respectively.

There have been a number of experimental studies in Bi employing loading scales ranging from several μs to tens of ns [50-54, 141-146]. These experiments have predominantly relied upon features in the shock wave profile to predict the phase transition pathway. In early experiments by Johnson, Asay and others, neither of the two kinetic extremes explained earlier was evident in the wave profile data. It was concluded that most likely the measured end state was that of the triple point which implied the presence of a mixed solid/liquid phase. More recently, Smith et al. [66, 147] employed ramp compression (isentropic loading) over 35 ns of pre-heated Bi samples. During these ramp compression tests, a velocity plateau was observed after the expected phase transition point. By entering the know strain rate $\dot{\varepsilon}$ of the experiment into an Arrhenius type equation where $\ln(\dot{\varepsilon}) \propto \Delta P / kT$, an estimate of the thermally activated energy barrier was allowed. Comparison with simulations predicting the energy barrier for each type of phase transition (solid-solid or solid-liquid) enabled an identification of the phase transition and thus, a timescale measurement from the temporal width of the plateau observed in the velocimetry profile. However, to this date there has been no time-resolved lattice measurement of the phase transition mechanisms in Bi.

We proposed to investigate the dynamics and kinetics of phase transitions in shock-loaded Bi via nanosecond x-ray diffraction and velocimetry. We suggested focusing primarily on inducing a solid-melt transition in the low-pressure region (20-50 kbar) by pre-heating samples of polycrystalline Bi. This investigation would have taken place in the S-B diffraction camera described in Chapter 5, utilizing its conductive heating capability, developed specifically for Bi experiments. Unfortunately, no facility time was ever allocated for this effort. However, by tagging along various other experiments, preliminary data was taken on both static and shocked Bi samples (at room temperature) which led into valuable insights on how a successful diffraction experiment in Bi could be performed in the future.

An example of preliminary static data from polycrystalline Bi is shown in (Figure 6.24). The greatest challenge in performing x-ray diffraction from Bi was the restrictions in sample thickness and the noise increase due to fluorescence as a result of Bi's high Z (Z_{Bi}=83). Both of these issues are interconnected as fluorescence could in principle be attenuated by the sample itself via the choice of a diffraction geometry detecting diffraction peaks in transmission (e.g. CPPC). However, the extremely low attenuation length of Bi (~2 μm at 8 keV) would require very thin samples which would imply very short shock-loading time scales in order to avoid release waves interacting with the shock front. Therefore, a study of the kinetics in shock-melted Bi would have been extremely difficult in transmission. If the signal-to-noise in the reflected direction was adequate to perform shocked studies, samples of thickness> 100 μm would have been required to support shock-loading of >20 ns. From preliminary data shots with a shock drive, we found that a shocked state in Bi could not be observed because of the poor signal to noise. Our suggestions for a diffraction study in shocked-Bi will be discussed in the Conclusions Chapter.

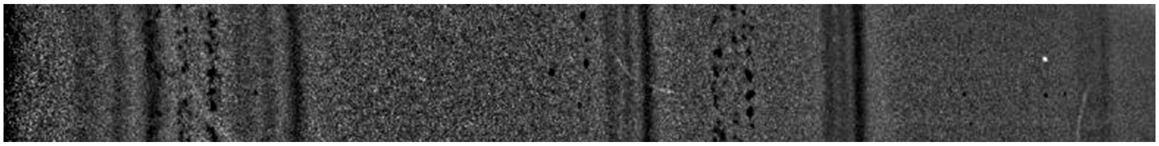

Figure 6.24. X-ray diffraction from a static 34.5 μm thick Bi foil in the Seeman-Bohlin geometry using a 4.75 keV, 4ns source. The signal to noise appeared sufficient for detecting a number of (*hkl*) planes in Bi, as well as the triplet resulting from the 1s2p -1s2 1P-1S and 1s2p - 1s2 3P-1S electronic transitions in He-like Ti.

7 SIMULATIONS OF ABLATION-DRIVEN SHOCKS

In our targets, shock formation via laser ablation and shock propagation was modeled using a 1D radiation hydrodynamics code (HYADES version 01.06.06). A 1D (in space) hydrodynamic treatment was sufficient in simulating the material response, since over the region of interest the loading conditions were such that uniform shock-loading (no edge effects) could be assumed. In practice, this was accomplished by laser drive spot diameters (> 1 mm) that by far exceeded the shock propagation distance in the sample (<100 μm).

In this Chapter, simulations performed in uncoated and parylene-N coated Mg are presented. These simulations provided an understanding of the relation between laser irradiance and pressure induced on Mg prior to experiments. Most importantly, they aided in the timing between the x-ray and drive pulse, where the delay of the x-ray pulse had to be predicted and set before each shot to an accuracy of ~0.5 ns. Selecting the correct delay was critical especially for coated Mg targets where the shock had to propagate initially across the width of the parylene-N ablator before reaching Mg. In these experiments, a too long of a delay posed the risk of capturing lattice information from Mg in release, which would have complicated our investigation of the shocked material response. A too short of a delay would have resulted in integrating only a small amount of diffracted signal from the shock-compressed lattice and therefore, in compressed lattice measurements with a very low signal-to-noise. Since the shock drive duration was ~7 ns while the x-ray backlighter drive was of the order of 2-4 ns, the room for error in the pump-probe timing of coated Mg targets was very small. Experiments with uncoated targets were much simpler, since the only concern for timing was the release from the back surface of the sample. However, there were three arguments behind the use of coated targets despite their timing complexities: 1) shock front generation on the ablator ensured that the x-ray pulse probed material that was not pre-heated by the ablation front causing spurious artifacts in the diffracted signal, 2) it was observed that the noise in diffraction from indirectly driven samples was much less than from samples driven directly (energetic electrons, x-ray emission), and 3) the impedance mismatch between the plastic ablator and Mg worked in our favor for producing the same shock pressure for a smaller irradiance compared to an uncoated Mg sample.

Besides laser irradiance vs. pressure other simulated parameters using HYADES were pressure as a function of propagation distance, especially depicting the pressure "jump" experienced at the ablator/Mg interface, and also temporal shock profile vs. laser irradiance history. A brief introduction on the 1D radiation hydrodynamics code HYADES is presented next.

7.1 An Introduction to HYADES Simulations

HYADES is a one dimensional radiation hydrodynamics code developed by Jon Larsen [148] in which the equations of continuum dynamics, heat conduction, and radiation transport are solved simultaneously. For simulating laser ablation and dynamic loading, three-temperature hydrodynamics (electrons, ions, radiation) are assumed. In the laser-matter interaction region ablation via laser deposition in the expanding plasma is simulated taking into account thermal conduction and radiation diffusion. In the bulk of the sample the material response is affected mainly by hydrodynamics. There the accuracy of the tabulated equation of state used (SESAME tables) is what determines the outcome of the simulations. For this reason, there exists a significant experimental and computational effort in testing and updating new and existing equation-of-state data within national laboratories especially LLNL and LANL.

HYADES uses a 1D Lagrangian frame of reference, namely a reference frame in which time derivatives are expressed along coordinates moving locally with the material. The partial differential equations representing the physics models used in HYADES are approximated by finite-difference discretization. Discretization is implemented in the input file of HYADES, where the material becomes partitioned into m zones defined by $m+1$ mesh points. Some physical quantities are calculated at the mesh points (e.g. position, velocity) and others at the zone centers (e.g. density, pressure). For this reason, the zone definition in the HYADES input file is generally the most crucial part of the simulations. On one hand, for an accurate computation of the shock parameters a large number of zones (zone width < 1 μm) is desirable. On the other hand, a large number of zones implies long computational times, so a balance must be found. In HYADES, this balance can be achieved with a "feathering" of the zone width in the regions where complex physics are expected.

In our case, for plastic ablator coated targets (including an 80 nm layer of Al flashing on top of the plastic) the problem was divided into five regions as shown in (Figure 7.1). Feathering was applied ensuring a small zone width (<10 nm) on the interface where complex physics was simulated. Feathering (with either decreasing or increasing zone width) was selected to be <15%, as recommended by Jon Larsen. For the stability of the code, it was also important that adjacent zones on an interface e.g. the plastic ablator and Mg interface, contained approximately the same mass. Therefore, calculations of the initial zone widths and feathering to satisfy the above criteria were necessary. In general, in order to run HYADES within a reasonable amount of computational time the total number of zones in a problem was kept to <300. For uncoated Mg targets, ~5% feathering over the width of the sample was applied (initial zone width of 1 nm).

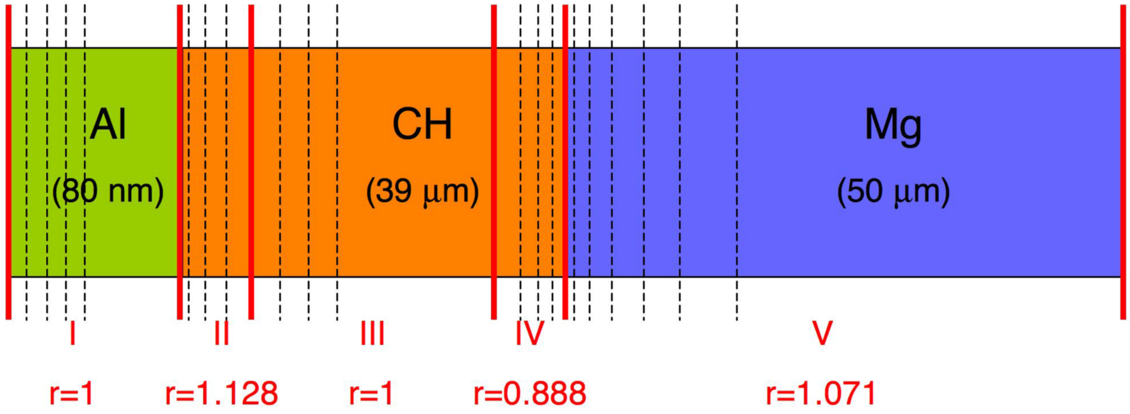

Figure 7.1. (not to scale) Definition of the HYADES problem for a coated Mg target consisting of an 80 nm Al flash coating, a 39 µm parylene-N coating and a 50 µm Mg sample. The problem was divided into five regions, each with a specific feathering as indicated. To minimize the number of zones (a zone is defined by adjacent dashed lines) feathering was applied at the interfaces only, over a few microns width. Mg was feathered towards an increasing zone width with a ratio of 1.071.

Other input parameters required to run HYADES simulations of laser-driven shocks were 1) a tabulated EOS (provided in the HYADES software package), 2) an ionization model for the calculation of conductivities for laser deposition and heat conduction (Thomas-Fermi or Saha) and 3) a flux limiter, chosen to be 0.03 of the free-stream value, a common choice for this type of simulations based on extensive comparisons of experimental data and HYADES simulations [149]. The flux limiter f is a factor entered in the heat flux equation $S = -\kappa \nabla T \approx f n_e v_e k_B T_e$ at the free-stream limit, to account for large temperature gradients where the electron mean free path $\lambda_e = v_e \tau_e$ may be larger than the plasma scale length $L = \frac{T_e}{\nabla T_e}$. In this situation, the heat flux equation must be corrected with a flux limiter f otherwise it predicts that thermal energy is transported in the plasma faster than the free-stream limit, which is not physical.

7.2 Simulations of Shock-Loading in Mg

We performed HYADES simulations to predict a shock pressure vs. laser intensity relationship in Mg. For coated samples these simulations provided the shock pressure in the ablator and in the sample for specific laser intensity. These results are plotted below together with the experimentally obtained pressure by velocimetry (Figure 7.2). A curve fitting to the pressure scaling law $P = a + bI^{\gamma}$ was applied. From the simple ablation model presented in Chapter 1, where shock generation was assumed to result from momentum transfer between the ablated particles and the solid material, a $\gamma \sim 0.66$ was expected. A ~20% difference in the simulated value of γ for the ablator could be attributed to the calculated conductivity for laser deposition and heat conduction, as well as the choice of the flux limiter.

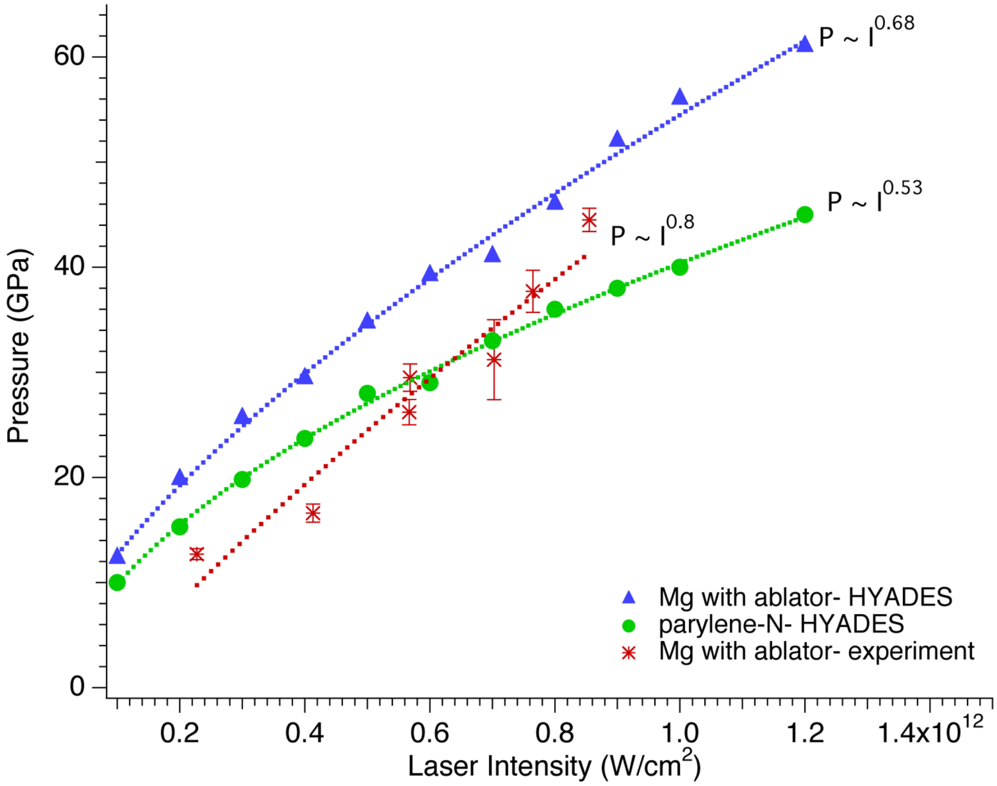

Figure 7.2. Pressure vs. laser irradiance for parylene-N and Mg as calculated by HYADES simulations. In the simulations, a flat top laser pulse (spatially and temporally) is incident on the Al flashing/parylene-N layer so that shock formation occurs in this layer, not in Mg. The experimentally obtained pressure vs. laser irradiance is also shown.

As expected, a pressure jump between the pressure in the parylene-N and Mg was evident in the simulations because of the impedance mismatch between the two materials. A direct comparison between ablator coated and uncoated Mg vs laser intensity is presented in (Figure 7.3). Here the experimentally measured shock pressure and laser intensity are plotted for the two types of targets. For laser intensities > 4x10^{11} W/cm^2 the pressure differential started to grow significantly (~50% at 8.5x10^{11} W/cm^2) supporting our argument for the use of an ablator to provide a pressure "boost" for a given laser intensity.

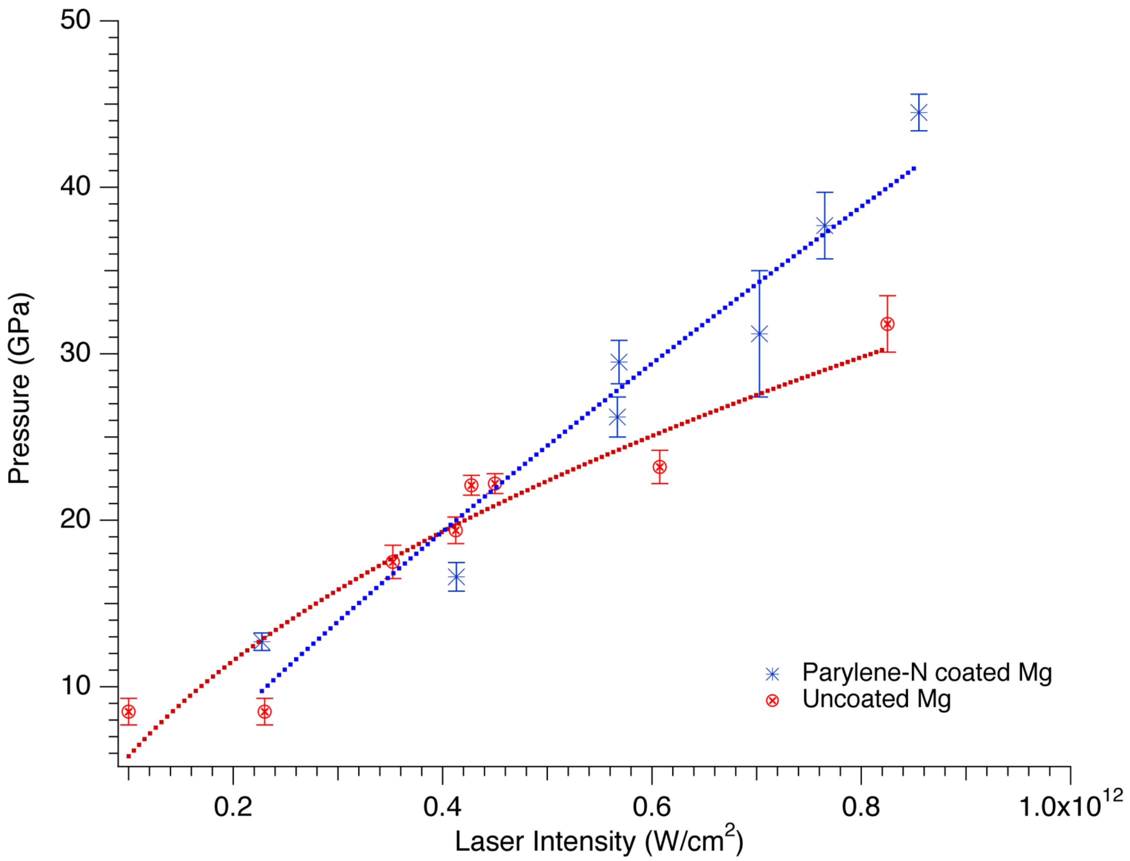

Figure 7.3. Comparison of the induced shock pressure between uncoated and coated Mg targets as a function of laser intensity.

1D hydrodynamics simulations in HYADES rarely agree with experimentally measured quantities because of the inherent approximations in the calculated physical quantities resulting from the finite-difference method. For this reason, HYADES simulations are typically scaled to experimental results. The offset between the experimental and simulated values appeared to be much smaller for uncoated targets, where the equation of state of one material (instead of three for coated targets) was used (Figure 7.4). In other words, the discrepancy observed between simulations and experiments could be due to inaccuracies in the EOS, as well as the definition of other parameters such as the flux limiter, artificial viscosity value, etc. Furthermore, discrepancies could arise from the simulated waveform (constant intensity, with 100 ps rise and fall time) versus the actual waveform. A closer examination of this problem is presented later in this Chapter.

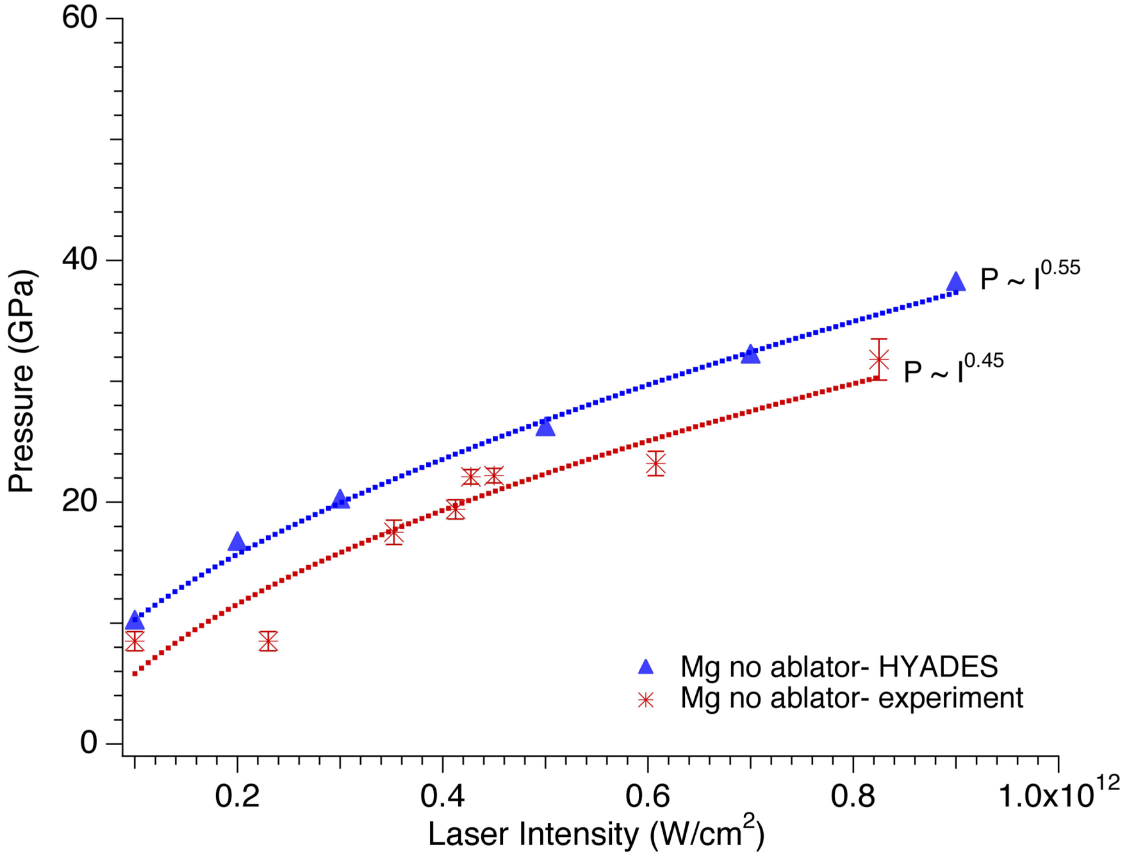

Figure 7.4. Pressure vs. laser irradiance for directly driven Mg samples, from HYADES simulations and experiments.

The approximate pressure vs. laser intensity scaling established by HYADES was used in conjunction with a known U_s-P relation for Mg and parylene-N to predict shock transit times in the ablator and Mg sample respectively (Figure 7.5). An estimate of these transit times proved to be extremely useful in defining the temporal delay between the x-ray probe pulse and the shock drive pulse such that both the uncompressed and compressed lattice details were captured on a single shot.

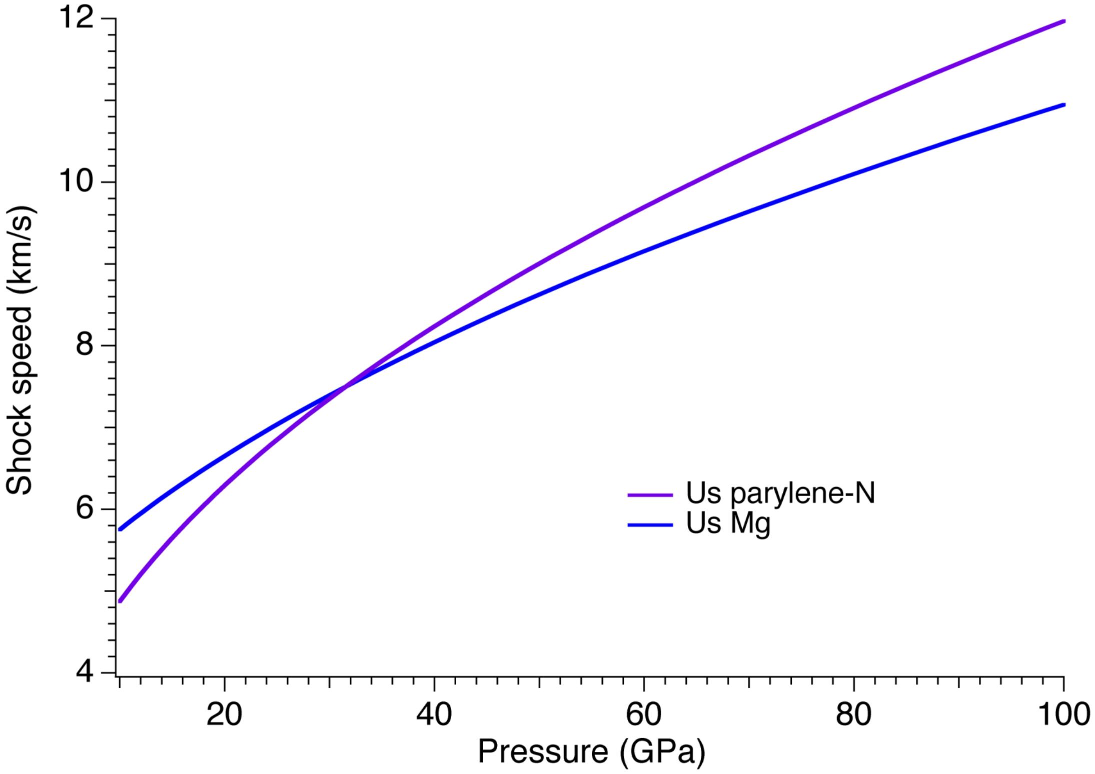

Figure 7.5. Plot of the shock speed as a function of pressure in Mg and in parylene-N.

To demonstrate the necessity for accurate pump-probe timing in x-ray diffraction experiments, snapshots of a shock propagating in a coated sample are plotted below (Figure 7.6). The modulations in the pressure amplitude shown here are artifacts of the simulation and may be dependent on the choice of the artificial viscosity value. At 6 ns, the shock formed in the ablator reaches the ablator/Mg interface as indicated by the sudden increase in pressure. Because of the transition into a higher density material a reflected shock is also formed at this interface with amplitude such that the addition of the incident and reflected shock amplitudes is equal to the transmitted shock amplitude. In the temporal window between 6-9 ns, the first 25 µm of Mg are compressed at a constant pressure. Since the attenuation length of 4.75 keV x-rays in Mg is approximately 25 µm, it is important that the amount of material contained in a depth of 25 µm is shock loaded to a constant pressure while being probed by the x-ray pulse. Therefore, for the loading conditions of this example, the x-ray pulse (e.g. 3 ns duration) should be switched on at t=5 ns such that 1 ns of the static and 2 ns of the compressed material at constant pressure are probed. A delay of the x-ray pulse to a later t=6 ns would result in no static signal being captured, whereas an even longer delay would be probing the lattice in release.

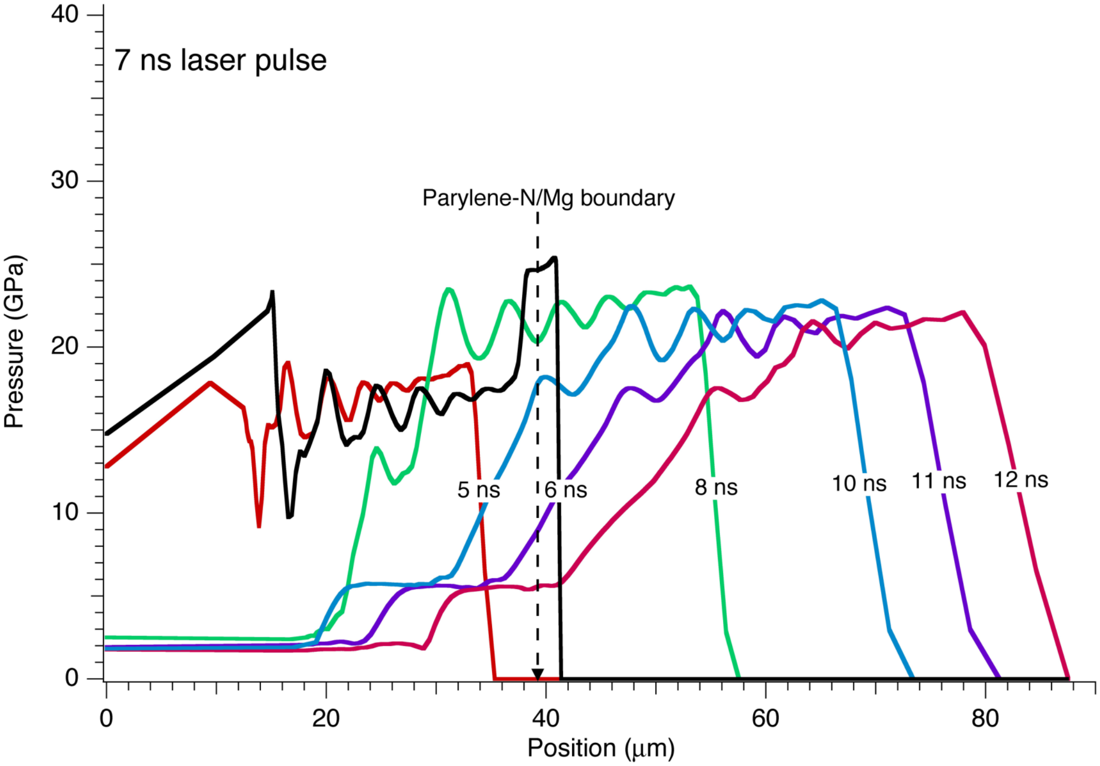

Figure 7.6. Snapshots of a shock front propagating in a coated Mg target (80 nm Al/39 µm CH/50 µm Mg). The incident laser pulse duration was 7 ns.

The accuracy in the pump and x-ray probe timing for uncoated targets was not as restrictive as for coated targets (Figure 7.7). In the example shown in Figure 7.7, a 3 ns x-ray pulse could have a maximum delay of 7 ns with respect to the 10 ns duration shock drive pulse.

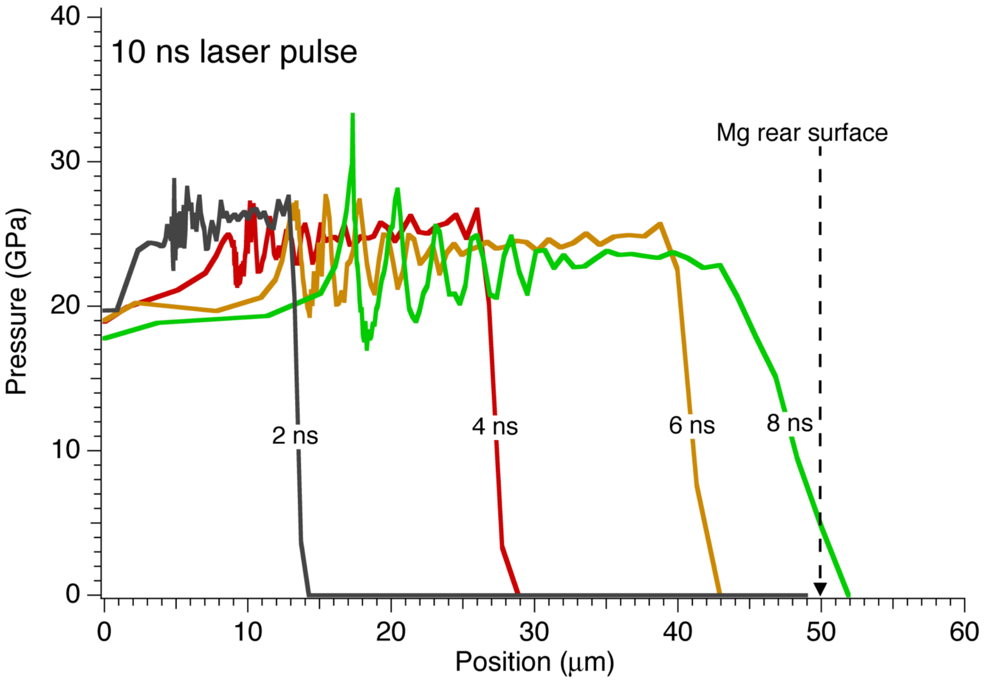

Figure 7.7. Snapshots of a shock front propagating in an uncoated 50 µm thick Mg target. The incident laser pulse duration was 10 ns.

7.3 Shock Profile versus Laser Temporal Waveform

We simulated various laser waveforms incident on coated targets in order to assess the sensitivity of the shock profile on the temporal features of the laser. Specifically, we varied the pulse duration of a constant intensity waveform and added ramped intensity profiles to waveforms of the same (7 ns) duration.

In the laser pulsewidth tests in coated targets, the most significant effects were observed for short laser pulsewidths, where the resultant shock profile suffered attenuation from the release wave catching up to the shock front. This is an undesirable situation for x-ray diffraction as the main goal is to probe the lattice at a single compression value, if possible, in order to be able to detect strength effects, elastic-plastic effects, phase transitions etc. Probing the lattice response to the shock front displayed in Figure 7.8 would result in broad diffraction peak widths representative of the compression range in this triangular shock profile. (Remember that the diffraction pattern is integrated over the duration of the x-ray pulse.) For this reason, the 39 μm parylene-N layer thickness in our experiments was tailored specifically to the 6-7 ns shock drive pulse.

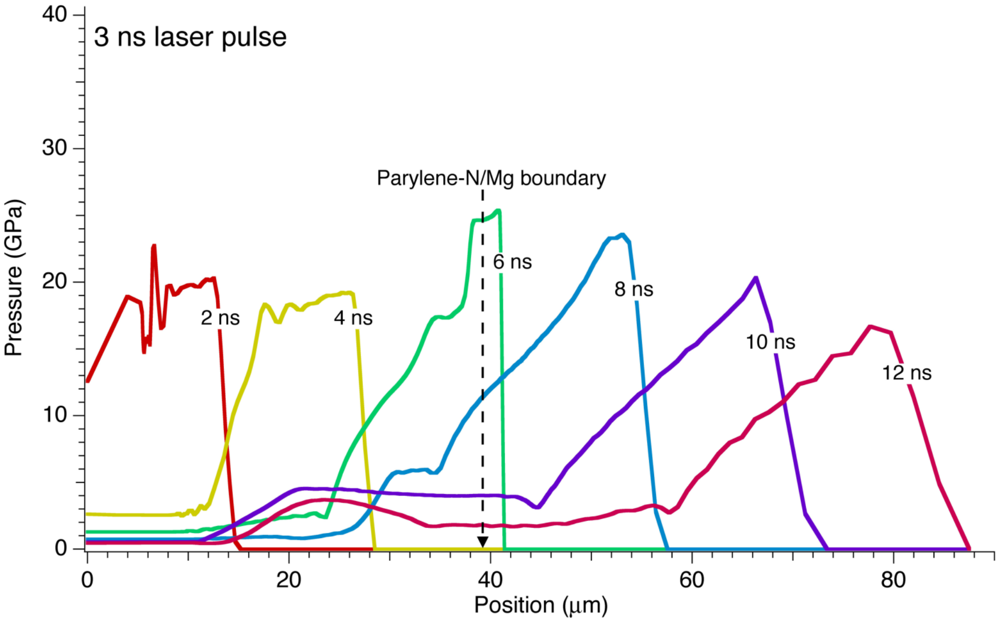

Figure 7.8. Simulation of a shock front propagating in a coated Mg sample with incident laser pulse duration of 3 ns. Shock amplitude attenuation is caused by the release wave catching up to the shock front.

Last, the effect of ramped, 7 ns pulsewidth, laser waveforms was investigated with HYADES simulations. Quite often during experiments, laser waveforms were observed to have ramps, so the following simulations helped in understanding their effect on the shock profile. The ramped laser profiles chosen are shown in Figure 7.9.

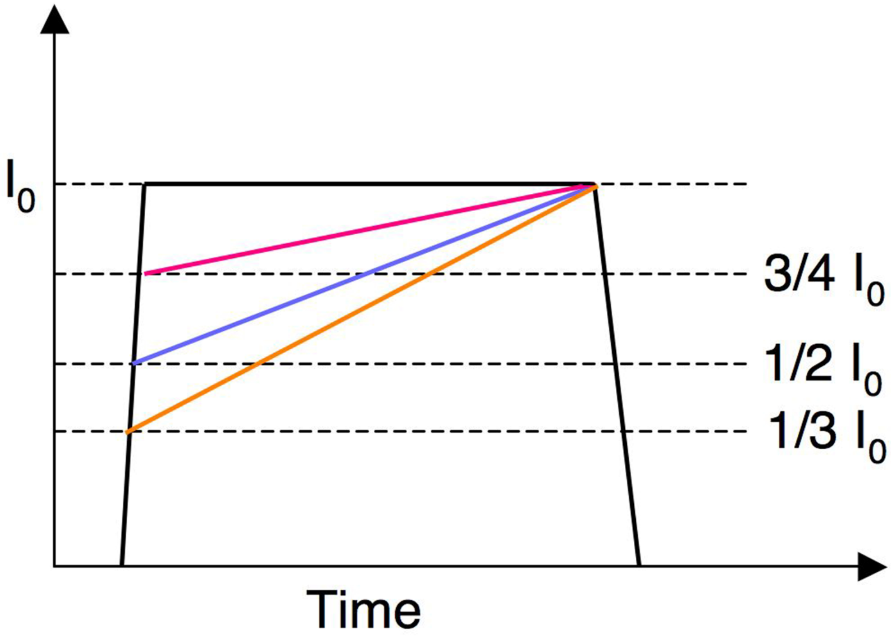

Figure 7.9. The ramped laser waveforms tested in HYADES for investigating the resultant shock profile .

Starting with a flat top intensity profile, we gradually introduced a slope with the steepest ramp starting at one third the peak intensity. Snapshots of the generated shock profiles from the three ramped laser waveforms propagating in a coated target are displayed in Figure 7.10. Surprisingly, the shock profiles were not affected by the ramped laser waveform, an observation also confirmed by HYADES simulations of Swift et al. in plastic ablators [149, 150]. To obtain a ramped shock profile, the pulse length would most likely have to be considerably extended in addition to the sloped intensity profile.

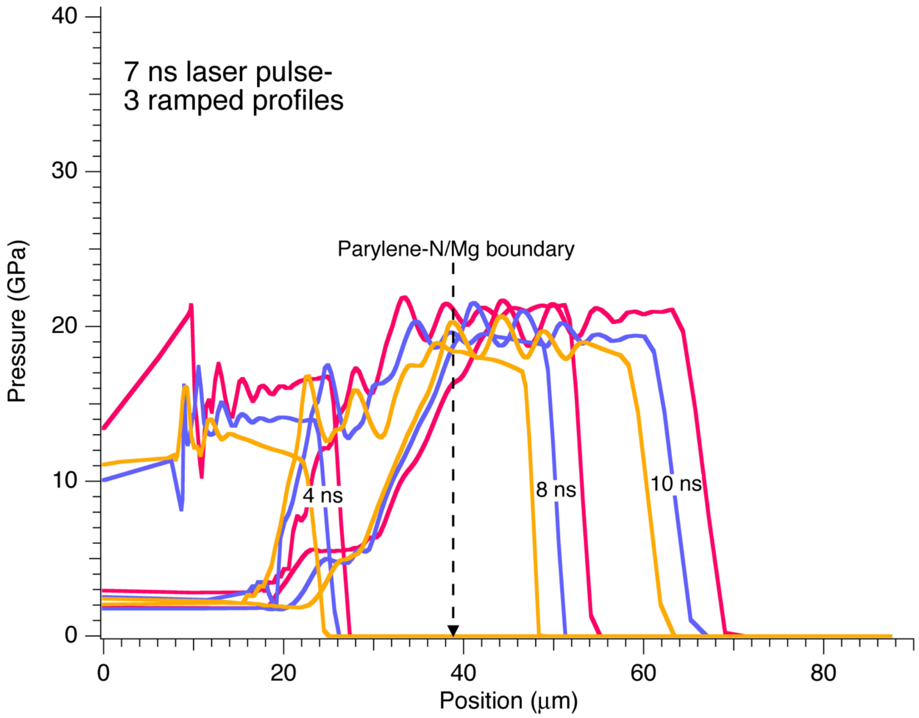

Figure 7.10. Snapshots of shock fronts propagating in a coated Mg sample, where the incident laser temporal profiles are designed with different ramped temporal shapes. The ramped laser profiles seem to have no obvious effect on the simulated shock profiles.

In summary, the HYADES simulations discussed here assisted us in understanding the pressure vs. laser intensity scaling in the ablators and in Mg, as well as selecting the appropriate pump-probe delays with an accuracy of ~ 1 ns. Furthermore, they provided a qualitative assessment of the factors influencing the shock profile in the material as a function of propagation distance. From the parameters tested, the laser pulsewidth appeared to be the most critical in the evolution of the shock profile in the sample.

8 CONCLUSIONS

8.1 Summary of Results

The main goal of this PhD work was to develop time-resolved lattice diagnostics employing x-ray diffraction, in order to identify and characterize the shocked material behavior at the relevant spatial and temporal scales. Shock-induced phase transitions were of particular interest to this study as shock-loading can alter drastically the timescales and thermodynamic pathway of the phase nucleation and growth process compared to quasistatic experiments. In addition, obtaining nanosecond snapshots of the lattice for a material undergoing phase transition is an extremely interesting problem because not only the timescales of the phase transition but also the atomic re-arrangement mechanism leading to the new structure can be revealed.

In pursuit of a lattice diagnostic with the necessary angular and temporal resolution as well as a satisfactory x-ray signal-to-noise ratio for nanosecond shock-loading experiments, we developed polycrystalline x-ray diffraction cameras using laser-based x-ray sources. These pulsed x-ray sources were generated from a thermal plasma K-shell line emission formed when a several hundred Joule, nanosecond laser pulse was focused on a thin (<12 μm) foil (Ti, Fe, Cu). These point x-ray sources were then adapted onto x-ray cameras where diffraction signals were captured in transmission or in reflection (or both) from shock driven or static samples.

In order to improve angular resolution and signal-to-noise in shocked lattice measurements, we designed and characterized a focusing diffraction camera. Focusing of x-rays diffracting from a broad area on a sample resulted from a simple geometric effect explained in detail in Chapter 5. Thus, via x-ray illumination of a large area of the sample and subsequent focusing on the detector, this Seeman-Bohlin-type diffraction camera demonstrated higher signal amplitudes compared to Debye-Scherrer-type cameras where a) the incident collimated beam illuminates only a narrow spot on the sample (otherwise the angular resolution is compromised) and b) the diffracted peaks from the sample diverge with increasing sample-detector distance. In addition, the focusing geometry exhibited angular resolution of <1° by resolving the 2P level splitting in Fe He_a-like emission (1.8505 Å and 1.8595 Å) upon diffraction from the Cu (311) and (222) planes. Following initial characterization tests with static samples, polycrystalline Cu samples were shocked in this diffraction geometry. Information from isotropically lattice planes was captured for the first time from this type of diffraction camera. Having provisioned access to a line-imaging velocimeter both lattice and free surface velocity measurements were obtained simultaneously, thus allowing for a proof-of-principle equation of state measurement in Cu with <1% error in the density and particle velocity measured via diffraction and velocimetry respectively. If time permitted, a more thorough investigation on the equation of state of Cu (or another polycrystalline material) would have been performed. In addition, we demonstrated the application of this camera in studies of amorphous materials by acquiring diffraction signal from metallic glass.

After having developed nanosecond x-ray diffraction techniques, the next set of experiments involved identifying a shock-induced phase transition. We selected polycrystalline Mg because its principal Hugoniot intersects the solid-solid and solid-melt phase boundaries at readily accessible pressures (or laser intensities). In addition, the hcp-bcc phase boundary in Mg has been highly controversial; A number of first principles calculations within the framework of density functional theory have attempted to define the hcp-bcc phase boundary in Mg taking advantage of its simple atomic arrangement; however, because of the small free energy difference between the competing crystal structures, the location of the hcp-bcc phase boundary has been predicted with a variation of ~5 GPa at room temperature, to >8 GPa for T>500 K. Here, using laser-based nanosecond x-ray diffraction and shock-loading we obtained a direct lattice measurement of the hcp to bcc phase transition in polycrystalline Mg. The peak shock pressure above which the bcc phase became evident was 26.2±1.3 GPa in agreement with the bcc phase boundary calculated by Moriarty et al. using a total energy pseudopotential method. The subnanosecond timescale of the phase transition implied by the shock-loading conditions was in agreement with the kinetics of a martensitic transformation.

We also attempted to diagnose shock-induced melt on the bcc-liquid boundary in Mg (~60 GPa) and in Bi (~ 3 GPa if preheated to >475 K and P>70 GPa from T=293 K). The solid-liquid phase transition in Bi under shock is a particularly interesting problem because of the yet to be understood timescales and thermodynamic transition pathway. Unfortunately, poor signal-to-noise mainly attributed to the ablation noise and sample fluorescence, and an extremely small x-ray penetration depth (<2 μm) did not allow for any lattice compression to be detected in Bi. However, having gained significant knowledge from these preliminary experiments in Bi and other polycrystalline materials, we are now in a position where we can define the experimental geometry for a successful lattice-level investigation on shock-compressed Bi and other high Z materials in general.

Finally, a series of 1D hydrodynamic simulations was performed to gain an understanding of the plastic ablator pressure and sample pressure vs. laser intensity scaling as well as the shock transit times in both the plastic ablator and Mg. A prediction of these parameters prior to experiments was important for planning the shots (e.g. determine the phase plate focal spot size) and also for providing an accurate pump-probe timing during the experiments. Timing to within ~0.5 ns was critical to our experimental results, since it ensured that lattice information from both the static (reference) lattice and compressed lattice were captured. In addition, hydrodynamic simultations aided in understanding how sensitivities in the temporal profile of the laser translated to features on the shock profile. It was found that laser profiles with a small intensity ramp still produced stable shocks of approximately constant amplitude; however, laser profiles below a certain duration caused shock waves in the sample to attenuate rapidly with propagation distance, a situation that is undesirable for lattice measurements where the compression detected averages over the penetration depth in the material.

8.2 Progress Towards Lattice Measurements in Shocked High Z Materials

During our dynamic x-ray diffraction experiments testing high Z materials such as Bi, several challenges were identified as mentioned earlier. The potential solutions to these challenges are now presented.

Perhaps the most important challenge in x-ray diffraction from high Z materials is their short x-ray penetration depth (<5 μm for <8.4 keV x-rays) which limits the allowed sample thickness for x-ray detection in transmission. To alleviate this problem, we suggested employing a focusing diffraction geometry where the focused signals are captured in reflection from the sample. It was soon realized that the ablation noise and fluorescence from the high Z materials contributed to a significant background in our x-ray diffraction measurements in reflection from the sample. Therefore, it was concluded that for experiments probing high Z materials, a diffraction geometry in transmission from the sample would be necessary, since the sample itself would act as a noise filter. However, the challenge in implementing a transmissive geometry is that the samples would have to have a thickness equivalent to the x-ray penetration depth. Such samples, especially for high Z materials are very expensive and difficult to produce (even with sputter deposition techniques). Furthermore, thin samples imply extremely short shock transit times so that effects from the interaction of the release wave with the shock front may be observed.

Here we suggest different methods for performing lattice measurements from shocked high Z materials. The first method takes advantage of the noise filtering provided by the sample itself (see diffraction images in Mg), without however any sample thickness limitations. To achieve this, we suggest that the laser drive and x-ray probe are incident on opposite sides of the sample. In this way, the ablation noise is filtered by the sample whose thickness in this case is not limited by the penetration depth of the x-rays. The sample can be placed in the focusing geometry described in this dissertation to exploit the increased signal amplitude and angular resolution. In this configuration, the ablation noise issue in high Z targets should be resolved. However, this arrangement would require a very precise timing of the x-ray pulse such that the lattice is probed before any release occurs. In order to increase the x-ray penetration depth, development of higher energy x-ray backlighters would be required. In addition, the focusing camera would have to allow velocimetry access from the side of the x-ray source, something that can be done relatively easily.

A second method for probing shocked high Z materials, which would target to increase the signal-to-noise in a reflective geometry, would be to use multiple x-ray backlighter sources. In principle, such an experiment could be performed within a multi-kJ laser facility such as the OMEGA laser at LLE and potentially the National Ignition Facility.

From the experiments performed here, the x-ray signal-to-noise ratio was the main battle to be won in detecting shock-induced phase transitions, especially melt. Even though multiple laser-based x-ray sources probing the target simultaneously with the laser-driven load will be the way forward for *in situ* lattice measurements at laser facilities, experiments could in principle be performed at an x-ray source with better spectral brightness such as LCLS. The prospect of coupling high energy laser systems to the free electron laser at LCLS is very attractive for high energy density materials science as all the methods discussed earlier in improving the signal levels would not be necessary with a tunable (2-25 keV) narrow linewidth ($\frac{\Delta\lambda}{\lambda} = 10^{-3}$) x-ray source such as LCLS. Furthemore, the spatial coherence of LCLS could prove to be invaluable in extracting both phase and amplitude information from the scattered signal from dynamically driven targets.

8.3 Future Work

We propose continuing the investigation of shock-induced phase transitions addressing the following:

1) A complete map of the hcp-bcc boundary in Mg in order to assess the validity of *ab initio* calculations. Such measurement would be possible with a heated target capability provided by either a CW laser beam or conductive heating via a substrate. By preheating Mg targets to different initial temperatures an investigation of the intersection of the bcc boundary along different Hugoniots would be possible.
2) The phase transition pathway in the shock-induced hcp-bcc transition in Mg is another interesting problem, which could be addressed via shock-loading single crystal Mg along different crystallographic orientations. With a known lattice and shock orientation, dynamic x-ray diffraction could reveal the atomic re-arrangement mechanism. Such mechanism has been proposed for Mg through *ab initio* molecular dynamics simulations but has never been experimentally verified.
3) Because of the relatively low pressure melt boundary in Mg (>60 GPa) and the long penetration depth of the material, Mg would be the ideal candidate for continuing the investigation of shock-induced melt, prior to performing melt experiments in high Z materials. Preliminary data has shown that for melt experiments to be successful, our signal-to-noise ratio would have to be improved significantly. We propose that future experiments on this problem be performed

at LCLS taking advantage of its high spectral brightness (10^{12} photons per pulse, linewidth $\frac{\Delta\lambda}{\lambda} = 10^{-3}$).

4) Upon successful demonstration of shock-melt in a low Z material such as Mg, Bi would be the next material forward for this type of studies. In Bi, information on both the timescale and thermodynamic path of the loading process are extremely interesting and for this reason, measurements with subpicosecond temporal resolution would be required. Again, the free electron x-ray laser at LCLS with x-ray pulses of 2-300 fs would be an ideal venue for this study, as it would provide both the temporal and spatial resolution to understand the highly speculated Bi response under shock-loading.
5) Last, 2D (or 3D) dynamic diffractive imaging from non-periodic structures [151, 152] is another avenue of experiments that the author has found extremely interesting for gaining an insight into the nanoscale phenomena that lead into the bulk phase transformation. Diffractive imaging exploiting the coherence of free-electron x-ray sources has already demonstrated imaging of biological structures and single atomic layers [153-155]. We envisage that this technique could be used to elucidate the processes occurring at a nanoscale level in a shock-loaded material, thus providing snapshots of defect formation in the material, phase nucleation and growth, and possibly the shock formation mechanism itself.

9 REFERENCES

1. Bozier, J.C., et al., *A new supercritical shock wave regime*. Astrophysical Journal Supplement Series, 2000. **127**(2): p. 253-260.

2. Collins, G.W., et al., *Temperature measurements of shock compressed liquid deuterium up to 230 GPa*. Physical Review Letters, 2001. **87**(16): p. art. no.-165504.

3. Fortney, J.J., *The structure of jupiter, saturn, and exoplanets: Key questions for high-pressure experiments*. Astrophysics and Space Science, 2007. **307**(1-3): p. 279-283.

4. Hawreliak, J., et al., *Modeling planetary interiors in laser based experiments using shockless compression*. Astrophysics and Space Science, 2007. **307**(1-3): p. 285-289.

5. Remington, B.A., *High energy density laboratory astrophysics*. Plasma Physics and Controlled Fusion, 2005. **47**: p. A191-A203.

6. Boehler, R., *Temperatures in the Earth's core from melting point measurements of iron at high static pressures*. Nature, 1993. **363**(6429): p. 534-536.

7. Solomatov, V.S. and D.J. Stevenson, *Can Sharp Seismic Discontinuities Be Caused by Nonequilibrium Phase-Transformations*. Earth and Planetary Science Letters, 1994. **125**(1-4): p. 267-279.

8. Knudson, M.D., M.P. Desjarlais, and D.H. Dolan, *Shock-Wave Exploration of the High-Pressure Phases of Carbon*. Science, 2008. **322**(5909): p. 1822-1825.

9. Olson, R.E., et al., *Shock propagation, preheat, and x-ray burnthrough in indirect-drive inertial confinement fusion ablator materials*. Physics of Plasmas, 2004. **11**(5): p. 2778-2789.

10. Tabak, M., et al., *Ignition and high-gain with ultrapowerful lasers*. Physics of Plasmas, 1994. **1**(5): p. 1626-1634.

11. Benuzzi-Mounaix, A., et al., *Laser-driven shock waves for the study of extreme matter states*. Plasma Physics and Controlled Fusion, 2006. **48**(12B): p. B347-B358.

12. Davis, J.P., et al., *Magnetically driven isentropic compression to multimegabar pressures using shaped current pulses on the Z accelerator*. Physics of Plasmas, 2005. **12**(5).

13. Luo, S.N., et al., *Laser-induced shock waves in condensed matter: Some techniques and applications*. High Pressure Research, 2004. **24**(4): p. 409-422.

14. Gupta, D.C. and S. Kulshrestha, *Pressure-induced phase transitions and electronic structure of GaAs*. Journal of Physics-Condensed Matter, 2008. **20**(25).

15. Jaffe, J.E., et al., *LDA and GGA calculations for high-pressure phase transitions in ZnO and MgO*. Physical Review B, 2000. **62**(3): p. 1660-1665.

16. Rousseau, R., et al., *Ab initio simulation of phase transitions and dissociation of H2S at high pressure*. Physical Review Letters, 2000. **85**(6): p. 1254-1257.

17. Bernasconi, M., G.L. Chiarotti, and E. Tosatti, *Ab-initio calculations of structural and electronic properties of gallium solid-state phases*. Physical Review B, 1995. **52**(14): p. 9988-9998.

18. Kadau, K., et al., *Atomistic simulations of shock-induced transformations and their orientation dependence in bcc Fe single crystals*. Physical Review B, 2005. **72**(6).

19. Baskes, M.I., *Modified embedded-atom potentials for cubic metals and impurities*. Physical Review B, 1992. **46**(5): p. 2727-2742.

20. Kadau, K., et al., *Microscopic view of structural phase transitions induced by shock waves*. Science, 2002. **296**(5573): p. 1681-1684.

21. Meyers, M.A., et al., *Laser-induced shock compression of monocrystalline copper: characterization and analysis*. Acta Materialia, 2003. **51**(5): p. 1211-1228.

22. Schneider, M.S., et al., *Laser-induced shock compression of copper: Orientation and pressure decay effects*. Metallurgical and Materials Transactions a-Physical Metallurgy and Materials Science, 2004. **35A**(9): p. 2633-2646.

23. Smith, C.S., *Metallographic studies of metals after explosive shock*. Transactions of the American Institute of Mining and Metallurgical Engineers, 1958. **212**: p. 574-589.

24. Arrigoni, M., et al., *Laser Doppler interferometer based on a solid Fabry-Perot etalon for measurement of surface velocity in shock experiments*. Measurement Science & Technology, 2009. **20**(1): p. 7.

25. Weng, J.D., et al., *Optical-fiber interferometer for velocity measurements with picosecond resolution*. Applied Physics Letters, 2006. **89**(11): p. 3.

26. Weng, J.D., et al., *A compact all-fiber displacement interferometer for measuring the foil velocity driven by laser*. Review of Scientific Instruments, 2008. **79**(11): p. 3.

27. Grigsby, W., et al., *Picosecond time scale dynamics of short pulse laser-driven shocks in tin*. Journal of Applied Physics, 2009. **105**(9): p. 10.

28. Henon, S. and J. Meunier, *Ellipsometry and reflectivity at the Brewster-angle-tools to study the bending elasticity and phase-transitions in monolayers at liquid interfaces*. Thin Solid Films, 1993. **234**(1-2): p. 471-474.

29. Ivlev, G.D., E.I. Gatskevich, and D.N. Sharaev, *Time-resolved temperature and reflectivity measurements at the nanosecond laser-induced melting and crystallization of silicon*, in *Laser-Assisted Microtechnology 2000*, V.P. Veiko, Editor. 2001, Spie-Int Soc Optical Engineering: Bellingham. p. 78-81.

30. Shank, C.V., R. Yen, and C. Hirlimann, *Time-resolved reflectivity measurements of femtosecond-optical-pulse induced phase-transitions in silicon*. Physical Review Letters, 1983. **50**(6): p. 454-457.

31. Werdiger, M., et al., *Detecting of melting by changes of rear surface reflectivity in shocked compressed metals using an interferometric diagnostic method*. Laser and Particle Beams, 1999. **17**(3): p. 547-556.

32. Dai, C.D., J.B. Hu, and H. Tan, *Hugoniot temperatures and melting of tantalum under shock compression determined by optical pyrometry*. Journal of Applied Physics, 2009. **106**(4): p. 7.

33. Gogulya, M.F., A.Y. Dolgoborodov, and M.A. Brazhnikov, *Investigation of shock and detonation waves by optical pyrometry*. International Journal of Impact Engineering, 1999. **23**(1): p. 283-293.

34. Seifter, A. and A.W. Obst, *About the proper wavelength for pyrometry on shock physics experiments*. International Journal of Thermophysics, 2007. **28**(3): p. 934-946.

35. Kalantar, D.H., et al., *Multiple film plane diagnostic for shocked lattice measurements (invited)*. Review of Scientific Instruments, 2003. **74**(3): p. 1929-1934.

36. Wark, J.S., et al., *Subnanosecond x-ray diffraction from laser-shocked polycrystals*. Physical Review B, 1989. **40**(8): p. 5705-5714.

37. Swift, D.C., *X-ray diffraction from shock-loaded polycrystals*. Review of Scientific Instruments, 2008. **79**(1).

38. Hawreliak, J., et al., *Nanosecond x-Ray diffraction from polycrystalline and amorphous materials in a pinhole camera geometry suitable for laser shock compression experiments*. Review of Scientific Instruments, 2007. **78**(8).

39. Loveridge-Smith, A., et al., *Anomalous elastic response of silicon to uniaxial shock compression on nanosecond time scales*. Physical Review Letters, 2001. **86**(11): p. 2349-2352.

40. Barker, L.M. and Hollenbach R., *Shock-wave study of alpha reversible epsilon-phase transition in iron*. Journal of Applied Physics, 1974. **45**(11): p. 4872-4881.

41. Kalantar, D.H., et al., *Direct observation of the alpha-epsilon transition in shock-compressed iron via nanosecond x-ray diffraction*. Physical Review Letters, 2005. **95**(7).

42. Boslough, M.B. and J.R. Asay, *Basic Principles of Shock Compression*, in *High Pressure Shock Compression of Solids*, J.R. Asay and M. Shahinpoor, Editors. 1993, Springer-Verlag: New York. p. 7-42.

43. Meyers, M.A., *Dynamic Behavior of Materials*. 1994, New York: Wiley-Interscience.

44. Zel'dovich, Y.B. and Y.P. Raizer, *Physics of Shock Waves and High-Temperature Hydrodynamic Phenomena*. 2002, Mineola, New York: Dover Publications.

45. Asay, J.R. and M. Shahinpoor, *High-pressure shock compression of solids*. 1993, New York: Springer-Verlag.

46. Courtney, T.H., *Mechanical Behavior of Materials*. 2000, New York: McGraw-Hill.

47. Graham, R.A., *Solids under high-pressure shock compression: mechanics, physics and chemistry*. 1993, New York: Springer Verlag.

48. Meyers, M.A. and K.K. Chawla, *Mechanical Metallurgy Principles and Applications*. 1984, Englewood Cliffs, NJ: Prentice-Hall.

49. Asay, J.R. and J. Lipkin, *Self-consistent technique for estimating dynamic yield strength of a shock-loaded material*. Journal of Applied Physics, 1978. **49**(7): p. 4242-4247.

50. Asay, J.R., *Shock-induced melting in bismuth*. Journal of Applied Physics, 1974. **45**(10): p. 4441-4452.

51. Hayes, D.B., *Wave-propagation in a condensed medium with N transforming phases-application to solid-I-solid-II liquid bismuth*. Journal of Applied Physics, 1975. **46**(8): p. 3438-3443.

52. Johnson, J.N., D.B. Hayes, and J.R. Asay, *Equations of state and shock-induced transformations in solid I-solid II-liquid bismuth*. Journal of Physics and Chemistry of Solids, 1974. **35**(4): p. 501-515.

53. Romain, J.P., *Phase-transformation in bismuth under shock loading*. Journal of Applied Physics, 1974. **45**(1): p. 135-139.

54. Servas, J.M., J. Perraud, and G. Ledon, *Detection of phase-transitions in shock-loaded bismuth*. Journal De Physique, 1988. **49**(C-3): p. 627-632.

55. Wetta, N. and J.L. Pelissier, *A model-potential approach for bismuth (II). Behaviour under shock loading*. Physica A, 2001. **289**(3-4): p. 479-497.

56. Peng, J.X., et al., *Pressure and temperature dependence of shear modulus and yield strength for aluminum, copper, and tungsten under shock compression*. Journal of Applied Physics, 2005. **98**(1).

57. Schneider, M.S., et al., *Laser shock compression of copper and copper-aluminum alloys*. International Journal of Impact Engineering, 2005. **32**(1-4): p. 473-507.

58. Tonks, D.L., *Rate-dependent plasticity of copper and stainless-steel under shock compression*. Journal of Applied Physics, 1989. **66**(5): p. 1951-1960.

59. Moriarty, J.A. and J.D. Althoff, *First-principles temperature-pressure phase-diagram of magnesium*. Physical Review B, 1995. **51**(9): p. 5609-5616.

60. Duval, G.E. and R.A. Graham, *Phase Transitions Under Shock-Wave Loading*. Reviews of Modern Physics, 1977. **49**(3): p. 523-579.

61. Bancroft, D., E.L. Peterson, and S. Minshall, *Polymorphism of iron at high pressure*. Journal of Applied Physics, 1956. **27**(3): p. 291-298.

62. Kalantar, D.H., et al., *Direct observation of the alpha-epsilon transition in shock-compressed iron via nanosecond x-ray diffraction*. Physical Review Letters, 2005. **95**(7): p. -.

63. Wang, F.M. and R. Ingalls, *Iron bcc-hcp transition: Local structure from x-ray-absorption fine structure*. Physical Review B, 1998. **57**(10): p. 5647-5654.

64. Yaakobi, B., et al., *EXAFS measurement of iron bcc-to-hcp phase transformation in nanosecond-laser shocks*. Physical Review Letters, 2005. **95**(7).

65. Avrami, M., *Kinetics of phase change I - General theory*. Journal of Chemical Physics, 1939. **7**(12): p. 1103-1112.

66. Bastea, M., et al., *Kinetics of propagating phase transformation in compressed bismuth*. Physical Review B, 2005. **71**(18).

67. Zhang, M.X. and P.M. Kelly, *Crystallographic features of phase transformations in solids*. Progress in Materials Science, 2009. **54**(8): p. 1101-1170.

68. Wentzcovitch, R.M., *Hcp-to-bcc pressure-induced transition in Mg simulated by ab-initio molecular-dynamics*. Physical Review B, 1994. **50**(14): p. 10358-10361.

69. Wentzcovitch, R.M. and M.L. Cohen, *Theoretical-model for the hcp-bcc tranisition in Mg*. Physical Review B, 1988. **37**(10): p. 5571-5576.

70. Will, G. and H. Berndt, *Kinetics of the pressure-induced first-order phase transformation of RbJ*. High Pressure Research, 2001. **21**(3-4): p. 215-225.

71. Chhabildas, L.C., et al., *Particle launch to 19km/s for micro-meteoroid simulation using enhanced three-stage light gas gun hypervelocity launcher techniques*. International Journal of Impact Engineering, 2006. **33**(1-12): p. 799-811.

72. Lemke, R.W., et al., *Magnetically accelerated, ultrahigh velocity flyer plates for shock wave experiments*. Journal of Applied Physics, 2005. **98**.

73. Ng, A., D. Parfeniuk, and L. Dasilva, *Hugoniot measurements for laser-generated shock-waves in aluminum*. Physical Review Letters, 1985. **54**(24): p. 2604-2607.

74. Swift, D.C., et al., *Shock pressures induced in condensed matter by laser ablation*. Physical Review E, 2004. **69**(3).

75. Regan, S.P., et al., *Laser absorption, mass ablation rate, and shock heating in direct-drive inertial confinement fusion*. Physics of Plasmas, 2007. **14**(5).

76. Krumbein, A.D., Y. Shima, and H. Yatom, *Inverse bremsstrahlung energy-absorption in laser-irradiated plasmas*. Journal of Applied Physics, 1978. **49**(12): p. 6167-6168.

77. Skupsky, S., *Coulomb logarithm for inverse bremsstrahlung laser-absorption*. Physical Review A, 1987. **36**(12): p. 5701-5712.

78. Pert, G.J., *Inverse bremsstrahlung absorption in large radiation fields during binary collisions-classical theory*. Journal of Physics Part a General, 1972. **5**(4): p. 506-&.

79. Rand, S., *Inverse bremsstrahlung with high-intensity radiation fields*. Physical Review|Physical Review, 1964: p. 10.1103/PhysRev.136.B231.

80. Kruer, W.L., *The Physics of Laser Plasma Interactions*. 2003, Boulder: Westview Press.

81. Spitzer, L. and R. Harm, *Transport phenomena in a completely ionized gas*. Physical Review, 1953. **89**(5): p. 977-981.

82. Celliers, P., et al., *Thermal equilibrium in a shock-wave*. Physical Review Letters, 1992. **68**(15): p. 2305-2308.

83. Partouche-Sebban, D. and J.L. Pelissier, *Emissivity and temperature measurements under shock loading, along the melting curve of bismuth*. Shock Waves, 2003. **13**(1): p. 69-81.

84. Dai, C.D., J.B. Hu, and H. Tan, *Hugoniot temperatures and melting of tantalum under shock compression determined by optical pyrometry*. Journal of Applied Physics, 2009. **106**(4).

85. Seifter, A., et al., *Use of IR pyrometry to measure free-surface temperatures of partially melted tin as a function of shock pressure*. Journal of Applied Physics, 2009. **105**(12).

86. Ashcroft, N.W. and N.D. Mermin, *Solid State Physics*. 2004: Thomson.

87. Marder, M.P., *Condensed Matter Physics*. 2000, New York: Wiley-Interscience.

88. Cullity, B.D. and S.R. Stock, *Elements of X-Ray Diffraction*. 3rd ed. 2001, Upper Saddle River, NJ: Prentice Hall.

89. Warren, B.E., *X-Ray Diffraction*. 1990, New York: Dover.

90. Guinier, A., *X-ray Diffraction in Crystals, Imperfect Crystals, and Amorphous Bodies*. 1994, New York: Dover.

91. Beg, F.N., et al., *A study of picosecond laser-solid interactions up to 10(19) W cm(-2)*. Physics of Plasmas, 1997. **4**(2): p. 447-457.

92. Kruer, W.L., *Intense laser-plasma interactions- from Janus to Nova*. Physics of Fluids B-Plasma Physics, 1991. **3**(8): p. 2356-2366.

93. Ruggles, L.E., et al., *Measurements of 4-10 keV x-ray production with the Z-Beamlet laser*. Review of Scientific Instruments, 2003. **74**(3): p. 2206-2210.

94. Phillion, D.W. and C.J. Hailey, *Brightness and duration of x-ray-line sources irradiated with intense 0.53-mu-m laser-light at 60 and 120 ps pulse width*. Physical Review A, 1986. **34**(6): p. 4886-4896.

95. Burnett, N.H., et al., *Time-resolved /b K/ alpha spectra in high-intensity laser-target interaction*. Physical Review A (General Physics)|Physical Review A (General Physics), 1984. **29**(4): p. 2294-7.

96. Mascaren.Y and Mascaren.S, *Diffraction camera for precision measurement of lattice parameters at low temperatures*. Review of Scientific Instruments, 1967. **38**(1): p. 141-&.

97. Woolsey, N.C., J.S. Wark, and D. Riley, *Subnanosecond X-Ray-Powder Diffraction*. Journal of Applied Crystallography, 1990. **23**: p. 441-443.

98. Gales, S.G. and C.D. Bentley, *Image plates as x-ray detectors in plasma physics experiments*. Review of Scientific Instruments, 2004. **75**(10): p. 4001-4003.

99. Cullity, B.D., *Elements of X-ray Diffraction*. 1956, Reading, MA: Addison-Wesley.

100. Rosolankova, K., et al., *Measuring stacking fault densities in shock-compressed FCC crystals using in situ x-ray diffraction*. Journal of Physics-Condensed Matter, 2006. **18**(29): p. 6749-6757.

101. Benuzzi-Mounaix, A., et al., *Absolute equation of state measurements of iron using laser driven shocks*. Physics of Plasmas, 2002. **9**(6): p. 2466-2469.

102. Cauble, R., et al., *Absolute equation-of-state data in the 10-40 Mbar (1-4 TPa) regime*. Physical Review Letters, 1998. **80**(6): p. 1248-1251.

103. DaSilva, L.B., et al., *Absolute equation of state measurements on shocked liquid deuterium up to 200 GPa (2 Mbar)*. Physical Review Letters, 1997. **78**(3): p. 483-486.

104. Bernard, S. and J.B. Maillet, *First-principles calculation of the melting curve and Hugoniot of tin*. Physical Review B, 2002. **66**(1).

105. Tsuji, K., et al., *Pressure dependence of the structure of liquid group 14 elements*. Journal of Physics-Condensed Matter, 2004. **16**(14): p. S989-S996.

106. Humphreys, F.J., *Review - Grain and subgrain characterisation by electron backscatter diffraction*. Journal of Materials Science, 2001. **36**(16): p. 3833-3854.

107. Mack, M. and W. Parrish, *Seemann-Bohlin X-Ray Diffractometry .2. Comparison of Aberrations and Intensity with Conventional Diffractometer*. Acta Crystallographica, 1967. **23**: p. 693-&.

108. Margulies, L., G. Winther, and H.F. Poulsen, *In situ measurement of grain rotation during deformation of polycrystals*. Science, 2001. **291**(5512): p. 2392-2394.

109. Upmanyu, M., et al., *Simultaneous grain boundary migration and grain rotation*. Acta Materialia, 2006. **54**(7): p. 1707-1719.

110. Funamori, N., T. Yagi, and T. Uchida, *Deviatoric stress measurement under uniaxial compression by a powder x-ray-diffraction method*. Journal of Applied Physics, 1994. **75**(9): p. 4327-4331.

111. Barker, L.M. and Hollenbach R., *Laser interferometer for measuring high velocities of any reflecting surface*. Journal of Applied Physics, 1972. **43**(11): p. 4669-&.

112. Celliers, P.M., et al., *Line-imaging velocimeter for shock diagnostics at the OMEGA laser facility*. Review of Scientific Instruments, 2004. **75**(11): p. 4916-4929.

113. Roddier, C. and F. Roddier, *Interferogram analysis using Fourier-transform techniques*. Applied Optics, 1987. **26**(9): p. 1668-1673.

114. Takeda, M., H. Ina, and S. Kobayashi, *Fourier-transform method of fringe-pattern analysis for computer-based topography and interferometry*. Journal of the Optical Society of America, 1982. **72**(1): p. 156-160.

115. Celliers, P.M., et al., *Systematic uncertainties in shock-wave impedance-match analysis and the high-pressure equation of state of Al*. Journal of Applied Physics, 2005. **98**(11): p. 20.

116. Miles, R., et al., *Microfabricated deep-etched structures for ICF and equation-of-state targets*. Fusion Science and Technology, 2009. **55**(3): p. 308-312.

117. Rothman, S.D., et al., *Impedance match equation of state experiments using indirectly laser-driven multimegabar shocks*. Physics of Plasmas, 2002. **9**(5): p. 1721-1733.

118. Ding, Y., et al., *Structural phase transition of vanadium at 69 GPa*. Physical Review Letters, 2007. **98**(8): p. -.

119. Grad, G.B., et al., *Electronic structure and chemical bonding effects upon the bcc to Omega phase transition: Ab initio study of Y, Zr, Nb, and Mo*. Physical Review B, 2000. **62**(19): p. 12743-12753.

120. Perez-Prado, M.T. and A.P. Zhilyaev, *First Experimental Observation of Shear Induced hcp to bcc Transformation in Pure Zr*. Physical Review Letters, 2009. **102**(17): p. 4.

121. McMahan, A.K. and J.A. Moriarty, *Structural phase-stability in 3rd-period simple metals*. Physical Review B, 1983. **27**(6): p. 3235-3251.

122. Moriarty, J.A. and A.K. McMahan, *High-pressure structural phase-transitions in Na, Mg, and Al*. Physical Review Letters, 1982. **48**(12): p. 809-812.

123. DalCorso, A., et al., *Generalized-gradient approximations to density-functional theory: A comparative study for atoms and solids*. Physical Review B, 1996. **53**(3): p. 1180-1185.

124. Hohenberg, P. and W. Kohn, Physical Review B, 1965. **136**.

125. Kohn, W. and L.J. Sham, Physical Review B, 1965. **140**.

126. Moriarty, J.A., *Density-functional formulation of generalized pseudopotential theory*. Physical Review B, 1977. **16**(6): p. 2537-2555.

127. Koo, R.C., *A quantitative method for study of orientation relationship between subgrains by dark-field transmission electron microscopy*. Journal of Applied Physics, 1966. **37**(7): p. 2764-&.

128. Swift, D.C., et al., *Shock formation and the ideal shape of ramp compression waves*. Physical Review E, 2008. **78**(6).

129. Marsh, S.P., *LASL Shock Hugoniot Data*. 1980, Berkeley: University of California Press.

130. Hawreliak, J., et al., *Analysis of the x-ray diffraction signal for the alpha-epsilon transition in shock-compressed iron: Simulation and experiment*. Physical Review B, 2006. **74**(18): p. 16.

131. Olijnyk, H. and W.B. Holzapfel, *High-Pressure Structural Phase-Transition in Mg*. Physical Review B, 1985. **31**(7): p. 4682-4683.

132. Errandonea, D., et al., *Study of the phase transformations and equation of state of magnesium by synchrotron x-ray diffraction*. Journal of Physics-Condensed Matter, 2003. **15**(8): p. 1277-1289.

133. Milathianaki, D., et al., *A Seeman-Bohlin geometry for high-resolution nanosecond x-ray diffraction measurements from shocked polycrystalline and amorphous materials*. Review of Scientific Instruments, 2009. **80**(9): p. 7.

134. Mehta, S., G.D. Price, and D. Alfe, *Ab initio thermodynamics and phase diagram of solid magnesium: A comparison of the LDA and GGA*. Journal of Chemical Physics, 2006. **125**(19): p. 7.

135. Mattsson, A.E., et al., *Designing meaningful density functional theory calculations in materials science - a primer*. Modelling and Simulation in Materials Science and Engineering, 2005. **13**(1): p. R1-R31.

136. Ziesche, P., S. Kurth, and J.P. Perdew, *Density functionals from LDA to GGA*. Computational Materials Science, 1998. **11**(2): p. 122-127.

137. Moriarty, J.A., *Density-functional formulation of the generalized pseudopotential theory .2*. Physical Review B, 1982. **26**(4): p. 1754-1780.

138. Moriarty, J.A., *Density-functional formulation of the generalized pseudopotential theory .3. transition-metal interatomic potentials*. Physical Review B, 1988. **38**(5): p. 3199-3231.

139. Chavarria, G.R., *Calculation of structural pressure-induced phase transitions for magnesium using a local, first principles pseudopotential*. Physics Letters A, 2005. **336**(2-3): p. 210-215.

140. Jona, F. and P.M. Marcus, *Magnesium under pressure: structure and phase transition*. Journal of Physics-Condensed Matter, 2003. **15**(45): p. 7727-7734.

141. Asay, J.R., *Shock loading and unloading in bismuth*. Journal of Applied Physics, 1977. **48**(7): p. 2832-2844.

142. Colvin, J.D., et al., *Microstructure morphology of shock-induced melt and rapid resolidification in bismuth*. Journal of Applied Physics, 2007. **101**(8): p. -.

143. Duff, R.E. and F.S. Minshall, *Investigation of a shock-induced transition in bismuth*. Physical Review, 1957. **108**(5): p. 1207-1212.

144. Elias, P., P. Chapron, and C. Remiot, *Experimental-study of phase-transitions in shock-loaded bismuth*. Journal De Physique, 1988. **49**(C-3): p. 667-672.

145. Hughes, D.S., L.E. Gourley, and M.F. Gourley, *Shock-wave compression of iron and bismuth*. Journal of Applied Physics, 1961. **32**(4): p. 624-&.

146. Larson, D.B., *A Shock-induced phase transformation in bismuth*. Journal of Applied Physics, 1967. **38**(4): p. 1541-&.

147. Smith, R.F., et al., *Ultrafast dynamic compression technique to study the kinetics of phase transformations in bismuth*. Physical Review Letters, 2008. **101**(6): p. 4.

148. Larsen, J.T. and S.M. Lane, *HYADES - a plasma hydrodynamics code for dense-plasma studies*. Journal of Quantitative Spectroscopy & Radiative Transfer, 1994. **51**(1-2): p. 179-186.

149. Swift, D.C. and R.G. Kraus, *Properties of plastic ablators in laser-driven material dynamics experiments*. Physical Review E, 2008. **77**(6): p. 12.

150. Swift, D.C., et al., *Shock formation and the ideal shape of ramp compression waves*. Physical Review E, 2008. **78**(6): p. 9.

151. Chapman, H.N., et al., *Femtosecond diffractive imaging with a soft-X-ray free-electron laser*. Nature Physics, 2006. **2**(12): p. 839-843.

152. Marchesini, S., et al., *Coherent X-ray diffractive imaging: applications and limitations*. Optics Express, 2003. **11**(19): p. 2344-2353.

153. Barty, A., et al., *Ultrafast single-shot diffraction imaging of nanoscale dynamics*. Nature Photonics, 2008. **2**(7): p. 415-419.

154. Barty, A., et al., *Three-dimensional coherent x-ray diffraction imaging of a ceramic nanofoam: Determination of structural deformation mechanisms*. Physical Review Letters, 2008. **101**(5): p. 4.

155. Chapman, H.N., et al., *Femtosecond time-delay X-ray holography*. Nature, 2007. **448**(7154): p. 676-679.

VITA

Despina Milathianaki was born on February 18, 1978, in Agios Nikolaos, Crete, Greece, the daughter of Philippos and Irini Milathianaki. After receiving the International Baccalaureate Diploma in 1995 on a scholarship from the United World College of the Adriatic in Duino, Italy, Despina attended Imperial College London where she earned her Masters in Science in Physics, with First Class Honors, in the Spring of 1999. Despina continued her education at the University of Michigan in Ann Arbor receiving her Masters of Science in Electrical Engineering in 2001. After a brief period of employment outside academia, she enrolled at the University of Texas at Austin in the Fall of 2004, where she completed her PhD degree in the field of High Energy Density Physics under the supervision of Professor Todd Ditmire. During the last three years of her graduate work at the University of Texas at Austin, Despina was employed by the Materials Science and Technology Division at Lawrence Livermore National Laboratory, where she conducted the majority of her PhD research.

Permanent address: 5 Evans Street, Agios Nikolaos, 72100, Crete, Greece

This manuscript was typed by the author.